C. R. Chimie 21 (2018) 1230–1269

Contents lists available at ScienceDirect

Comptes Rendus Chimie

www.sciencedirect.com

Account/Revue

Spin-crossover nanoparticles and nanocomposite materials

Nanoparticules et matériaux nanocomposites à transition de spin

Lionel Salmon [a, *], Laure Catala [b, **]

[a] *Laboratoire de chimie de coordination (LCC), Université de Toulouse, CNRS, Toulouse, France*
[b] *Institut de chimie moléculaire et des matériaux d'Orsay (ICMMO), Université Paris-Sud, Orsay, France*

ARTICLE INFO

Article history:
Received 7 March 2018
Accepted 31 July 2018
Available online 30 October 2018

Keywords:
Spin crossover
Nanoparticle
Nanohybrid
Nanocomposite

ABSTRACT

This contribution reports on the state of the art of the elaboration and the application of nanoparticles (NPs) and nanohybrid/nanocomposite materials based on spin-crossover (SCO) complexes. The first part of this review concerns the syntheses and the characterizations of the physical properties of SCO NPs. All of the methods including homogeneous and heterogeneous media syntheses developed for the elaboration of such NPs and the associated methods used for their morphological characterization are presented. A particular attention is paid on the effects of the size reduction and the influence of the environment on the SCO properties and to specific and recent remarkable advanced physical measurements realized on a batch of NPs or on an isolated object. The second part presents the elaboration of various nanocomposite or nanohybrid materials for which SCO NPs have been associated with magnetic entities, noble metals, different fluorescent dyes, and different active polymers with the objectives to go toward specific applications based on synergistic effects between the two components.

Mots clés:
Transition de spin
Nanoparticules
Nanohybride
Nanocomposite

RÉSUMÉ

Cette contribution rend compte de l'état de l'art sur l'élaboration et la mise en application de nanoparticules et de matériaux nanohybrides/nanocomposites à base de complexes à transition de spin. La première partie de cette revue concerne la synthèse et la caractérisation des propriétés physiques de nanoparticules à transition de spin. Toutes les méthodes, y compris les synthèses en milieux homogène et hétérogène développées pour l'élaboration de telles nanoparticules et les méthodes utilisées pour leurs caractérisations morphologiques, sont présentées. Une attention particulière est portée aux effets de la réduction de taille et de l'influence de l'environnement sur les propriétés de transition de spin et sur des mesures physiques récentes remarquables réalisées sur un lot de nanoparticules ou sur un objet unique. La deuxième partie présente l'élaboration de divers

* Corresponding author.
** Corresponding author.
E-mail address: lionel.salmon@lcc-toulouse.fr (L. Salmon).

https://doi.org/10.1016/j.crci.2018.07.009

matériaux nanocomposites ou nanohybrides au sein desquels des nanoparticules à transition de spin ont été associées à des entités magnétiques, des métaux nobles, divers fluorophores et différents polymères actifs dans le but d'aller vers des applications spécifiques basées sur des effets synergétiques entre les deux composants.

1. Introduction

Spin-crossover (SCO) materials constitute nowadays a very promising research domain to go toward application in various fields incorporating molecular memories [1], pressure and temperature sensors [2,3], gas sensors [4,5], optoelectronic and actuators devices [6], nano-thermometers [7], and other "general public" applications like displays and intelligent papers or paints [8,9]. Indeed, the specific behavior of these complexes reposes on their intrinsic and stable switch related to intramolecular electronic transitions. The SCO phenomenon is now well understood and it is accompanied by the modification of optical, magnetic, and volumetric properties of the materials. Different cornerstone discoveries have legitimated the growing interest for such family of materials, in particular, (1) the role of the intermolecular interaction within materials, which we call cooperativity, on the nature and the abruptness of the spin transition behavior [10]; (2) the possibility to have SCO with hysteresis loop in the case of exacerbated cooperativity affording the possibility to have a memory effect [1]; (3) the versatility of the stimuli that can be used to trigger the spin state, that is, temperature, light, magnetic, and electric field or the inclusion of a guest molecule [11–13]; (4) the possibility to have room temperature SCO transition (a paramount result was the discovery of a light-induced reversible switch in the hysteresis loop at room temperature) [14]; and more recently, (5) the maintaining of the bistable behavior in nanometric-sized particles or thin films [15–18]. In general, the macroscopic behavior of bulk SCO materials is strongly influenced by electron–lattice coupling effects. In particular, the modification of the volume and shape of the molecules accompanying the spin state change leads to considerable elastic interactions between them. These interactions give rise to various cooperative phenomena, such as first-order phase transitions or self-accelerating relaxations of metastable states. Research into SCO nanoparticles (NPs) is chiefly motivated by the long-standing question of the size effect on the first-order phase transition observed in many cooperative SCO systems. Particular attention is focused on the hysteresis property, which is expected to be strongly affected when decreasing the number of molecules constituting the particle. An important challenge in this context is to preserve the bistability and the cooperative spin transition properties during the downsizing of the compound at the nanoscale. So, in a first approximation, size reduction effects in SCO materials are expected to occur primarily due to the reduction in the number of interacting metallic centers and the associated decrease in the cooperativity. We shall see later that this picture is too simplistic and many other parameters and material properties have to be considered to interpret the experimental observations obtained with SCO nanomaterials. Because the investigation of the size effects on the bistability remains one of the main objectives in the field, there is a clear need for novel characterization tools and techniques with high spatial resolution as well as high sensitivity able to detect molecular spin state changes in very small amounts of matter, ideally in a single isolated nano-object. By the same token, these studies open up also new perspectives for the development of applications [19].

The first part of this review concerns the syntheses and characterizations of the physical properties of SCO NPs. Section 2 starts with the description of various techniques including homogeneous and heterogeneous media syntheses developed for the elaboration of such NPs and the associated methods used for their morphological characterization. Then, an exhaustive state of the art concerning the size, shape, and the SCO properties of molecular and polymeric complex particles is reported. A particular attention is paid on the effects of the size reduction on the SCO properties and to specific and recent remarkable advanced physical measurements realized on a batch of NPs or on an isolated object. Section 2.3 is dedicated to the influence of the matrix and the surface on the SCO behavior.

The second part of this review presents the state of the art of various nanocomposite or nanohybrid materials based on SCO compounds. Indeed, SCO materials have been associated with magnetic entities, noble metals, different fluorescent dyes, and different active polymers with several objectives in mind. First, to be able to probe the SCO properties of a reduced quantity of matter and ideally a single particle, and on the other hand, to try to go toward specific applications based on synergistic effects between the two components.

2. SCO nanoparticles

2.1. Methods for the elaboration and characterization of SCO NPs

This section intends to review the main bottom-up synthetic processes and characterization techniques that have been used on various SCO nanomaterials. These synthetic methods have been extensively applied to oxide/sulfide/metallic NPs. The aim of this introductive part is to stress the specificities, advantages, and drawbacks of the different methods for downscaling SCO compounds. More experimental details on each compound will be provided in Section 2.2. Three main synthetic routes may be distinguished: hard template, soft template, and template-free synthesis. Concerning the characterization techniques of such nanomaterials, rather than fully describing each technique we will stress the importance of the

complementary information that may be extracted and a few basic points for any newcomer in the field. These basic characterizations are compulsory to establish reliable studies on SCO nanomaterials and avoid inconsistent comparisons.

2.1.1. Hard template synthesis

Synthesis of coordination NPs in hard templates such as silica, anodized alumina, polysaccharide beads, and a few other templates have been reported along the last decade for several coordination polymers (CPs) starting with the most studied Prussian blue analogues (PBA). The main advantage over other synthetic strategies relies on the fact that the nano-objects may be directly shaped by the template porosity with a controlled and predictable size and shape tuned by that of the pores (Fig. 1, top). One main difficulty of the hard template approach is to confine growth within the mesoporosity only and avoid any precipitation on the external surface, and the use of functionalized internal pores (by ligands or preincorporated metal centers) is the most recommended strategy. The precipitation of SCO inside the pores can also be done by adjusting the water volume around 80% of the porous monolith volume and immersing it in an apolar immiscible solvent such as hexane [20]. Oxide-based hard templates are convenient to control growth of PBA coordination networks as recently reviewed [21]. Among PBAs, the $A_xCo[Fe(CN)_6]_y$ family ($A = Cs^+$, Rb^+, Na^+, etc.) is highly interesting as it exhibits thermo- and photoswitchable behavior that involves a charge transfer–induced spin transition (CTIST) depending on the nature and amount of the inserted alkali cation A^+ [22–24]. Although no study was reported on PBA NPs that usually display thermal CTIST (with $A = Rb^+$, Na^+) most likely because of the disappearance of the transition with size reduction and/or the matrix effect, photoswitchable $Rb_xCo[Fe(CN)_6]_y$ PBA NPs embedded in templates have been reported by several methods. To a lesser extent, SCO NPs were also produced in hard templates. A few examples are provided to illustrate each method.

A first strategy, even if it may not be fully considered as "hard template" in some cases, is based on sol–gel synthesis to confine the nucleation and growth processes in a silica xerogel obtained by hydrolysis of alkoxysilanes (as TEOS or TMOS) in basic or acidic conditions. The first example reported 8–10 nm KCoFe NPs entrapped in a xerogel that did exhibit photomagnetic behavior but where the formation of the gel and PBA were not decoupled [25]. Another process was developed by Fornasieri et al. [26], which consists in the addition of a cobalt(II) basic solution to the silica sol that leads to the formation of unreactive tetrahedral species, and subsequent addition of a ferricyanide solution that enables the insertion of both precursors without formation of the PBA. A simple acidification step restores the octahedral Co^{II} species that immediately react to form the $Rb_xCo[Fe(CN)_6]_y$ particle. Concerning SCO compounds, NPs around 2.5–5 nm were obtained for the one-dimensional (1D) $[Fe(Htrz)_2(trz)](BF_4)$ CP within a silica xerogel by adding an aqueous solution of the preformed complex into a methanolic solution of alkoxysilane at pH = 5 followed by aging and drying in mild conditions in different containers to control their shaping as film, disk, or monolith (test tube or Petri dish) [27]. Fairly good crystallinity was achieved but partial oxidation of Fe^{II} to Fe^{III}

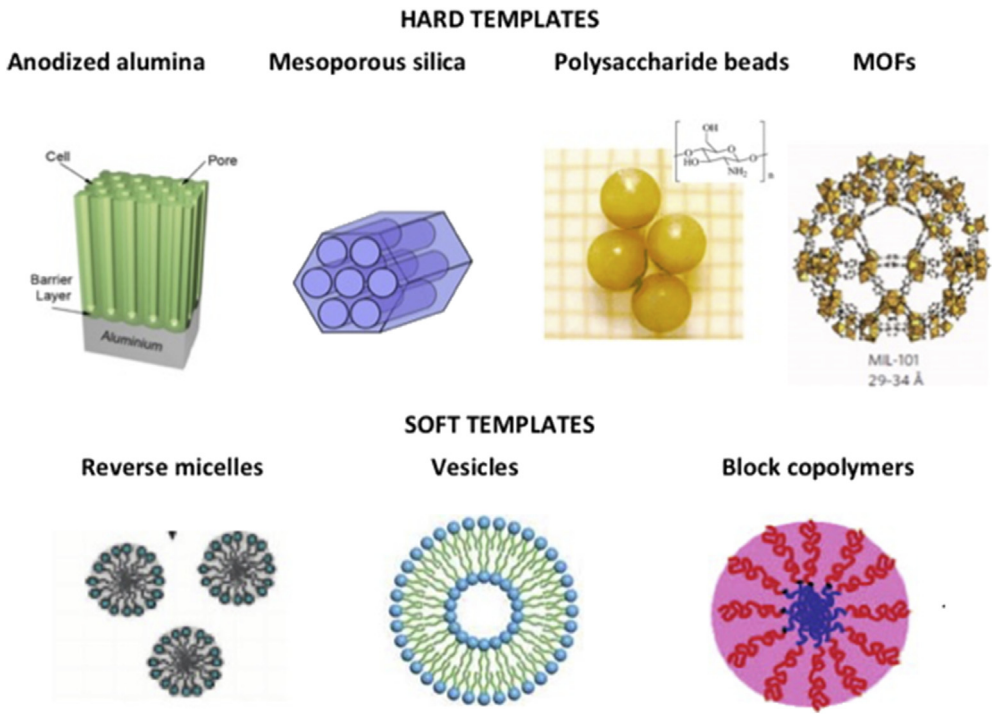

Fig. 1. Schematic representation of some templates (hard and soft) that may be applied to the controlled growth of SCO NPs.

was evidenced by Mössbauer spectroscopy. When producing silica nanocomposite films, a crucial parameter is the increase in the aging time that tunes the viscosity of the gel before the spin coating of the film. Size is critically affected by this parameter, as illustrated for the mononuclear complex $[Fe((mepy)_3tren)](PF_6)_2$ where the average size was tuned between 47 and 730 nm when aging between 2 weeks and 1 h, respectively [28].

Besides, silica *mesoporous* matrices have calibrated and organized porosity with the widest range of structuration and shaping possibilities (powder, film or monolith) because of the well-developed surfactant-assisted sol–gel processes. The optical and mechanical performances as well as good thermal stability are highly appealing, especially when photoswitchable particles are targeted. This has allowed us to control various PBA NPs, among which NPs of 5 nm of $Rb_{0.5}Co[Fe(CN)_6]_{0.82}$ (containing Co^{III}–Fe^{II} photoswitchable pairs) were successfully synthesized within silica monoliths by a two-step method: a first step based on Co^{II} octahedral complexes solubilized in the copolymer and subsequent calcination that induces grafting of tetrahedral Co^{II} species with a low degree of condensation onto the silica pore walls, and a second step by impregnation with an acidic solution of ferricyanide that restores the octahedral Co^{II} species followed by immediate precipitation of PBA NPs [29].

A preformed silica monolith was also used to confine SCO polymers such as $[Fe(Htrz)_2(trz)](BF_4)$ [30]. This two-step approach led to 3 nm $[Fe(Htrz)_2(trz)](BF_4)$ spherical particles. Furthermore, the use of hexagonal MCM-1 (Mobil Crystalline Materials) with pores from 2 to 2.7 nm in diameter was reported to grow the 1D CPs $[Fe(Htrz)_2(trz)](BF_4)$ and $[Fe(Htrz)_3](BF_4)_2$ in the cylindrical pores, leading to crystalline spherical NPs around 2 nm in both cases without any oxidation. In both cases, the compound that deposited on the external surface of the powders was washed out easily. Other nanoporous templates such as metal–organic frameworks may also be envisaged to produce particles less than 2 nm in size. One example of $[Fe(HB(pz)_3)_2]$ SCO complex in several types of MIL-101 was obtained directly during synthesis of the metal–organic framework itself and may be extended to produce other types of ultrasmall particles [31]. In the case of 3D Hofmann clathrates, confinement in silica templates was not reported apart from one attempt with a Co^{II} compound (that does not exhibit SCO [32]), even if the grafting of a ligand on the internal walls of the pores using pyridine or click chemistry may be applied to coordinate the Fe^{II} species. This may be related to the difficulty to avoid defects in pyrazine during the washing steps. Still hard templates of polysaccharides (chitosan and alginate beads) were successfully used on the $\{Fe(pyrazine)[M(CN)_4]\}$ (M = Pt, Pd, Ni) 3D compounds and PBAs. Anchoring in the polysaccharide beads is achieved, thanks to the coordination of NH_3 or COOH groups to Fe^{II} in chitosan and alginate, respectively. Successive impregnation was performed with the three precursors (iron salt, pyrazine, and tetracyanometallate salt) and was optimized to ensure precipitation occurred within the porosity only. This was done by extensive washing with methanol after each step. This synthetic method cannot be simply transposed from one compound to another, as the ratio between the two metals M/Fe strongly depends on the M–CN–Fe bond strength, and incomplete coordination occurred when M = Pt, Pd, whereas M = Ni leads to the expected Ni/Fe = 1. This has tremendous consequences on the SCO behavior (see subsequently). The number of defects after the rinsing steps may be also complicated by the fact that while the 2D cyanide-bridged sheets are easily formed by reacting Fe^{II} salts with tetracyanometallates, the complete interconnection of these planes by pyrazine to form the defectless 3D structure requires the use of solvent mixtures, low temperature, or high concentrations in precursors. Such polysaccharide templates have the advantage to induce confinement below 4 nm and the particles may be post-dispersible in solvents, whereas oxide-based templates require the use of harsh conditions (strong base or HF) to extract the NPs that may damage the material crystallinity and composition. With all of these hard template methods, spherical NPs were identified, despite the cylindrical shape of most pores in silica that may favor rod-shaped particles by coalescence of particles in the channels. Larger cylindrical pores of porous alumina membranes are more favorable to tune the shape of SCO particles. These membranes are obtained by oxidation of aluminum and periodic dissolution of alumina under applying an electric field leading to hexagonal packing of pores perpendicular to the surface with an average diameter typically greater than 50–300 nm (and many micrometers in length). Anodized alumina was used, for instance, to prepare several types of PBA nanowires or nanotubes (by electrodeposition) [33,34] and nanowires of the molecular SCO complex $[Fe(sal_2\text{-}trien)]$ (80–100 nm width, micrometer length) [35]. Cationic exchange resin beads were also used where successive impregnation with the precursors to produce alignment of nanorods of Fe triazole polymers at the periphery of the beads (see subsequently); in this case, the template promotes a release of Fe and a controlled nucleation at the surface and the shape of the particles is related to the 1D structure of the compound itself [36].

Most of these hard template methods are in general not straightforward, lead to low yields of highly diluted paramagnetic nanocomposites difficult to measure. Also of utmost importance, the rigid matrix plays a noninnocent and complex role on the cooperativity, transition temperature, and completeness of the SCO phenomenon, as detailed in Section 2.3. It should be reminded that this strategy always couples size effects to matrix/interfacial effects that may either be beneficial or detrimental to the SCO cooperative character.

2.1.2. Soft template/polymer-assisted synthesis

Multiple routes are available to control nucleation and growth by using self-assembled nanostructures based on surfactants or polymers where nanometric pools may confine the growth (Fig. 1, bottom). A water-in-oil microemulsion is an optically transparent and thermodynamically stable dispersion of water in an apolar solvent stabilized by an interfacial film of a surfactant, sometimes in combination with a cosurfactant. It has been efficiently used to downscale many inorganic materials as pioneered by Pileni [37]. Reverse water-in-oil micelles are nanometric water pools stabilized in the apolar phase by surfactants

(organic compounds having a hydrophilic "head" and a hydrophobic "tail") with low packing parameters $g = V/Al$ around 1/3, where V is the molar volume of the surfactant, A is the area per head group, and l is the contour length of the alkyl chain. Charged surfactants may be used as the most employed anionic bis(2-ethylhexyl) sulfosuccinate (AOT) or cationic cetyltrimethylammonium, but also neutral as Brij, Igepal, Laurepal, Tergitol that all include water-soluble oxyethylene oligomers.

This method was first applied to PBA coordination networks [38] and is perfectly adapted to SCO compounds that are insoluble in water and obtained from water-soluble precursors. The two water-soluble precursors are separately dissolved in the desired volume of water and the surfactant dissolved in the apolar solvent (alkane) is added under vigorous stirring (that may be accelerated by sonication) to obtain the two separate translucent microemulsions. Brownian motion promotes the fusion of micelles that exchange their content leading to the formation of the water-insoluble compound. This process was successfully applied to SCO polymers such as iron triazole–based 1D polymers and {Fe(pyrazine)[$M(CN)_4$]} 3D Hofmann clathrates (M = Pt, Pd, Ni) (Fig. 2). Furthermore, it has been applied to the mononuclear complex [$Fe(phen)_2(NCS)_2$] by Valverde-Muñoz et al. [39] to produce rhombohedral particles around 150–200 nm large. The iron and thiocyanate precursors were contained in one microemulsion and a methanolic solution of phenanthroline was used to stabilize the second microemulsion. A detailed description for each sample will be given in section 2.2, but some general features may be underlined. The first point is obviously to work with a water/oil/surfactant ratio where reverse micelles are stable in the corresponding ternary diagram that depends on the oil/surfactant mixture, and this is favored for surfactants that have large hydrophobic tails ($g = 1/3$). Concentration in precursors within the water pools is one parameter that affects the size as a nucleation-controlled process is often favored. Smaller particles are generally produced when higher concentrations of precursors are used. An important point is to maintain the stability of the microemulsion over time and avoid any uncontrolled flocculation process, so that concentration may not be increased above a certain threshold that is compounddependent. Particle size strongly depends on the solubility of the compound and interaction with the surfactant, so that physicochemical parameters can hardly be extrapolated from one compound to another. Furthermore, the water/surfactant ratio ω may be varied between 5 and 50 (depending on the ternary system) and it tunes the water nanopool size. The size of the reverse micelles linearly depends on ω but is restricted to a small size range depending on the system (much less than 50 nm). For instance in the case of AOT/water/isooctane ternary system (with [AOT] = 0.1 M), a change in ω from 5 to 35 tunes the water pool diameter from 3 to 14 nm. However, apart from low water content ($\omega = 5$) where the micelle size controls the particle size through interfacial energy of the boundary surfactant, size and shape may be very different from the initial water pool size and unpredictable, due to controlled aggregation and reorganization of the surfactant at the particle surface. Nanorods of [$Fe(Htrz)_2(trz)](BF_4$), around $100 \times 10 \times 10$ nm^3 [40], may be produced in AOT-stabilized water-in-oil reverse micelles beyond the size of the initial water pools meaning that the growth of the crystal facets is dominant and the surfactant reorganizes at the nanocrystal surface. However, this is a

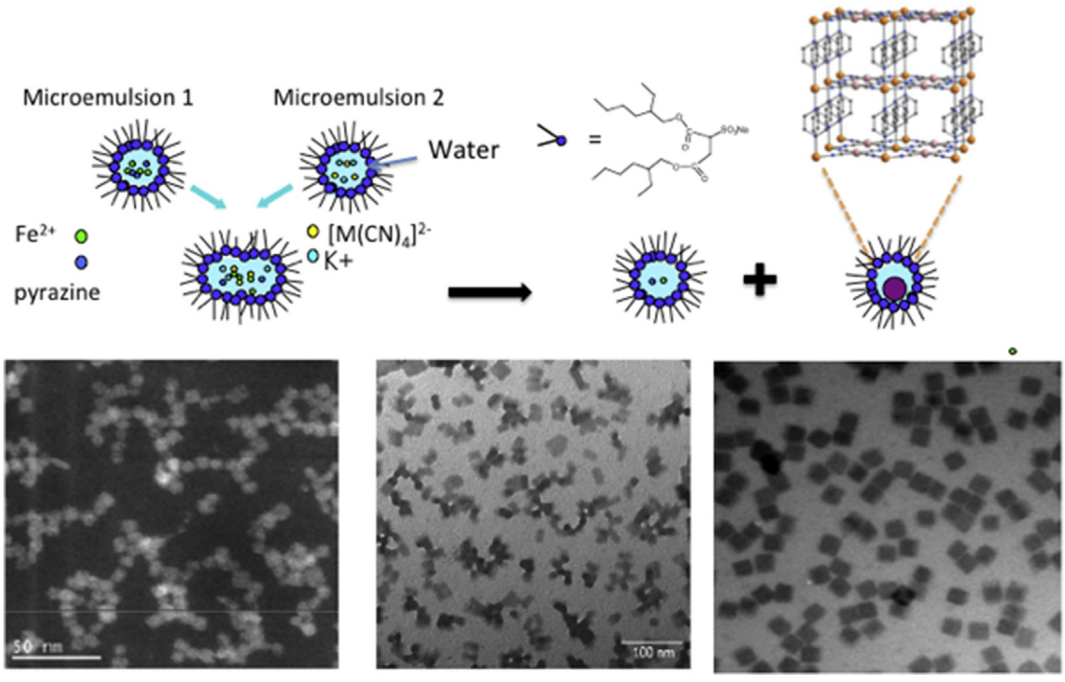

Fig. 2. Example of water-in-oil microemulsion method to tune size of Fe(pyrazine)[$Pt(CN)_4$] depending on physicochemical parameters (decrease of the precursors concentrations from left to right).

typical case where the growth of the nanocrystals is not totally controlled by the micelles and the flocculation of the microemulsion occurs after 30 min. A major point is to preserve *individualized* particles after flocculation of the microemulsion, maintaining their processability and avoiding irreversible coalescence. Importantly, the excess of surfactant strongly modifies the SCO behavior (either increasing or suppressing the cooperativity depending on the compound, see Section 2.3). In many reports, flocculation is done by adding a solvent (acetone, ethanol, etc.) and several washing steps of AOT with acetone are performed, but it is hard to insure that no coalescence has occurred (that may change the properties) and only dynamic light scattering/transmission electron microscopy (DLS/TEM) on dispersed sample after the washing process provides a clear proof, which is scarcely mentioned in the literature. With iron triazole–based CPs, the compound contains cationic chains and anions located in between. Anionic surfactants have, therefore, a strong affinity with the particles because of the electrostatic interaction with the cationic CPs, so that the extensive washings of AOT are possible keeping a monolayer of AOT only at the surface. This is not the case of neutral Hofmann clathrates. In most cases, a small amount of AOT remains in the sample (even if it may be totally suppressed), but this quantity has to be severely controlled to compare SCO properties in a reliable way between different samples. When extensively washed, partial coalescence of particles during the washing process may occur and is hard to characterize even with X-ray diffraction (XRD). A way to avoid any problem is to protect the particle during the flocculation step by a molecule/coating that strongly binds to the surface more than the surfactant itself. A convenient recovery consisted in using pyridine-based ligands that coordinate at the Fe^{II} sites located on the surface [41]. To avoid decoordination of monodentate ligands during the multiple washing steps while maintaining subsequent dispersibility in organic solvents, one successful strategy relies on using a strongly chelating ligand with eight pyridine groups (linked covalently to a calix-[8]arene ring) without affecting the composition and shape. The most convincing way to show that the integrity of the particle has been maintained is to disperse the particles after the washing steps and characterize them by DLS, TEM, and energy-dispersive X-ray (EDX) spectroscopy [41].

Apart from surfactant, block copolymers (BCPs) form micellar structures because of the strong difference in solubility between one block and the other in a chosen solvent [42]. If this solvent is water as for copolymers having a hydrophilic block (such as poly(ethylene glycol), polysulfonate, polyvinylpyridine, polypyrrolidone, etc.) the core will be formed by the hydrophobic part and will serve to encapsulate apolar compounds, whereas the use of a less polar solvent may lead to a more polar core. The advantages of this method are as follows: (1) it may be applied in solvents others than water (thus applicable to neutral reactants and products); (2) the size of the particles may be larger than those obtained with other strategies; (3) the use of coordinating functions in the core may lead to controlled location of the reactants in the cores; and (4) the obtained colloids may be easily processed by slow evaporation of the solvent to lead to ordered structures and films. Only one example has been reported to date using polystyrene-poly-4-vinylpyridine in THF to form 50 nm particles of a 1D CP $[Fe(L)(bipy)]_n$ (with L = 1,2-phenylenebis(iminomethylidyne)bis(2,4-pentanedionato) (2-) and bipy = 4,4′-bipyridine) starting from the neutral $[Fe(L)(MeOH)_2]$ complex and bipyridine. Repeated addition of the precursors at high temperature led to NPs with an enhanced crystallinity that were isolated by cold distillation of the solvent [43] (see Fig. 3).

Besides the use of self-assembling BCPs, polymer-assisted coprecipitation is also commonly used. The polymer is chosen to interact with the particles through coordination bonds, hydrogen bonds, or electrostatic interactions that help to control nucleation and efficiently limit the aggregation of particles by inducing steric or electrosteric stabilization. This strategy is different from studies on nanocomposites where the compound is prepared and simply suspended in a matrix. The polymer/precursor ratio may control the size of the NPs, but often mainly avoids secondary aggregation and reorganization steps. Polyvinylpyrrolidone (PVP) has been efficiently used to stabilize photomagnetic NPs of octacyanometallate-based networks (spherical or nanorods) and CoFe PBA between 3 and 50 nm (spherical or cubic) but more scarcely used for SCO compounds to control the growth. Again one should keep in mind that the influence of the polymer embedding the particles may strongly affect the SCO behavior (see Section 2.3).

In sub-100 nm Hofmann clathrate NPs surrounded by PVP, suppression of the cooperativity was observed by Volatron [44] (later on attributed to a strong matrix effect). Platelets of a 2D Hofmann clathrate were reported by Martinez et al. [45] stabilized in PVP with similar effects. For iron triazole 1D CPs, several polymers (PVA, PEG, Triton, etc.) [46] have been used leading to rather large particles but it remains difficult to produce nanostructures less than 100 nm using this approach (see section 2.2), probably due to rather weak interactions with the particles.

2.1.3. Surfactant-free synthesis

Besides these template-based methods that are efficient routes to control particle size less than 10 nm, other homogeneous synthetic strategies may be applied that do not require any stabilizer/template. The main requirement is to produce an efficient nucleation step avoiding overlap of nucleation and growth events. This may be done as proposed by Lamer and Dinegar [47] on colloidal sulfur by inducing high supersaturation in a reactant either by producing the reactive moieties progressively from a precursor (as hydrolysis in sol–gel synthesis) or by changing the solubility by adding a miscible nonsolvent and/or changing the temperature. Monodisperse particles may be produced, starting from precursors that are soluble in a solvent (that may act as a ligand toward the transition metal such as water) and adding a miscible antisolvent to provoke the nucleation event with primary particles that may often subsequently lead to secondary particles by fusion [48].

For instance, valence tautomerism particles were prepared by connecting $\{Co^{III}(3,5\text{-dbsq})(3,5\text{-dbcat})\}$ units through the 1,4-bis(imidazol-1-ylmethyl)benzene (bix)

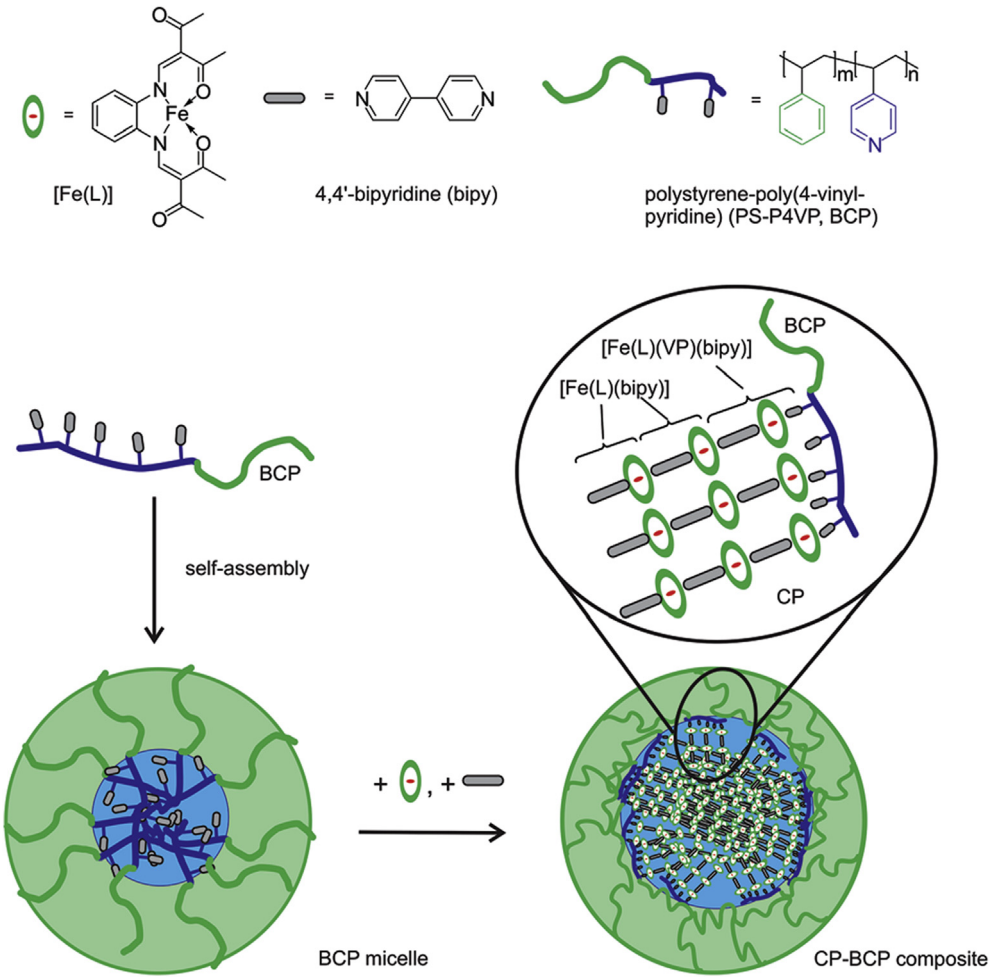

Fig. 3. Schematic representation of a self-assembled BCP micelle for use as a nanoreactor. Successive addition of the complex [Fe(L)] and the bridging ligand bipy to the BCP micelle will lead to a growth of the CP in the core of the micelle. Adapted from Ref. [43].

ligand, achieving a so-called "infinite CP". For this compound, spherical amorphous particles were obtained with a tunable size between 75 and 200 nm depending on the water addition rate that controls the supersaturation and thus the amount of produced nuclei. In many cases, the aggregation process and ripening precludes long-term stability and colloidal particles have to be isolated rapidly from the solution or stabilized with polymers [49]. Playing on the physicochemical parameters (solvent nature, temperature, and pH) is also a way to tune the size of microparticles to NPs of 1D iron triazole CPs without the help of any stabilizer, for instance, using solvent mixtures where the solvent may coordinate and stabilize short oligomers (as in chlorinated/alcohol mixtures or acetone, see subsequently) [46].

In the case of *charged* particles, Oswald ripening is strongly limited and particles remain stable for months, even if some reorganization may take place. Charging the surface provides an efficient way of reducing surface tension in water (as observed for oxides) and leads to stable nuclei of smaller sizes. This is the case of PBA and octacyanometallate-based coordination networks that have been reported to display thermal SCO ($CsFe[Cr(CN)_6]$) or CTIST ($ACo[Fe(CN)_6]_y$ with A = Na, Rb, $CsMn[Fe(CN)_6]_y$), light-induced electron transfer ($ACo^{III}[Fe^{II}(CN)_6]_y$ with A = Cs, Rb, etc.) and light-induced excited spin state trapping (LIESST) effects ($CsCu[Mo(CN)_8]$). For $Cs_xM[M'(CN)_6]_y$ it was shown that playing on the stoichiometry of the polycyanometallate and the cations (both transition metal and alkali) it is possible to stabilize sub-100 nm negatively charged nanocrystals by fast addition of an aqueous solution of cations into the polycyanometallate solution, with a size dependence that follows the Irving Williams series [21]. The surface charge is due to the presence of hexacyanometallates and the overall particle is charged as well due to incomplete insertion of alkali inside the tetrahedral vacancies. Moreover, the larger the complexation constant, the lower the solubility and the higher the nucleation rate for similar precursor concentrations. Nucleation is favored by the presence of Cs^+ cations that act as templates for the formation of the fcc structure. It was clearly shown that kinetics of nucleation and growth is accelerated in the

order $Cs^+ > Rb^+ > K^+$, Na^+ with a decreasing amount of vacancies. Hence Cs^+ and Rb^+–containing PBAs are the most interesting systems to obtain (1) small particles between 3 and 60 nm and (2) particles with a small amount of hexacyanometallate vacancies. An overall negative charge is obtained (negative ζ potential) and related to the presence of an excess of polycyanometallates that insure the long-term stability of the colloidal solution. Similar features were observed on alkali-containing octacyanometallate-based particles. NPs of $CsFe[Cr(CN)_6]$ and $A_xM[Fe(CN)_6]_y$ (M = Co, Mn; A = Rb, Na; and $x = 0.2–0.6$) were obtained by some of us but despite the good chemical sand structural features (crystallinity, low amount of vacancies, and no linkage isomerism) no cooperative SCO or CTIST was observed to date on PBA when size is reduced to less than 200 nm.

One main advantage of these cyanide-bridged particles is that starting from well-controlled seeds, it is possible to control growth of a defined thickness of the same coordination network or another network that has very similar cell parameters by sequential addition of the precursors in a one-pot process with a perfect predictability over the size, composition, and crystallinity [50]. Importantly, a matrix (polymer, ligand) may be added a posteriori if needed. Even if this strategy is probably the most interesting way for a very systematic study on different sizes of SCO compounds and decorrelate any matrix effect, it is however not applicable to Hofmann clathrates because of the neutrality of the network and neutral [001] facets of the nanocrystals that lead to fast aggregation. Moreover, the smaller complexation constant does not allow the synthesis in diluted conditions. Some combined approaches using PBA seeds for Hofmann clathrates self-stabilized nanocrystals are under progress but there is still no report about self-standing processable NPs less than 100 nm for this family of compounds. A few other template-free strategies have been used by tuning the nature of the solvent (with high dielectric constant) and thus the solubility of the compound, as for PBA (without SCO behavior) in ionic liquids and for iron triazole derivatives in different solvents (see subsequently).

Besides, the continuous production of SCO microparticles and NPs is of technological interest and an attempt has been reported using millifluidics [51]. The use of a milliscale segmented technique (setup with milliscale PTFE tubes and a mixing chamber) has the advantage to produce larger amounts of materials than microfluidic devices (see Fig. 4). One example has been reported recently and shows that using a kinetically regulated automated input crystallizer, a good agreement was obtained with the samples produced by coprecipitation, in the range of 700–1000 nm. Future work is underway in several groups to improve the homogeneity and reduce size using microfluidics. It is also worth mentioning that spray drying used to produce dry powders by rapidly drying with a hot gas has been applied to some iron triazole–based CPs and a mononuclear SCO complex [52]. For the former cases, shape of the microcrystals (spherical) was different from that of the batch synthesis (rods) whereas being similar for the SCO complex, and low crystallinity that affects the SCO properties (see Section 2.2).

2.1.4. Size and shape analysis

Size and size dispersion are determined using TEM, which provides a direct visualization of the inorganic cores containing high-Z elements that scatter the accelerated electronic beam (typically under a 100–200 kV voltage) with a resolution directly related to the voltage that results in a dark contrast corresponding to the inorganic cores (in bright field mode). The lower metal density of CPs often leads to a much lower contrast as compared with purely metallic NPs that complicates the observation of NPs less than 10 nm; low-dose imaging may be recommended to avoid alteration of the NPs (desolvation and amorphization). Preparation of a routine sample consists in depositing a few drops of the colloidal solution on a TEM copper grid covered with an amorphous carbon layer often reinforced by a polymer (Formvar) and dried before observation. Statistics on the size distribution should be determined (for all dimensions if anisotropic) to provide the average value of the inorganic core together with the standard deviation (e.g., with ImageJ, i.e., a free software). Organic coating does not induce detectable contrast in conventional bright field mode; organic surfactants/polymers may render the inorganic core harder to visualize so that it should be avoided/limited when possible.

The overall diameter of colloidal particles (inorganic core and coating) may be assessed by DLS directly on the colloidal solution. Indeed, by collecting the scattered intensity resulting from the particle interaction with the laser beam, DLS allows estimating the hydrodynamic diameter that includes the core, the coating, and the solvation shell. It is dependent on the ionic force so that a constant ionic force should be maintained (adding salt). Shape of the particles is assumed to be spherical, and in the case of rod-like particles, the diffusion is mainly governed by the length of the rod rather than its width. The technique consists in comparing the resulting diffraction pattern coming from the ensemble of particles in the volume probed by the laser ("speckle") with time. An autocorrelation function reflects whether the signal change is fast (going fast from 1 to 0). As the translational diffusion coefficient D of a spherical particle decreases with increasing hydrodynamic diameter as stated by the Stokes–Einstein law, smaller particles lead to an autocorrelation function that decreases from 1 to 0 much faster than for larger ones. Fitting of this autocorrelation function leads to the estimated hydrodynamic diameter $d(H)$. The Rayleigh scattering intensity is approximately related to $d(H)^6$; therefore, a large overestimation of the population of larger sizes is obtained from the scattered intensity (that may be reduced if using other representations in volume or number but introducing a large approximation if the refractive index of the coordination network is not well known). It remains the most useful technique to detect the presence of any trace of aggregate in solution. This technique is thus compulsory to check that particles are well individualized, and often the only way to prove that no coalescence has occurred (after recovering from the microemulsion for instance). Another way to check the particles are not aggregated in the solution and determine directly size distribution of the core is to use microtomy on a frozen drop of solution and study them by cryo-TEM. Still DLS is the only technique that

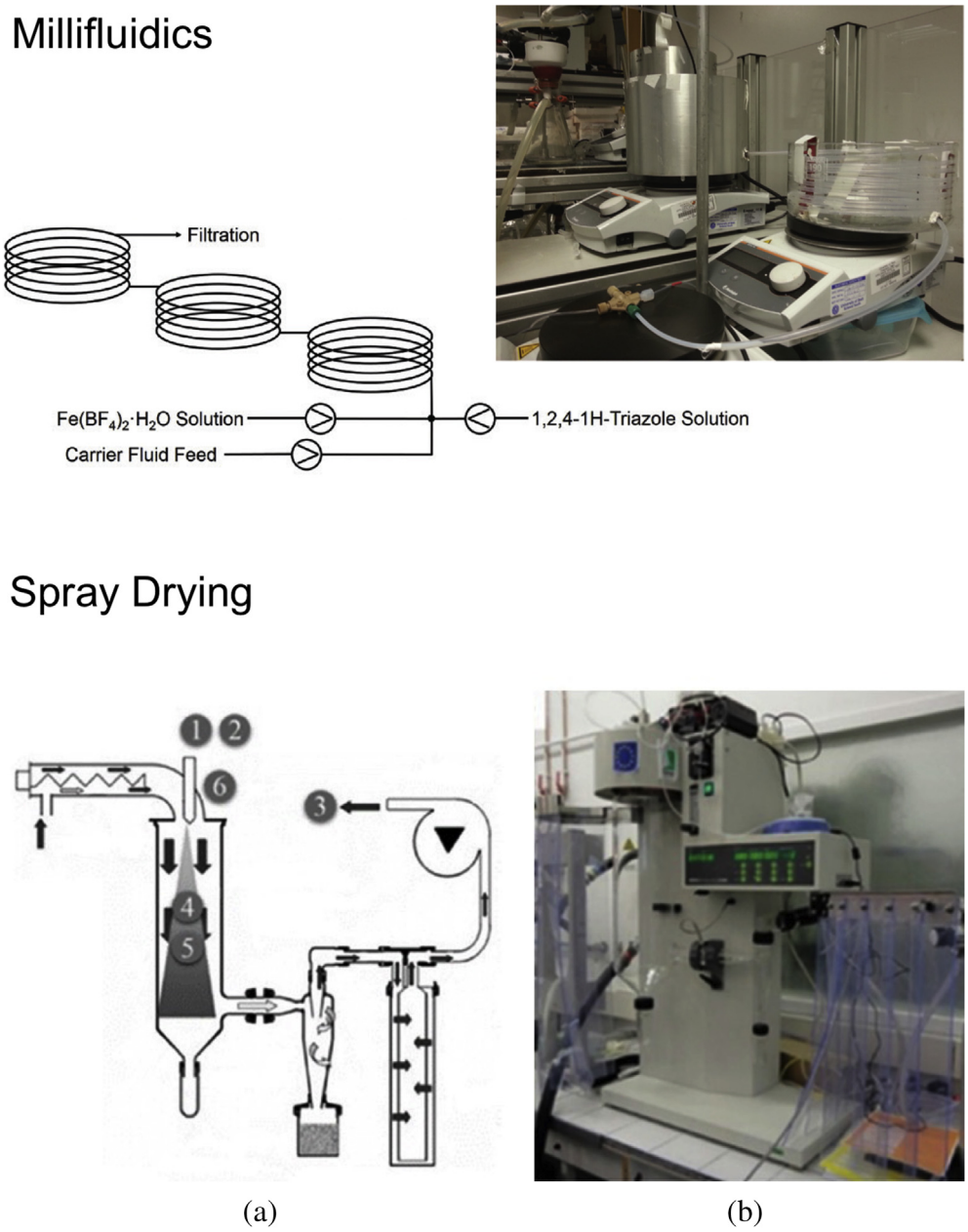

Fig. 4. Setups for the production of particles by millifluidics (top) and spray drying (bottom). Adapted from Refs. [51,52].

provides information on the extension of the organic layer/solvation shell.

2.1.5. Structure and crystallinity

Powder XRD is the routine technique to carry on powders of particles in order to check the structure of the NPs comparing the diffraction peaks with those of the bulk compound. In some cases, it was shown that the nanoscale compounds lead to new polymorphs, which may exhibit completely different SCO phenomena. Moreover, the correlation length that corresponds to the size of crystalline domains may be determined from the full width at half maximum that increases when decreasing size, as stated by Scherrer's law (applicable to sizes up to 100 nm due to the instrumental broadening). This gives a first indication whether the whole particle is crystalline or composed of aggregates of smaller NPs as sometimes seen on iron triazole particles. This often leads to an overestimation as compared with TEM evaluation, because of the higher intensity obtained with larger sizes, and has to be considered as a rough estimation for nanocrystals less than 10 nm where the peaks are large and weak in intensity. Crystallinity may be checked on the local scale by high-resolution electron microscopy where defects such as dislocations may be identified, especially in core–shell heterostructures (see Fig. 5).

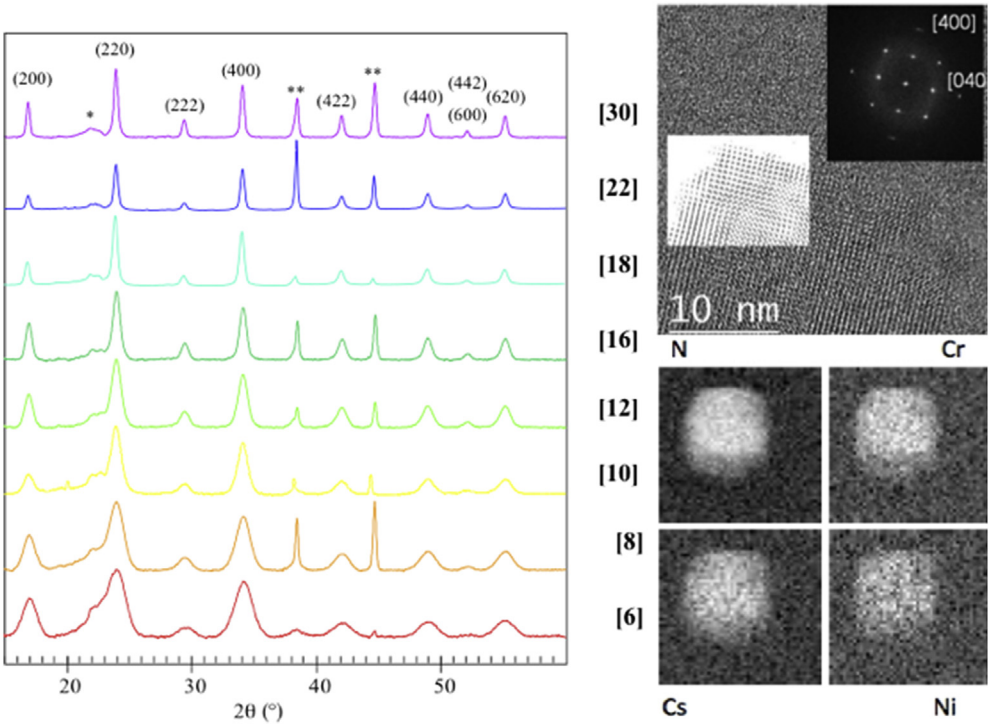

Fig. 5. Left: X-ray powder diffraction on powder sample of PBA of 6 to 30 nm; Top right local analysis of crystallinity of single particle by high resolution TEM; Bottom right: local composition (N, Cr, Cs, Ni) by energy electron loss spectroscopy by scanning TEM.

2.1.6. Chemical composition

The chemical composition determined preferentially by elemental analysis and/or EDX spectroscopy is crucial to check that the inorganic core remains the same when changing the size of the particles and that the content of organic matter is unchanged (surfactant or any matrix); if the content in surfactant/polymer is not strictly comparable in a series, this may strongly affect the properties and may be misinterpreted. Local composition at the nanometric scale may be carried out by more specific techniques such as EDX spectroscopy used in conjunction with the microscope or electron energy loss spectroscopy (EELS) coupled with scanning transmission electron microscopy (STEM) that provide a local mapping of the different elements and probe the homogeneity of the composition within the nanocrystal. These techniques are very useful to discriminate between core–shell and alloyed structures.

Other techniques commonly used to characterize SCO compounds such as Mössbauer spectroscopy, infrared and Raman spectroscopies, and magnetic susceptibility measurements confirm the information of iron oxidation and spin states that are often strongly altered when decreasing size because of the different environment of iron atoms located at the surface (detailed in Section 2.2).

2.2. State of the art on SCO NPs

All of the reports on SCO NPs can be divided in three families of compounds: the mononuclear complexes with supramolecular interaction also called "molecular complexes", the 1D chain structure mainly Fe^{II}-triazole complexes with various counteranions and substituents beared by the triazole ligand and the 3D Hofmann-like CPs $Fe(L)[M(CN)_4]$ (L = bidentate ligand, M = Ni, Pd, or Pt). The elaboration and the SCO properties of nanomaterials from these families of compounds are successively discussed in the 2.2.1, 2.2.2, and 2.2.3 sections. To reach these different nano- and micro-objects, various homogeneous (soluble polymer encapsulation, acid condition, dilution, addition of nonsolvent, etc.) and heterogeneous (reverse micelles, biopolymer encapsulation, etc.) methods have been used. The influence of these approaches on the size, morphology, and SCO properties on the formed particles will be discussed and detailed throughout this section while respecting as closely as possible the chronological order of the publication of articles. A particular attention will be paid on the influence of the size reduction effect on the evolution of the SCO properties for each family of compounds but also comparing the different families.

2.2.1. Fe-triazole chain particles

One of the still relevant great challenges underlying the search for such molecule-based functional materials is to produce systems that exhibit switching properties around room temperature and with large hysteresis loop. An important family of compounds presenting such property is the Fe^{II}-triazole complexes [53,54] with 1D chain [55,56]. In 1977, Haasnoot et al. [57] reported the first example of such compound, the $[Fe(Htrz)_2(trz)](BF_4)$ complex (Htrz = 1,2,4-triazole and trz = 1,2,4-triazolato) exhibiting

a large hysteresis loop of 50 K centered at 370 K. All of these appealing properties can be exploited into applications only if reduced sized and organized objects are fabricated. Indeed, if we look at the morphology of the elements forming the bulk samples, rather polydisperse and micrometric-sized particles are observed. It is also interesting to note that in comparison with the rather spherical-shaped particles observed for most of these bulk samples of this family [58], a rod-like particles with length ranging from 300 to 800 nm were observed for the bulk sample of the $[Fe(NH_2trz)_3](NO_3)_2$ derivative. In the frame of the study of the size reduction effects on the SCO properties, different methods have been used to obtain controlled size and monodisperse NPs based on these materials.

The first results concerning the synthesis of SCO NPs were reported by Létard and co-workers [8,59,60]. These authors reported the observation of a thermal hysteresis loop in NPs of the compound $[Fe(NH_2trz)_3]Br_2$ (NH_2trz = 4-amino-1,2,4-triazole) of ca. 70 nm size obtained by the reverse micelle technique (see Fig. 6). The aforementioned NPs synthesized in the presence of nonionic Lauropal surfactant playing role of both the surfactant and oil maintained the sharp spin transition measured for the bulk powder but with a less pronounced hysteresis loop ($T_{\uparrow}$ = 311 K and $T_{\downarrow}$ = 303 K instead of $T_{\uparrow}$ = 320 K and $T_{\downarrow}$ = 300 K for the bulk).

Somewhat later, Coronado et al. [40], using a similar approach with sodium dioctyl sulfosuccinate (NaAOT) as a surfactant and octane as an oil phase, have succeeded in synthesizing spherical NPs of the $[Fe(Htrz)_2(trz)](BF_4)$ complex with a medium statistical size of ca. 15 nm, which exhibited a remarkable 43 K wide hysteresis loop with $T_{\uparrow}$ = 386 K and $T_{\downarrow}$ = 343 K. A slight temperature transition move toward lower temperature for the heating branch after successive cycles in contrast to that observed for the bulk sample was also observed. Is it interesting to notice that in this case and on the contrary to that obtained for the $[Fe(NH_2trz)_3]Br_2$ derivative, no counteranion exchange between the surfactant and complex was observed. Indeed, in the latter case, the presence of the AOT anions in the reaction medium led to the formation of the $[Fe(NH_2trz)_3](AOT)_2$ derivative [61]. More recently, such a priori not expected exchange reaction was used to synthesize monodispersed 200–300 nm plate-shaped nanocrystals of the corresponding $[Fe(NH_2trz)_3](doe)_2$ complex (doe = dodecyl sulfonate) undergoing a hysteretic (13 K) abrupt spin transition centered at 317 K [62].

One problem that researchers encounter, however, is that the SCO properties and particle size are measured in separate experiments and in different conditions. Beside the problems associated with polydispersity, the influence of solvent residues and of the matrix surrounding the particles remains difficult to control in many cases. The typical setup involves magnetic property measurement on an aggregated NP powder and TEM measurements on a small amount of particles deposited on a microscopy grid. Although an accurate correlation between size and properties (e.g., on isolated particles) is technically not yet achieved, to get more reliable results a study of the spin state fractions and particle size was realized at the same time using stable monodisperse colloidal suspensions. To this aim, NPs of the $[Fe(NH_2trz)_3](OTs)_2$ (OTs = tosylate) SCO complex of various sizes (3–40 nm) were synthesized and dispersed in a nonionic Tergitol by the direct evaporation of the polar phase of the microemulsion subsequent to the micellar exchange [63,64]. The average particle size and spin state fraction of such stable limpid purple suspension were determined in rigorously the same conditions by means of DLS and electronic absorption spectroscopy, respectively (Fig. 7). This way it was possible to provide an irrefutable proof that 10 nm NPs of $[Fe(NH_2trz)](OTs)_2$ revealed an abrupt spin transition with a hysteresis loop, whereas only a sharp transition with no detectable hysteresis was observed for 3–4 nm particles.

Moreover, while heating the colloidal suspension, the small NPs evolved into a transparent irreversible gel containing larger size spherical NPs included in the fibrous structure. Using the same water–ethanol/Tergitol binary system (Tergitol plays the role of both the surfactant and oil) and as result of the destabilization of the microemulsion by a nonpolar solvent, larger size spherical NPs ranging from 80 to 1500 nm preserving the SCO properties of the bulk were also obtained. To investigate the versatility of this approach other representatives of the $[Fe^{II}(R\text{-}trz)_3](anion)$ SCO family have been investigated as well. For this aim, $[Fe(Htrz)_2(trz)](BF_4)$ and $[Fe(NH_2trz)_3](Cl)_2$ NPs were prepared using the same conditions of microemulsion. However, in these cases, the mixture of the two initial independent microemulsions is unstable and leads to rapid precipitation of 85 and 32 nm NPs,

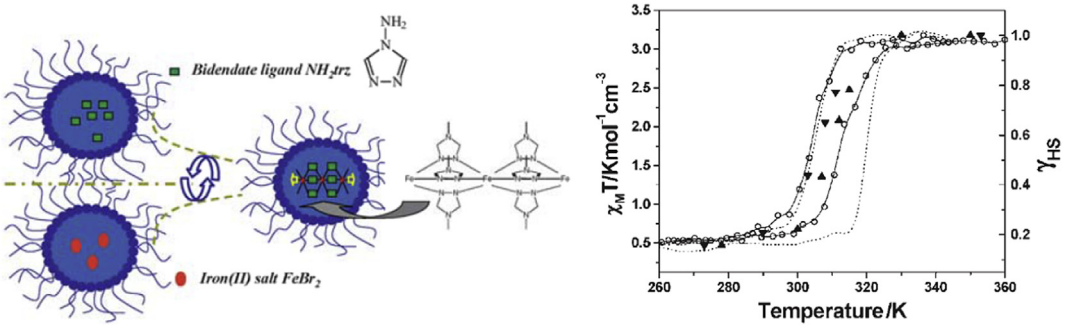

Fig. 6. Schematic representation of the reverse micelle technique used for the synthesis of $[Fe(NH_2trz)_3]Br_2$ NPs and magnetic measurements for the 70 nm particles compared with the bulk sample. Adapted from Ref. [60].

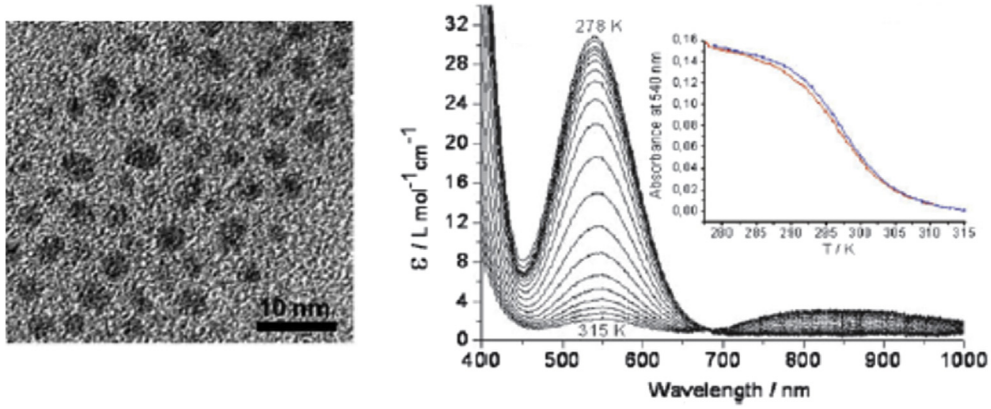

Fig. 7. (Left panel) Cryomicrotomy TEM images of 3–4 nm $[Fe(NH_2trz)](OTs)_2$ particles in a surfactant matrix. (Right panel) Variable temperature absorption spectra in the visible range and thermal dependence of the absorbance at 540 nm in the cooling (red) and heating (blue) modes. Adapted from Ref. [63].

respectively—contrary to the $[Fe(NH_2trz)_3](OTs)_2$ complex. Comparison of the obtained particle sizes reveals that the $[Fe(NH_2trz)_3](Cl)_2$ and $[Fe(Htrz)_2(trz)](BF_4)$ NPs should be formed mainly in the micelles and the particle extraction stage (solvent precipitation) does not affect considerably the particle size in these cases. This finding is in agreement with the NP sizes obtained in Ref. [60] for the $[Fe(NH_2trz)_3](Br)_2$ complex. On the contrary, the water solvated oligomeric species stabilized for the $[Fe(NH_2trz)_3](OTs)_2$ complex in the micelles form the NPs in the precipitation stage. Thus the change in the chemical composition and the reaction solvent can influence on the nucleation and the particle growth processes for the synthesis of the $[Fe^{II}(R\text{-}trz)_3](anion)$ complexes.

Study of particle size of $[Fe(NH_2trz)_3](Br)_2$ on its SCO properties was reported by Forestier et al. [65]. For particle sizes of 50 and 30 nm obtained with different ω factors (ω tends to the solvent/surfactant ratio), a relatively gradual thermal SCO occurs without clear existence of thermal hysteresis although the equilibrium temperature of the transition is almost unaffected by the decrease in the size of the NPs. The authors suggested by means of powder XRD analyses that the bistability regime implies the presence of at least five interacting coherent domains. Size effects in $[Fe(NH_2trz)_3](Br)_2$ SCO NPs with rather broad size distributions were also investigated by first-order reversal curves' magnetic measurements [66]. The study of thermal transition of such surfactant-coated NPs with average diameter d in between 30 and 110 nm revealed the presence of reversible contributions expected from particles smaller than the critical size d_C associated with the collapse of the hysteresis loop. Thanks to the reversibility property the d_C values ~45–50 nm were determined. A differential interference microscope operating in transmission mode was used to study the SCO properties of single isolated $[Fe(NH_2trz)_3]Br_2$ microparticles [67]. The comparison of the thermal hysteresis loop of several isolated microparticles demonstrates that the warming branch clearly appears more abrupt than the cooling branch and in fact, the gradual spin transition recorded for the macroscopic material does not simply result from the superposition of sharp hysteresis loops of individual particles.

The size reduction effect on the SCO properties for the $[Fe(Htrz)_2(trz)](BF_4)$ NPs was also investigated. By changing the ω factor, Galán-Mascarós et al. [68] succeeded to tune the mean size of the NPs down to 6 ± 3 nm in diameter with a narrow size distribution. A narrower 29-K wide hysteresis was found in this case (centered around 357 K), with a higher high-spin (HS) residual fraction (33%). This work was extended with a fine control of the ω factor in between 5 and 11.5 (limit of the stability of the microemulsions) affording NPs in the 4–18 nm range for $[Fe(Htrz)_2(trz)](BF_4)$ and $[Fe(Htrz)_{2.95}(NH_2trz)_{0.05}](ClO_4)_2$ complexes [69]. The latter material has been prepared with the aim of shifting the SCO phenomenon toward room temperature (Fig. 8). Importantly, for the different sizes investigated, the NPs exhibit the characteristic abruptness in the spin transition, with a significant decrease in the hysteresis width by progressive reduction in the size. Thus, relatively large hysteresis loop has been preserved even for NPs of only 4 nm (with value of 24 and 13 K for the BF_4 and ClO_4 derivative, respectively).

The effect of ligand substitution on the SCO properties and shape of $[Fe(Htrz)_2(trz)](BF_4)$ NPs was also investigated [70]. It has been shown, as previously observed for the bulk material, that the transition temperature can be gradually shifted toward room temperature, with respect to the increasing 4-NH_2-triazole quantity inclusion, reducing hysteresis width but still with abrupt spin transition. Moreover, increasing the 4-NH_2-triazole quantity inclusion, the morphology of these NPs is changing also from platelet to rod-like. Such tendency to obtain platelet rather than spherical particles for this particular $[Fe(Htrz)_2(trz)](BF_4)$ complex was clearly demonstrated by Bartual-Murgui et al. [71] synthesizing a series of different size NPs playing with the ω factor of the water/AOT/octane ternary system. One hypothesis to explain the discrepancy concerning the reported shape of the particle is related to the residual surfactant around the NPs. It seems that the presence of the surfactant induces the rods to be packed vertically on the substrate suggesting a false spherical shape. It was also shown that the presence of the surfactant tends to increase the cooperativity in the material. Indeed, the removal of the surfactant leads to the decrease in the

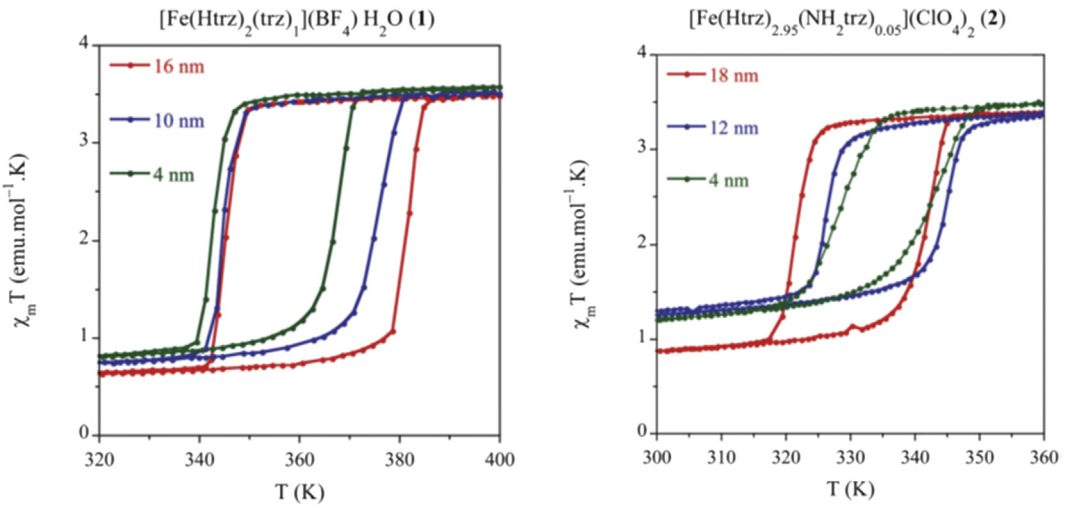

Fig. 8. Thermal hysteresis of the magnetic susceptibility (per mole of Fe) of various size $[Fe(Htrz)_2(trz)](BF_4)$ and $[Fe(Htrz)_{2.95}(NH_2trz)_{0.05}](ClO_4)_2$ NPs. Adapted from Ref. [69].

width of the hysteresis loop of ca. 15 K. On the other hand, the hysteresis width is found to increase linearly with the width of the particles until reaching values close to 40 K (raw NPs) and 20 K (washed NPs) for 20 nm NPs. Such tendencies were more recently confirmed by the rationalized study of Moulet et al. [72], which also highlighted the decrease in $T_{\uparrow}$ while $T_{\downarrow}$ is barely affected upon the NPs size reduction. These syntheses using Tergitol as surfactant and modifying both the reaction temperature and time afforded rod particles with length varying from 75 nm to 1 μm. In this study, the evolution of the crystallinity and the coherent-domain morphology was also reported including the effect of a large number of repetitive SCO thermal cycles [73]. Structural fatigability was observed at the scale of the coherent domains. A few hundred thermal SCO cycles were able to destroy the crystalline aspect of the material and such degradation in the crystalline quality was associated with a break in the $[Fe(Htrz)_2(trz)]+$ chains and confirmed by similar observations on the $[Fe(NH_2trz)_3](NO_3)_2$ derivative. On the other hand, a thermal treatment allows us to recover a better crystallinity increasing the size of the coherent domains [74]. The morphology change associated with the spin transition of similar isolated particles synthesized in a water/Triton X-100/cyclohexane ternary system was also analyzed using variable-temperature AFM (Atomic Force Microscopy) in amplitude modulation mode [75]. Significant microstructural reorganization of the particles during the low spin (LS) to HS transition, which involved a volume expansion, grain boundary changes, and a certain degree of separation of the nanocrystallites, was observed (see Fig. 9). These changes particularly important during the first switching event and only partially reversible during the reverse (HS to LS) switching can explain the observed shift of the LS to HS transition temperature between the first and second heating cycles.

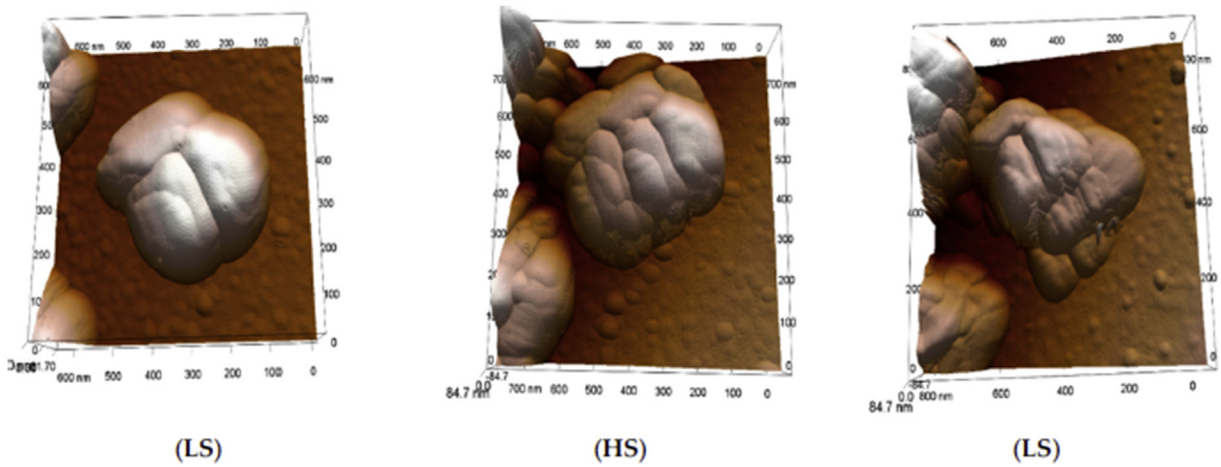

Fig. 9. AFM height images of a $[Fe(Htrz)_2(trz)](BF_4)$ particle acquired in different spin states at 358 K (in the hysteresis loop) over a complete thermal cycle. Adapted from Ref. [75].

The stability tests of the SCO properties for the $[Fe(Htrz)_2(trz)](BF_4)$ complex were also carried out for powder NP samples and electronic devices by reflectivity and electrical measurements, respectively [76]. The key finding is that the spin transition is robust to a large extent, because the powder compound can be stored for several years and the hysteresis associated with the SCO can be preserved even after several thousand thermal switches in ambient atmosphere although a progressive reduction in the width of the hysteresis loop is observed from the ca. 500th cycle. Concerning the electrical devices, the spin transition remains reproducible over several tens of cycles but the measured current decreases continuously. Such device characteristics changing with thermal cycling might be attributed to a change in the electrical contact with the interdigitated electrodes. Indeed, the device was prepared by dielectrophoresis depositing a drop of a suspension of the anisotropic $[Fe(Htrz)_2(trz)](BF_4)$ NPs under the gold electrodes. Other examples have reported the used of suspended NPs to elaborated SCO thin films or nanopatterns. In particular, homogeneous thin film maintaining the bistability properties was obtained from surfactant free, not dried (wet with ethanol), and dispersed in various solvent $[Fe(Htrz)_2(trz)](ClO_4)_2$ NPs [77]. A soft lithographic technique was also implemented to elaborate homogeneous micropatterns and nanopatterns of SCO NPs over a large area [78]. Microtransfer molding was used with an aprotic solvent (normally difficult to implement because it generates the swelling of the polydimethylsiloxane stamp) to elaborate patterns containing $[Fe(NH_2trz)_3](OTs)_2$ NPs.

A particular attention was paid to the electrical properties of $[Fe(Htrz)_2(trz)](BF_4)$ nano-objects upon SCO [79]. Using $[Fe(Htrz)_2(trz)](BF_4)$ NP powder sample or the corresponding microparticles and NPs integrated in between interdigitated electrodes by dielectrophoresis, Rotaru and co-workers [80,81] reported the spin state dependence of electrical conductivity. In both cases, the thermal variation in the measured current revealed a wide hysteresis loop centered around 370 K with the LS state being more conductive. Using similar strategy, these results were confirmed by Dugay et al. [82] The study of the metal substitution effects on the charge transport of $[Fe_{1-x}Zn_x(Htrz)_2(trz)](BF_4)$ NPs revealed a strong overall decrease in conductivity with increase in Zn concentration suggesting that the ferrous ions participate directly in the charge transport mechanism [83]. Photoconductivity experiments on $[Fe(Htrz)_2(trz)](BF_4)$ micrometric rods were also carried out [84–86]. Prins et al. [87] showed the possibility of addressing single $[Fe(Htrz)_2(trz)](BF_4)$ NP deposited between gold electrodes with an electrode gap of 5–10 nm. By plotting the conductance (I/V) of the device at 0.4 V as a function of temperature, a hysteretic behavior similar to the one obtained in the magnetic susceptibility measurements was found. Photoswitching experiments on $[Fe(Htrz)_2trz](BF_4)$ NPs synthesized in microemulsion in the presence of Tergitol were also realized [88]. Whatever the temperature of the compound, outside and within the thermal hysteresis loop, the photoswitching from the LS to the HS state is achieved in ca. 10 ns.

Alternatively, nanocomposite systems integrating an SCO functionality have been designed by embedding SCO NPs within mesoporous silica matrices. First report concerns the inclusion of preformed $[Fe(Htrz)_2(trz)](BF_4)$ complex in a xerogel using a one-step method [27]. The silica precursor mixed with a sonicated complex suspension afforded, after the gelation, aging, and drying processes, monolith or thin film containing the SCO compounds. The HRTEM (High Resolution Transmission Electronic Microscopy) analysis of the $[Fe(Htrz)_2(trz)](BF_4)$ @SiO_2 film and monolith revealed well-dispersed NPs of the Fe complex in the SiO_2 matrix, with diameter ranging from 2 to 5 nm. The composites undergo incomplete SCO behavior with temperature transition shifted toward high temperature in comparison with the bulk material mainly attributed to the SiO_2 matrix effect. In 2013, Durand et al. [30] reported the preparation and characterization of a 3 nm SCO NP–silica nanocomposite using a two-step nanocasting synthetic method by confined growth of NPs of the SCO CP $[Fe(Htrz)_2(trz)](BF_4)$ using an impregnation technique in a preformed silica xerogel matrix with well controlled porosity. The temperature dependence of the magnetization of the FeHtrz–silica nanocomposite indicated an uncompleted reversible spin transition with a hysteresis loop of 65 K width larger than that of the bulk sample. Again, it was assumed that the interactions between the NPs and the rigid silica matrix play a key role in the maintaining of a hysteresis because larger size dispersed NPs of the same complex obtained by the reverse micelle technique exhibit a much reduced hysteresis.

More recently, similar strategy was used to incorporate 2 nm cross-section nano-objects of the two polymorphs $[Fe(Htrz)_2(trz)](BF_4)$ and $[Fe(Htrz)_3](BF_4)_2$ in a commercial MCM-41 hexagonal silica matrix [89]. The Mössbauer, DC magnetic, and optical reflectivity measurements demonstrated a strong matrix effect only for $[Fe(Htrz)_3](BF_4)_2$@MCM, whereas the matrix effect for $[Fe(Htrz)_2(trz)](BF_4)$@MCM is much weaker. The explanation was associated with the presence of water for the former polymorph and suggests that water is important as a "pressure mediator" for delivering the "hydrostatic pressure" to induce a significant matrix effect (see Section 2.3). SCO@SiO_2 NPs were also synthesized using a reverse micelle technique in the presence of the precursor of the silica [90]. Such particles constitute a platform for the elaboration of various hybrid NPs (fluorescent, plasmonic) developed in the following section 3. SCO nanorod arrays were also achieved by self-assembly on a sulfonated cation-exchange polymer resist, which acted as a template to direct the growth of the nanorod arrays. By increasing the immersion time of the resin in the precursor solutions, resin beads were covered by perpendicular rods with size increasing from 250 to 750 nm [36]. The author speculated that the nucleation and growth mechanism of the SCO nanorod arrays is as follows: (1) the resin beads act as a nanoporous template with internal channels, which provide numerous ion-exchange sites for Fe^{2+} and H^+ ions; (2) the triazole organic ligands and BF_4^- anions react with the Fe^{2+} cations bound to sulfonic acid groups on the surfaces of the resin beads to generate the nucleation sites of the SCO nanorods; and (3) at the same time, the Na^+ cations diffuse into the internal channels of the resin to exchange with Fe^{2+} cations, and the exchanged Fe^{2+} cations are

released into the solution slowly and promote the consequent growth of the SCO crystal nucleus to form nanorod arrays.

SCO properties are often highly sensitive to minute aspects of the synthetic conditions, and it is of particular interest to investigate this question in the case of nano-objects. Following this idea, synthesis of $[Fe(hptrz)_3](OTs)_2$ (hptrz = heptyl-triazole) NPs by both heterogeneous (reverse micelles) [91] and new homogeneous [46] approaches using or not using different stabilizers (surfactants and polymers) was also reported. Nano-objects with various morphologies were obtained, and the relative (dis)advantages of the different approaches were discussed. The modification of both the ω factor of a water/tergitol/hexane ternary system and the concentration of the reagents does not influence drastically the size of the NPs: the average size varying from 35 to 70 nm [91]. In comparison with the bulk sample, the size reduction and the aggregation effects appear to be rather weak on the spin transition behavior. On the other hand, homogeneous synthetic pathways to obtain SCO micro- and nano-objects can bring several advantages, including (1) in contrast to the reverse-micelle technique, this process is simple and versatile, not only because various polar and nonpolar solvents can be used, but also because the whole procedure does not imply the presence of a critical step that influences the final material, such as the destabilization of the micelle phase by an additional solvent. (2) The quantity of the polymer and the solvent used for the synthesis is lower than those used in the reverse-micelle method. As a consequence, measurements of the properties are facilitated by the high concentration of the active species in the matrix. (3) The shape and size of the nano- and micro-objects can be different to those that are elaborated with the microemulsions. (4) The doping of the SCO polymer with an organic molecule (e.g., a fluorescent agent) can be more easily controlled, owing to the absence of two phases with different polarity that could provoke the undesired migration of the guest species, as in the case of a microemulsion. Following this approach, particles of the $[Fe(hptrz)_3](OTs)_2$ derivative were synthesized in the presence of various polymeric compounds as Triton X-100 (with a hydrophilic polyethylene oxide group and a hydrocarbon lipophilic group), TOPO (trioctylphosphine oxide), PVA (polyvinyl alcohol), and PEGs (polyethylene glycols) [46]. Whatever the encapsulating polymer used, quite large size particles ranging from 150 to 1500 nm maintaining the SCO properties of the bulk ($T_{\uparrow} = 318$ K and $T_{\downarrow} = 308$ K) were obtained (Fig. 10). Importantly, attempts to obtain smaller-sized objects by modifying the nature or the concentration of the polymers were unsuccessful. Nevertheless, instead of the rather spherical shape encountered for the reverse micelle syntheses, more anisotropic shapes (rods and plates), depending on the solvent used, were obtained in such homogeneous media. Here 250 nm particles of the $[Fe(hptrz)_3](OTs)_2$ derivative synthesized in the presence of PEG were used to probe the sensitivity of a novel SQUID (Superconducting Quantum Interference Device)-like magnetometry device prototype working at room temperature [92]. In this work, an ensemble of $[Fe(hptrz)_3](OTs)_2$ NPs with a volume of ca. 3×10^{-3} mm^3 has been investigated and was found to give rise to a modulated voltage signal of about 0.55 mV, which reflects the SCO properties.

The next step was to find a polymer-free synthetic pathway for the elaboration of SCO NPs, motivated by the expectation that the molecules on the surface are one of the key factors in influencing the spin transition in the NPs. It was possible to stabilize short oligomer solutions of the same $[Fe(hptrz)_3](OTs)_2$ compound without embedding it in the polymer or surfactant, by performing the reaction in a specific solvent mixture [46]. The reaction between $[Fe(H_2O)_6](OTs)_2$ and hptrz in chlorinated organic solvents, such as $CHCl_3$ or trichloroethylene, in the presence of alcohols (up to 5% v/v) yielded relatively stable solutions of a low-level "polymerization" SCO complex. The addition of

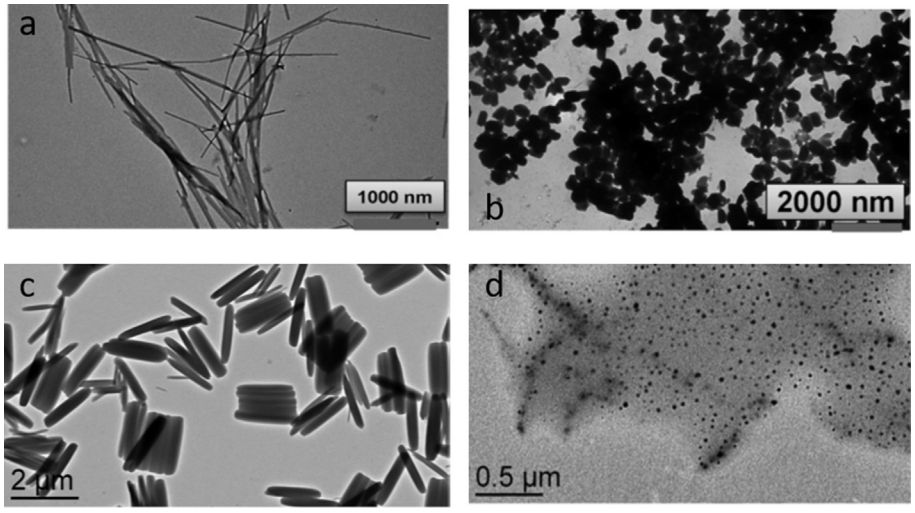

Fig. 10. TEM images showing various sizes and shapes of $[Fe(hptrz)_3](OTs)_2$ NPs obtained in homogeneous media. (a) Synthesis in the presence of Triton X-100; (b) synthesis in the presence of PEG; (c) slow precipitation from an oligomer $CHCl_3$ solution; and (d) fast precipitation from a fresh oligomer solution with PEG. Adapted from Ref. [46].

alcohols effectively prevents the gelation of the complex. The alcohol can play the role of a terminal ligand, slowing down the growth of the oligomers into larger structures. The alcohol has an exclusive influence on the stabilization of the oligomer solution without gelation; in contrast, the use of DMF or DMSO provokes the direct formation of a fibrous gel structure. A few seconds after mixing the reagents, the color of solution turns pink, thus indicating the formation of the LS complex. DLS measurements as a function of time show the presence of 6.5(±2) nm objects in fresh solution and their growth into microstructures over 24 h. Slow growth of the oligomers occurs within a few hours of mixing the reagents until the mean size reaches 8.5 nm; then, a fast and spontaneous formation of about 400 nm crystals takes place with a subsequent gradual increase to about 1400 nm. Alternatively, the addition of PEG-3350 chloroform solution to the initial and diluted oligomer solution results in the formation of colloidal solutions of small NPs of 23(±5) and 6.2(±1.8) nm, respectively (Fig. 10). The properties of such smaller NP studied by optical-reflectance measurements revealed a transition temperature shift of approximately 10 K; the more important observation being the gradual manner in which the spin transition occurs.

Such types of oligomer solution can be extremely useful for the preparation of SCO thin films by spin coating onto different substrates and for the elaboration of nanopatterns by means of soft lithography, as recently reported [93–95]. The importance of obtaining stable nano-objects without the presence of large amounts of additives has been underlined for the surface deposition and patterning of the particles. Indeed, dilution of particles in a surfactant can be a serious obstacle in the study of the SCO properties, and in particular, the electrical and optical properties of the particles can be completely masked by the matrix.

A similar surfactant-free homogeneous approach was used to synthesize homochiral coordination NPs of $[Fe(NH_2trz)_3](L\text{-}CSA)_2$ (NH_2trz = 4-amino-1,2,4-triazole, L-CSA = L-camphorsulfonate) [96]. Acetonitrile was used as a solvent and stabilizer to prevent the aggregation of the ca. 50 nm NPs. The introduction of the chiral anion to the coordination framework makes these NPs display specific chiro-optical (circular dichroism) properties that are different in HS and LS states.

An original homogeneous acid medium method was also used to synthesize controlled size surfactant/polymer-free nanorods and microrods based on the BF_4 (tetrafluoroborate) and CF_3SO_3 (triflate) derivatives of the Fe-triazole family of compounds [97,98]. The control of the size was realized by modifying the acid concentration. In the case of the BF_4 derivatives, all of the physical characterizations revealed a correlation between the size of the particles and their composition, the smaller rods correspond to the $[Fe(Htrz)_2(trz)](BF_4)$ complex with a spin transition localized at high temperature ($T_{1/2\,(\downarrow)} \approx 352$ K and $T_{1/2\,(\uparrow)} \approx 397$ K), whereas the longer ones correspond to the fully protonated ligand $[Fe(Htrz)_3](BF_4)_2 \cdot 3H_2O$ derivative, which presents a spin transition just below room temperature ($T_{1/2(\downarrow)} \approx 265$ K and $T_{1/2\,(\uparrow)} \approx 278$ K for the dehydrated compound) [97]. In fact, high concentrations of acid, which preclude the deprotonation of the Htrz ligand associated with a slow evaporation speed of the complex solution, lead to the slow stabilization of the $[Fe(Htrz)_3](BF_4)_2 \cdot 3H_2O$ long rod-shaped particles, whereas short rod-shaped $[Fe(Htrz)_2(trz)](BF_4)$ particles are obtained for low acid concentrations. Thus, it is demonstrated that not only the size but also the morphology of the objects for a considered material can be tuned. A similar homogeneous acid condition was used for the elaboration of highly anisotropic acicular rods of the CF_3SO_3 derivatives as well [98]. Syntheses in the absence or in the presence of low concentration of acid allowed us to stabilize rod-shaped particles of the $[Fe(Htrz)_2(trz)](CF_3SO_3)$ derivative, which presents a rather low temperature SCO behavior as compared with other compounds of this family with $T_{1/2(\downarrow)} \approx 162$ K and $T_{1/2(\uparrow)} \approx 166$ K for the dehydrated form. In contrast, incorporation of larger concentration of acid as for the BF_4 derivative led to the precipitation of microrods of the $[Fe(Htrz)_3](CF_3SO_3)_2$ form. This new compound presents a large hysteresis loop of 50 K perfectly centered at room temperature ($T_{1/2(\downarrow)} \approx 278$ K and $T_{1/2(\uparrow)} \approx 327$ K). Such properties are very scarce and even unique for shaped materials. Indeed, although hysteretic SCO at room temperature is a prerequisite to go toward several applications, the possibility to obtain regular and organized nano- and micro-objects is also crucial. In fact, such simple experiments led to the elaboration of already-shaped SCO objects with very appealing properties, which will be certainly beneficial to undertake the relevant great challenges concerning both fundamental and applied perspectives. In particular, these very high aspect ratio bistable objects could be really useful using soft lithographic approaches or the dielectrophoresis to understand the spatiotemporal behaviors and the transport properties of organized individual objects, which constitute one of the foremost paradigms in molecular electronics. Moreover, the largest measured “real” room temperature bistability reported for these objects is very promising for practical application in the fields of memory devices, display devices, inkless paper, and micro-electromechanical systems.

Different SCO NP morphologies were also obtained using a spray-drying method, which is a method to transform aqueous solution into powders [52]. In the case of the CP $[Fe(Htrz)_2(trz)](BF_4)$ (Fig. 11), the SCO properties of the spherical particles differ from those of the referenced materials, in the sense that SCO is more gradual and incomplete, in adequacy with a poor crystallinity. It is interesting to notice that such techniques commonly used by food and pharmaceutical industries permit to produce in a simple manner a large quantity of material. In this research axe, fluidics methods have become well established as the benchmark method of NP production. Very recently, millifluidics methodology was used to control and increase the NP production. Thus, the first flow synthesis of $[Fe(Htrz)_2(trz)](BF_4)$ particles in a milliscale segmented flow crystallizer has been reported (Fig. 11) [51].

The ensemble of results concerning compounds of the triazole family seems to indicate that the evolution of the SCO properties is not only dependent on the size but also critically on the chemical nature of the compounds and certainly more precisely on the structural arrangement of

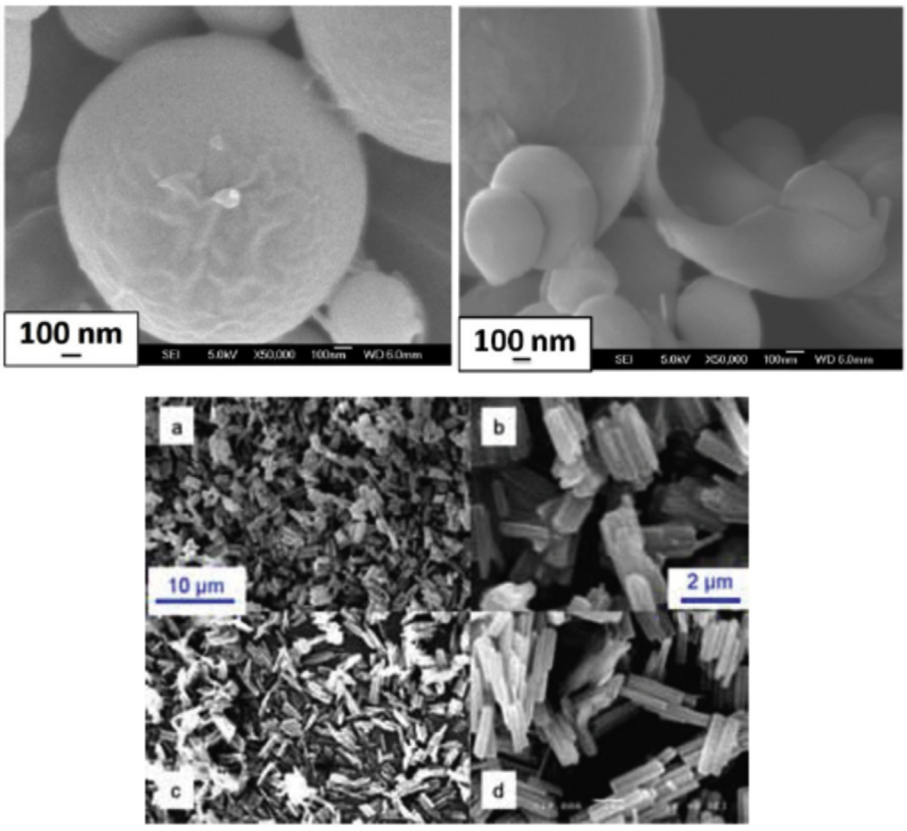

Fig. 11. Scanning electron microscopy (SEM) images of $(Fe(Htrz)_2(trz))(BF_4)$ synthesized by spray drying (top) and millifluidic methods (bottom). Adapted from Refs. [51,52].

the chains, which is influenced by the nature of the ligands and that of the counter anions and (in certain cases) by solvent molecules. Unsubstituted triazole ligand in $[Fe(Htrz)_2(trz)](BF_4)$ and tosylate OTs counter anion in both $[Fe(NH_2trz)_3](OTs)_2$ and $[Fe(hptrz)_3](OTs)_2$ seem to favor strong interactions between the adjacent chains, presumably by means of hydrogen bonds possibly through solvent molecules. This cooperative effect could explain the maintaining of the first-order spin transition in these compounds even at the nanometric scale.

2.2.2. *Three-dimensional Hofmann-like clathrate NPs*

Different synthetic approaches have also been reported for the elaboration of Hofmann-like clathrate 3D network $[Fe(L)\{M(CN)_4\}]$ (L = bridging ligand as pyrazine (pz), azopyridine (azpy), etc., M = Pt or Ni) NPs. The water-in-oil microemulsion technique has been used by both Boldog et al. [99] and Volatron et al. [100] to prepare various sized (8–250 nm) nanocrystals of the $[Fe(pz)\{Pt(CN)_4\}]$ compound (Fig. 12). In all cases, using a water/AOT/octane ternary system, the control in the size was achieved by modifying the concentration of the precursors and thus the ω factor. The study of the magnetic properties revealed that upon a reduction in the size, particles display SCO behavior, which is different from the bulk. In the anhydrous forms of these nano-objects, the observed modification of the transition temperature, the hysteresis width, the abruptness of the transition, and the residual fractions were related to the size reduction effect (Fig. 13).

Adapting the microemulsion synthesis, van der Veen et al. [101] obtained $600 \times 600 \times 30$ nm^3 $[Fe(pz)\{Pt(CN)_4\}]$ nanocrystals and studied the thermal and photoinduced spin state switching on the nanosecond scale for single objects using 4D electron microscopy. In comparison with the measurements on an assembly of particles, a more gradual thermal spin transition with a smaller hysteresis loop has been detected for the isolated particle and the dynamics is significantly faster. Sagar et al. [102] reported a femtosecond time-resolved spectroscopic study of size-dependent dynamics in nanocrystals of the same material. It was observed that smaller NPs (123 or 78 nm cross-section) exhibit SCO with time constants of ~5–10 ps whereas a ~20 ps time scale is measured for larger NPs (375 nm cross-section). The authors suggest that the SCO is less efficient in larger NPs owing to their larger size and hence lower residual LS/HS fractions.

The 2D SCO polymers $[Fe(3\text{-}Fpy)_2\{M(CN)_4\}]$ (M = Ni, Pd, Pt) were also nanostructured in the form of nanocrystals and NPs [45]. Surfactant-free nanocrystals of average length of 400 nm were synthesized from water-in-oil microemulsions, whereas smaller size NPs ranging from 200 to 70 nm were only obtained in PVP-coated polymer. The SCO process is drastically influenced by the dimensions of the crystal/particle. The large nanocrystals exhibit a

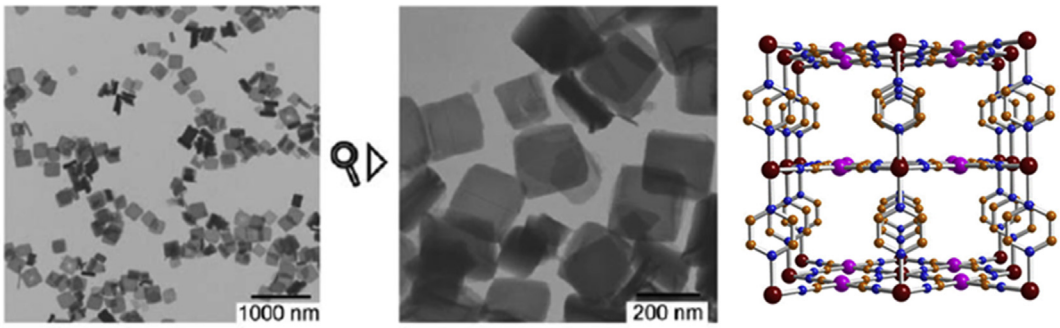

Fig. 12. TEM images of nanocrystals of the [Fe(pz){Pt(CN)$_4$}] complex and its schematic crystal structure. Adapted from Ref. [99].

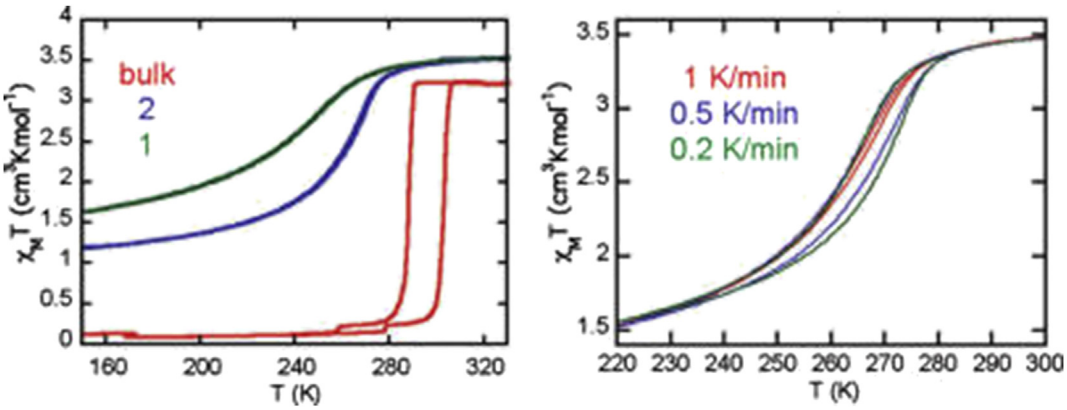

Fig. 13. Magnetic properties of nanocrystals of [Fe(pz){Pt(CN)$_4$}] of 15 × 15 × 5 (2) and 8 × 8 × 3 (1) nm^3 size compared with that of the bulk. Adapted from Ref. [100].

quasi-complete first-order spin transition centered within the interval 200–225 K, whereas all PVP-coated NPs undergo continuous second-order spin transition at much lower temperatures (ca. 160 K). The nanostructuration of both 2D and 3D Hofmann-like clathrate polymers has provided better insight into the correlation between the maintaining of the cooperativity at reduced size and the dimensionality of the polymer. Despite SCO materials based on the 2D polymers and the 3D one [Fe(pz){Pt(CN)$_4$}] feature cooperative "efficiency" for the bulk material, the 2D polymer NPs (200 nm), undergo incomplete second-order spin transition whereas first-order transition is still observable for the 3D polymer nanocrystals (15 nm). This experimental fact clearly demonstrates, as anticipated, that the 3D polymer enables better cooperativity of the spin transition process.

The synthesis of ultrasmall NPs of the SCO CP [Fe(pz){Ni(CN)$_4$}] analogue was also demonstrated by using chitosan biopolymer as matrix [103]. Chitosan is a natural biopolymer obtained by deacetylation of chitin (poly-*b*-(1,4)-acetylglucosamine) from seafood industry waste (crab and shrimp shells and squid pens) and more rarely from fungi [104]. The procedure was adapted from the multilayer sequential assembly process developed for the preparation of the corresponding thin films [105]. The advantages of this strategy consist of (1) the possibility to covalently anchor the cyanide-bridged metallic network at the reactive functional amino groups of the chitosan; (2) the possibility to afford ultrasmall NPs (less than 10 nm corresponding to the natural size of pores into the chitosan polymer); (3) the water solubility of the chitosan matrix that permits removal of the NPs from the matrix. Thus, the porous chitosan beads allow the reproducible growth of ~4 nm NPs with a narrow size distribution (Fig. 14). The study of the physical properties of these nanocomposite beads notably by Mössbauer spectrometry revealed that only ca. 1/3 of the Fe^{II} ions of the NPs undergo a cooperative thermal spin transition with a hysteresis loop. The decrease in the fraction of iron ions involved in the spin transition in comparison with powder or larger sized NPs may be related to the high percentage (ca. 2/3) of iron ions localized at the surface of the NPs. Indeed, it can be suggested that the different environments around the iron atoms localized at the surface, in comparison with those inside the NPs, can lead to the loss of the SCO properties. Thus, in contrast to that was expected, it seems that even very small particle (3–4 nm) with a few hundreds of SCO metal ions can exhibit high cooperativity. However, if we compare the magnetic properties of the same NPs with comparable size previously obtained by using the reverse micelles method showing more gradual conversion, we can conclude that in the present case the preservation of the cooperativity and

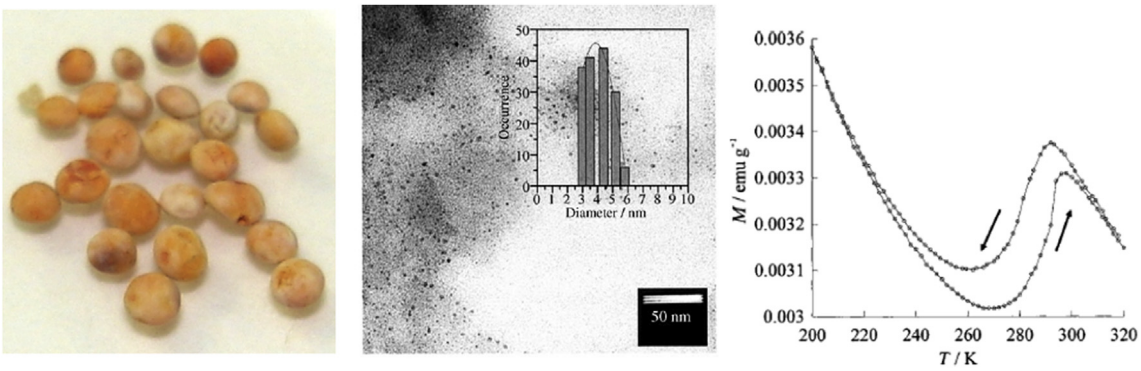

Fig. 14. (Left) Photograph of the nanocomposite chitosan beads containing [Fe(pz){Ni(CN)$_4$}] NPs. (Middle) TEM images of the NPs within the chitosan beads; the inset shows the size distribution histogram of the NPs. (Right) Temperature dependence of the magnetization measured for the nanocomposite beads at heating and cooling rates of 0.5 K min^{-1}. Adapted from Ref. [103].

the hysteresis loop should be explained by the specific matrix effect generated by the chitosan polymer (see Section 2.3).

The reverse nanoemulsion technique was also used for the elaboration of different size [Fe(pz){Ni(CN)$_4$}] NPs [106]. With the objective to reach sizes down to 2–3 nm both the preparation of the starting nanoemulsion and the micellar exchange reaction were performed at low temperature. By modifying both the temperature and the concentration of the reactants NPs with sizes from 2 to 110 nm could be obtained. It is interesting to note that a significant change in the color of the powder samples could be observed as a function of the particle size. The darkening of the sample can be explained by the increasing residual LS fraction at room temperature when the size of the NPs decreases. When decreasing the size of the particles from 110 to 12 nm the spin transition shifts to lower temperatures, becomes gradual, and the hysteresis shrinks in agreement with the result reported for the platinate derivative (Fig. 15). On the other hand, a reopening of the hysteresis was observed for smaller (2 nm) particles.

A detailed ^{57}Fe Mössbauer spectroscopy analysis was used to correlate this unusual phenomenon to the modification of the stiffness of the NPs, thanks to the determination of their Debye temperature. This study clearly showed that elastic properties of NPs can change with the particle size. One hypothesis is that the surfaces are more rigid than the core of the particle. For the first time, a size decrease would lead to a decrease in cooperativity until a certain size. Then the influence of surfaces would become greater and there would be an increase in cooperativity. To better understand this phenomenon, the elastic properties of SCO particles with sizes between ca. 3 and 30 nm have to be explored systematically and confronted with the theoretical models [107–120]. To complete this study, the size evolution of lattice dynamics in SCO coordination NPs through nuclear inelastic scattering (NIS) was also investigated [121]. Vibrational properties in these bistable molecular materials are of paramount importance and NIS permits to access the partial vibrational density of states in both spin states from which thermodynamical and mechanical properties can be extracted. It was shown that the size reduction leads to the presence of inactive metal centers with the coexistence of HS and LS vibrational modes [122]. Moreover, the confinement effect has only weak impact on the vibrational properties of NPs, especially on the optical modes, which remain almost unchanged. On the other hand, the acoustic modes are much more affected, which results in the increase of the vibrational entropy and also the Debye sound velocity in both spin states. This stiffening may be because of the elastic surface stress exerted by the external environment. An evidence of the

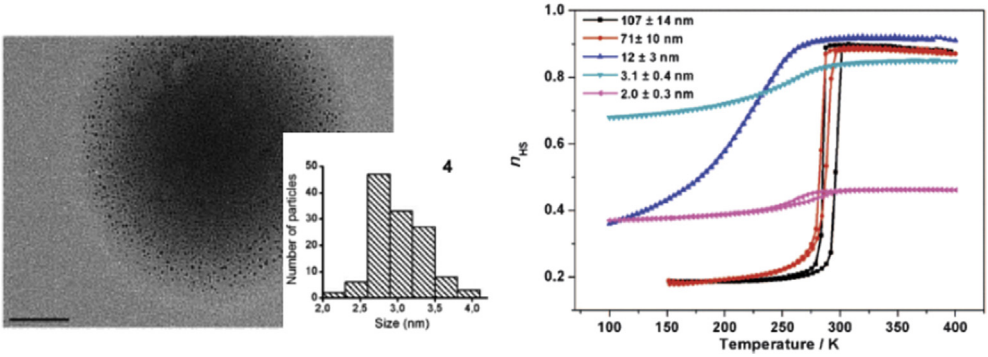

Fig. 15. (Left) TEM image and the associated size distribution histogram for ca. 3 nm. (Right) Calibrated $n_{HS} = f(T)$ curves for different size NPs from combined magnetic and Mössbauer measurements. Adapted from Ref. [106].

influence of the host matrix on the vibrational properties of the NPs is also highlighted through the matrix dependence of the sound velocity.

With the preceding results in mind, it is important to mention that the size–properties relationship should be closely related to the dimensionality of the materials. The 1D Fe^{II} triazole CPs should contain a less important fraction of inactive terminal iron ions and thus the effect of size reduction might be amplified for the 3D systems like the Hofmann clathrate networks. We would like to stress also that the modification of the transition properties between the powdered sample and the NPs may not only occur because of the decreased number of interacting SCO centers, but also because of the increased number of defects—in particular surface defects—and structural relaxation. Moreover, the difference in cooperativity observed for particles of similar size (and shape) of the same compound seems to be related to the different synthesis methods. The various synthesis methods lead to different crystallinity, defects (including the chemical environment of the metal centers at the surface of the particles), and also they provide different physical environment around the NPs (matrix effect).

2.2.3. Molecular complex particles

A particular interest in this system is that the NPs are composed of discrete SCO molecules in contrast to CPs (1D–3D). The surface termination of these latter is not well defined, and the coordination environment of the transition metal ions can be seriously altered at the surface of the particle. This problem is more likely avoided in the case of molecular nano-objects, although in the case of ionic complexes, the relative location of counterions near the surface may differ from what is observed in the core of the particle. The same uncertainty as to comparative position also applies if solvent or other guest molecules are present in the structure, and differences in intermolecular interactions (e.g., H-bonding) must be also observed at the surface.

The first report concerning the elaboration of NPs based on molecular SCO complexes was reported by Tissot et al. [28]. In this study, a silica polymeric gel is used to control the kinetics of nucleation and growth of the $[Fe^{II}((mepy)_3tren)](PF_6)_2$ complex; the reference bulk powder sample exhibiting a gradual HS to LS crossover centered at 160 K. This approach leads to spherical particles of controlled size ranging from 730 (±80) to 47 (±10) nm homogeneously dispersed in transparent silica thin films obtained by spin coating. With respect to the bulk reference compound, the SCO curves afforded by the NPs do not significantly vary. The photoswitching properties based on LIESST are probed by UV–vis and magnetic measurements. As observed for the crystalline pure sample, the NPs embedded in silica thin films can be efficiently photoexcited and no size effect has been detected on the relaxation kinetics. Tissot et al. [123] reported also the elaboration and the SCO properties of micro- and nanometric particles (down to 18 nm, Fig. 16) of $[Fe^{III}(3\text{-MeO-SalEen})_2]PF_6$ (H-3-MeO-SalEen being the condensation product of 3-methoxy–substituted salicylaldehyde and *n*-ethylethylenediamine). A precipitation method in an antisolvent was used to produce objects whose size and shape can be modulated by varying the experimental conditions. Another interesting issue, which should be remarked upon concerning this compound, is that the larger objects crystallized as long needles (7500 × 640 × 215 or 3500 × 350 × 125 or 950 × 270 × 35 nm^3). Such "1D" nano-objects (nanorods, nanowires, etc.) only appeared in the SCO literature recently, and mainly (although perhaps not surprisingly) comprise Fe^{II}-triazole complexes whose crystal structure consists of "infinite" chains of the Fe complexes [55]. Such high aspect ratio SCO nano-objects may exhibit singular properties (mechanical, thermal, etc.), and they should be more easily organized and manipulated at the nanoscale, thanks to their particular shape.

A decrease in the cooperative character (from first order to gradual crossover) with decreasing size was reported, whereas the transition temperature and the completeness of the transition were found to be only marginally altered. Needle-shaped crystals of this compound were embedded in PVP to probe their photoswitching properties [124]. The optical spectroscopy measurements revealed a femtosecond switching associated with an increase in the photoconverted molecules in comparison with macroscopic single crystal. Similar precipitation method was also used to prepare crystalline NPs of the $[Fe^{II}((mepy)_3tren)](PF_6)_2$ complex [125]. The photoinduced relaxation dynamics was

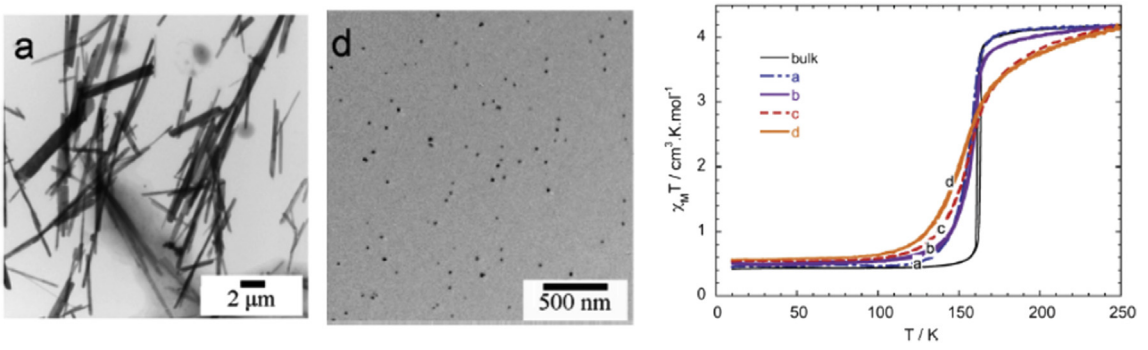

Fig. 16. TEM and magnetic properties of $[Fe^{III}(3\text{-MeO-SalEen})_2]PF_6$ particles with length ranging from 18 nm (d) to 8 µm (a) (b = 950 nm and c = 3.5 µm). Adapted from Ref. [123].

studied and compared with those of the similar size (ca. 70 nm) amorphous NPs of the same compounds obtained by the sol–gel approach [28]. The HS to LS relaxation kinetics are significantly different in terms of time scale, that is, 10^{-1} versus 10^{4} s at 40 K, and shape, that is, single exponential versus stretched exponential, between crystalline and amorphous particles, respectively. Amorphous particles have a lower transition temperature because of the less-dense packing ($T_{1/2} = 225$ K for the crystalline NPs and $T_{1/2} = 125$ K for the amorphous NPs). This arrangement results in slower relaxation kinetics than in the crystalline particles.

Alkylated derivatives of the [Fe(sal_2-trien)] complex, where sal_2-trien is the hexadentate N_4O_2 bisimino ligand formed by the condensation of salicylaldehyde with N_1,N_2-bis(2-aminoethyl)-1,2-ethanediamine, were investigated to form nanowires by template assembly in nanoporous anodic aluminum oxide [35]. Nanowires of ca. 80 nm diameter and 5–10 μm length were released using a phosphoric acid to dissolve the template. SQUID and Raman measurements on both the templated and not templated material confirmed that SCO persisted in the nanoassembly, although the profile is less complete than for the bulk powder.

A new mononuclear SCO compound [Fe(AP-Mesal)$_2$] (AP-Mesal = 2-hydroxy-3-methyl-*N*-((pyridin-2-yl)-ethylidene)benzohydrazide) exhibiting SCO properties near room temperature was synthesized as microparticle and NP in the presence of PEG-400 modifying both the concentration of reactants and the quantity of polymer [126]. In agreement with the magnetic measurements of the crystals, small hysteresis widths of about 4–6 K were observed when the particle size is on the microscopic scale. When the particle size is further reduced to 30–50 nm, the hysteresis width becomes more pronounced (about 10 K). The authors underline this uncommon behavior and assume that its origin is dominated by the size distribution of the particles even if the high surface area of the small NPs should play a key role.

The size reduction effect on the SCO properties of particles of the prototypical [Fe(phen)$_2$(NCS)$_2$] complex was also investigated. The precipitation method [127] or the reverse micelles method [39] was used to synthesize such NPs and microparticles. Using the precipitation method for the diamagnetic [Fe(phen)$_3$(NCS)$_2$] precursor, followed by a thermal treatment, Laisney et al. [127] elaborated an array of crystalline objects with sizes varying from 15 to 1400 nm. The salient features are a cooperativity preserved at the micrometric scale, a very limited downshift in the transition temperature, and an asymmetric spreading of the thermal process (over ca. 100 K) with the size reduction although the process appears to be quasi-complete whatever the size of the samples. Similar result were also obtained with the more gradual and high temperature SCO [Fe(Me$_2$-bpy)$_2$(NCSe)$_2$] NPs [128]. At the same time, surfactant-free [Fe(phen)$_2$(NCS)$_2$] nanocrystals with dimensions ranging from 203 × 203 × 106 to 142 × 142 × 74 nm and elaborated after a reverse micelle method were also reported by Valverde-Muñoz et al. (Fig. 17) [39]. It was found that the smaller nanocrystals undergo an abrupt and more cooperative spin transition in comparison with the bulk compound with a spin transition centered in the interval of temperature of 175–185 K and with an 8 K hysteresis loop. Nevertheless, the crystallite quality more than the crystallite size seems to be responsible for the higher cooperativity. Such [Fe(phen)$_2$(NCS)$_2$] objects were also investigated in studies for the comprehension of the influence of the environment (matrix) on the SCO properties (see hereafter).

2.2.4. Other CP NPs

Particles of the SCO CP [Fe(NCS)$_2$(bpe)$_2$] [bpe = 1,2-bis(4-pyridyl)ethane] have been prepared by water-in-oil reverse micelle methods using Ifralan D0205 as a surfactant [129]. Although keeping constant the reactant concentration and modifying the mass of surfactant, particles sizes ranging from 1–4 μm to 30–80 nm were obtained (Fig. 18). Comparison of the magnetic properties with those of the macroscale crystals revealed that the spin transition becomes more gradual, more incomplete, and concomitantly the transition temperature ($T_{1/2}$) decreases with particle size reduction. The study of the effect of the particle size reduction on the light-induced spin state switching at 10 K was also reported. According to the authors, one of the most important results of this study is the retention of the same light-induced SCO effect whatever

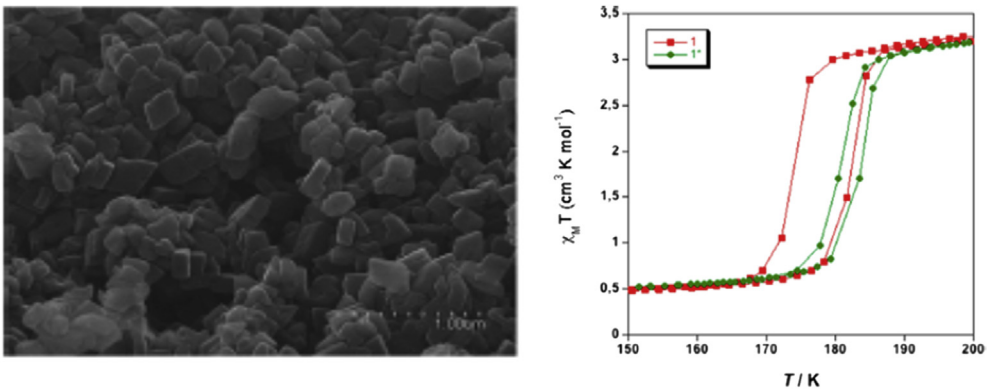

Fig. 17. SEM image and magnetic properties of 203 × 203 × 106 nm nanocrystals of [Fe(phen)$_2$(NCS)$_2$] (sample 1* corresponds to similar size particle sample but with defects on the surface). Adapted from Ref. [39].

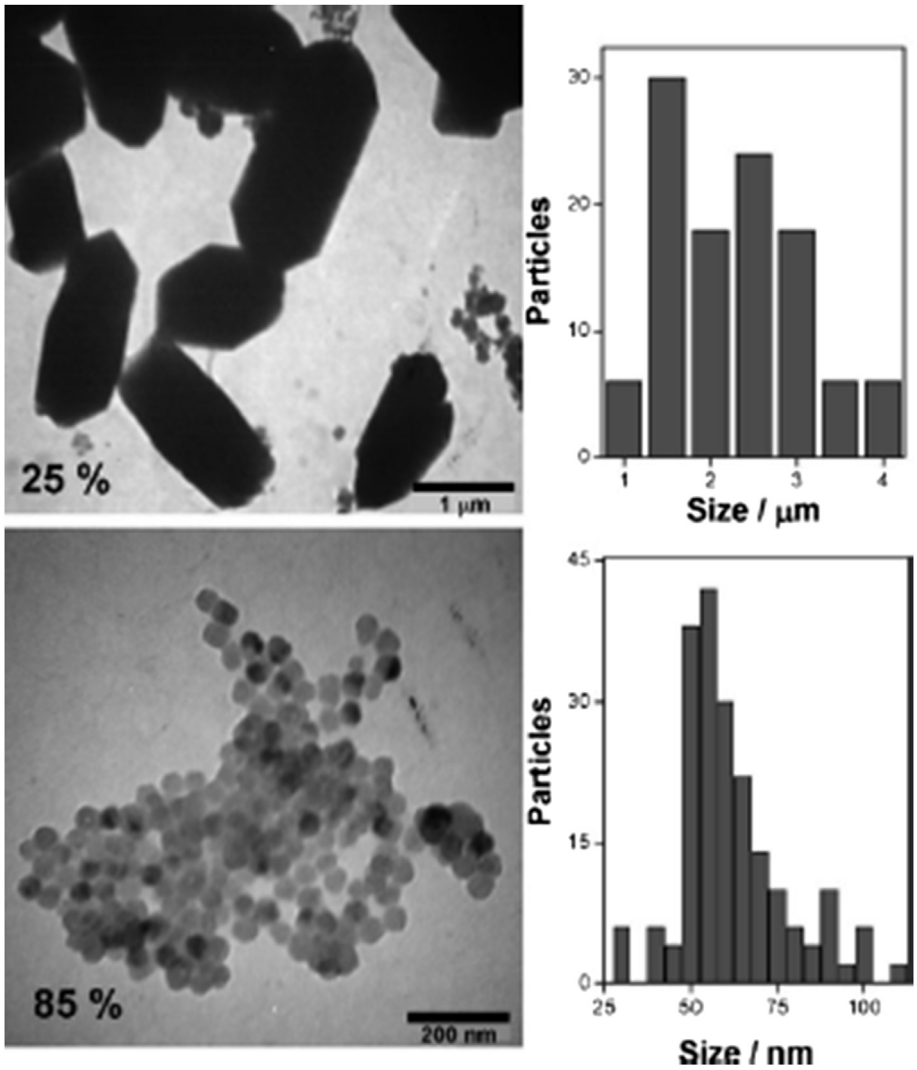

Fig. 18. Representative TEM images of $[Fe(NCS)_2(bpe)_2]$ NPs including size distribution histograms. Adapted from Ref. [129].

the size of the particles, highlighting that the light-induced SCO properties are governed by the molecular scale, whereas the thermal SCO regime is governed by solid-state cooperative interactions.

More recently, Weber and co-workers used a polystyrene-poly-4-vinylpyridine–based BCPs known for their ability to build micellar structures as a template for the NP synthesis of the CP [Fe(L)(bipy)]*n* (with L = 1,2-phenylenebis (iminomethylidyne)bis(2,4-pentanedionato)(2-) and bipy = 4,4′-bipyridine) [43,130]. The progressive growth of the CP chains attached to the pyridine functions of the BCP affords the formation of core–shell NPs with a constant size (50 nm) increasing crystallinity CP core (Fig. 19).

2.3. Matrix and surface effects on SCO properties

A major point that has been questioned for the past years and that is still under investigation is the crucial role of the matrix and interface. Puzzling differences between the SCO behaviors were reported in the first studies dedicated to SCO NPs. Some differences were observed on the cooperativity of the iron triazole derivatives, but they were more related to the nature (ligand and counterion) of the compounds themselves. More intriguing were the large discrepancies in the Hoffman clathrate family: although NPs of 7 nm of the $[Fe(pz)\{M(CN)_4\}]$ (M = Pt, Ni) were found to have a partial and gradual SCO without any hysteresis aperture [100], 4 nm particles of $[Fe(pz)\{Ni(CN)_4\}]$ embedded in chitosan beads revealed a large thermal hysteresis loop close to room temperature (although with a large proportion of remaining HS Fe^{II} sites) [103]. Moreover, partial washing of the surfactant was shown to have a tremendous effect on the SCO properties [44]. These examples have emphasized the importance of carrying out studies on NPs that are fully characterized (in composition, crystallinity) and comparing samples not only with respect to the size but also consider the influence of shape and more importantly of the environment. Even if later on the

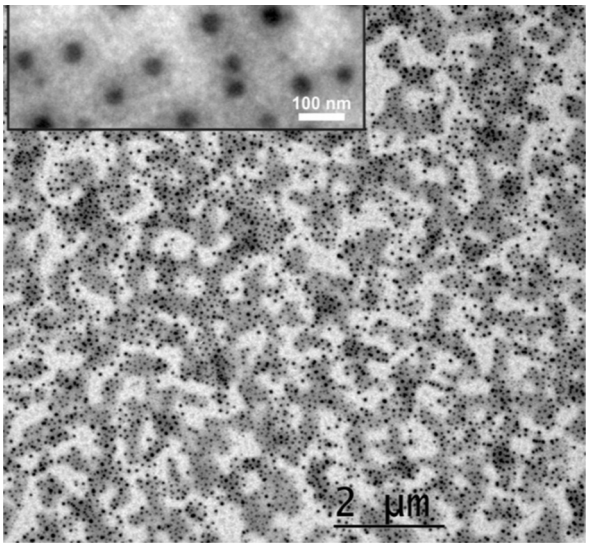

Fig. 19. TEM characterization of the CP–BCP composite micelles at two different magnifications illustrating the core–shell nature of the particles. Adapted from Ref. [43].

reaperture of a hysteresis loop was demonstrated a size of less than 4 nm [106], the effect of the surrounding does have an importance of the rigidity of the surface (see subsequently). From an experimental point of view, having the same environment represents a big challenge for chemists as tuning size requires the use of different methods or surfactant-based approaches. Even traces of surfactants may interfere and modify the SCO behavior. Ideally, self-standing particles without any stabilizer should be targeted to avoid these effects, but this is not straightforward if one targets sub-100 nm NPs.

A first experimental demonstration was reported by Raza et al. [41] in 2011 on $10 \times 10 \times 5$ nm^3 nanoplatelets of [Fe(pz){M(CN)$_4$}] (M = Pt, Ni) that were surrounded by a coating of variable nature without any contamination by the surfactant, to clearly evidence the surrounding effect maintaining the core size, crystallinity, and shape the same. Using the strong anchoring of the eight pyridine groups to the Fe^{II} surface sites of a modified calixarene leads to full washing of the surfactant while remaining crystalline. Importantly, these particles can be dispersed, thanks to this coating in dichloromethane showing that no coalescence occurred. Besides, an inorganic silica shell was grown on similar cores at different thicknesses to probe the effect of the nature/compressibility on the SCO behavior. When the samples contain AOT (before washing), partial and gradual SCO was observed whatever the coating's nature and thickness, whereas full washing induces the appearance of a hysteresis loop only in the case of a thin silica shell (around 2 nm). The calixarene-coated sample has a similar transition temperature but without any hysteresis. These observations show how only the nature of the surrounding (of similar thickness) can affect the elastic interactions at the origin of cooperativity. Growing a slightly thicker silica shell of 5 nm by exactly the same process leads to no hysteresis and lower transition temperature (Fig. 20). This points out that the behavior may not only relate to the interface between the particle and the matrix as it is exactly the same type of interaction between silica and particle surface, but both the thickness and rigidity of the matrix may play a role. One hypothesis suggested by these results was that only a *thin rigid* matrix acts as an efficient coating for propagating elastic interactions. Both a more compressible (organic) or thicker shell (rigid or soft) may prevent these elastic interactions to be operative.

The hypothesis proposed in the original article was that propagation of acoustic waves occurs in between NPs throughout a thin rigid layer when it is hampered by thick shells or thin compressible shells. This hypothesis was proposed because with exactly the same silica/particle interface, the SCO behavior still depends on the silica thickness. However, propagation of phonons through amorphous solids is not a trivial issue, and in this case the chemical bonding between the silica shells may play a very specific role as underlined recently [131]. Even if *interparticle* elastic interactions may be seriously questioned, the conclusion may be similar regarding the particle itself: *intraparticle* elastic interactions may be operative only with a thin rigid shell when empeeded with thick and/or compressible shells. This has been illustrated by an electroelastic model by Boukheddaden and co-workers [108,132] that have calculated the internal pressures in the core and the shell depending on their respective thicknesses using 2D core–shells; the authors suggest importantly that acoustic impedance mismatch between the core and the shell may be detrimental to the cooperativity.

The influence of the matrix has been first modeled by Stoleriu et al. [133] with a mechanoelastical model based on Monte Carlo calculations using an elastic spring constant representing the interaction of the matrix (polymer, surfactant, and ligand) with the particle surface. The main idea is that the presence of the matrix on the edges lowers the switching probability from LS to HS and leads to a more incomplete more gradual transition when this elastic spring constant k_{pol} is increased. This simple model is very efficient to rationalize the significant matrix effects that were reported in 2012 on large micrometric SCO particles of molecular complexes by Tissot et al. [134] for microcrystals of [Fe(phen)$_2$(NCS)$_2$], the effect of surface is negligible as compared with NPs of extended CPs where the environment at the surface is strongly modified. The coordination sphere around the Fe^{II} remains the same whatever the location, even if slight distortion may occur and for ionic compounds the organization of the counterions at the surface may not be strictly comparable. In any case, the proportion of surface atoms for microcrystals represents less than a few percent. [Fe(phen)$_2$(NCS)$_2$] microcrystals postembedded in different matrices, such as PVP or PEG display different SCO behaviors, with a more gradual SCO for the PVP composite. When heating the PEG sample above its glassy transition (T_g) and cooling down again, the recrystallized PEG sample displays an SCO behavior similar to that of the PVP composite.

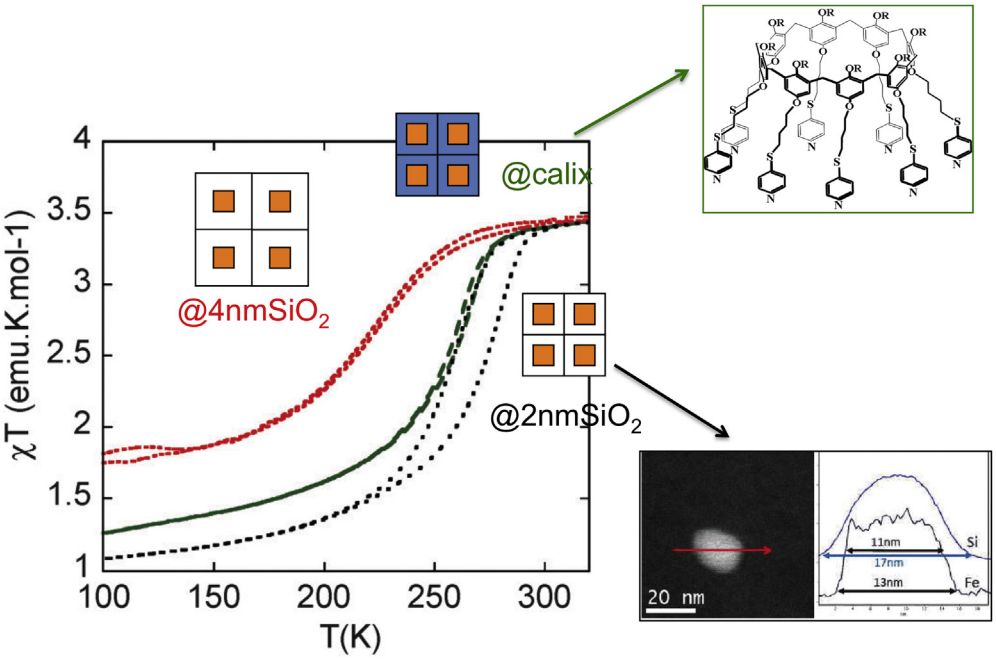

Fig. 20. Thermal evolution of χT for [Fe(pz){Pt(CN)$_4$}] nanoplatelets surrounded by a calixarene (green curve) and silica of variable thickness (2 nm, black curve; 4 nm, red curve). STEM-EELS profile of the composition obtained across a particle surrounded by 2 nm of silica.

This clearly stresses the importance of the crystallinity/texture of the matrix that delays the SCO phenomenon by exerting a negative pressure that depends on the viscoelastic properties of the matrix. An elegant demonstration to further support the importance of the viscoelasticity of the environment was made using matrices that soften (from glassy to viscous) while undergoing the SCO transition. [Fe(phen)$_2$(NCS)$_2$] microcrystals embedded in glycerol show a large hysteresis, not present on the bulk compound (Fig. 21e). Indeed, when going from the HS to the LS state, the viscous matrix becomes glassy and exerts an increasing negative pressure that delays the SCO and shifts the descending branch to lower temperatures [112,134]. The volume of the LS particles is then smaller than the original cavity, and particles are ultimately free from the interaction (Fig. 21a–c). This explains why the ascending curve is very similar to that of the bulk compound. This cooperativity may thus be considered as "matrix-induced".

Another experimental demonstration of the crucial role of the matrix is the use of polysaccharides (chitosan and alginate) as hard templates to confine the growth of sub-4 nm [Fe(pz){M(CN)$_4$}] particles [135]. Within chitosan, a thermal hysteresis loop is observed on the beads containing 4 nm [Fe(pz){Ni(CN)$_4$}] NPs. The Hofmann-like clathrate NPs located in the chitosan pores are covalently linked to the amino groups of the chitosan and could also be involved in the hydrogen bonding network via the remaining solvent molecules. The presence of such connectivity can induce a strong cooperativity between the NPs, which can explain the maintaining of the abrupt and cooperative transition for such ultrasmall NPs. One may also speculate, considering the high concentration of the NPs in the nanocomposite beads, that the change in one NP volume upon the spin transition may cooperatively spread in the whole SCO system through the rigid dispersing medium. In fact, the mechanical parameters of the chitosan matrix seem to affect the embedded SCO NPs. To confirm this statement and to better understand the role of the matrix, similar syntheses were realized for the Pt and Pd derivatives and also using an alginate polymer as matrix [135]. Alginates also belong to a family of polysaccharide biopolymers, but are mainly extracted from brown algae and incorporate carboxylate groups [136]. Although, the morphology of the beads of both polysaccharides is similar, they present different physicomechanical characteristics such as elasticity, hardness, thermal expansion, and so forth. In all cases, the synthetic modifications (different matrix or dissolution of the chitosan matrix) led to the disappearance of the abrupt hysteretic behavior obtained for the original chitosan matrix—despite the fact that the size of the particles remained very similar in each case. This finding confirms the key role played by the nature and the texture of the matrix on the cooperativity effect associated with the spin transition. Another interpretation is that the NPs feel a less important negative pressure when embedded in the beads that have larger cavities than in the film where reorganization of the chitosan chains at the interface of the particle may inhibit the volume change associated with the SCO. The second important point to note is the different magnetic behavior of the [Fe(pz){M(CN)$_4$}]–chitosan bead nanocomposites in the series with M = Ni, Pd, and Pt. Although, the presence of the spin transition was observed for the three nanocomposites, in comparison with the properties of the Ni derivative nanocomposite, the Pd derivative nanocomposite showed a less

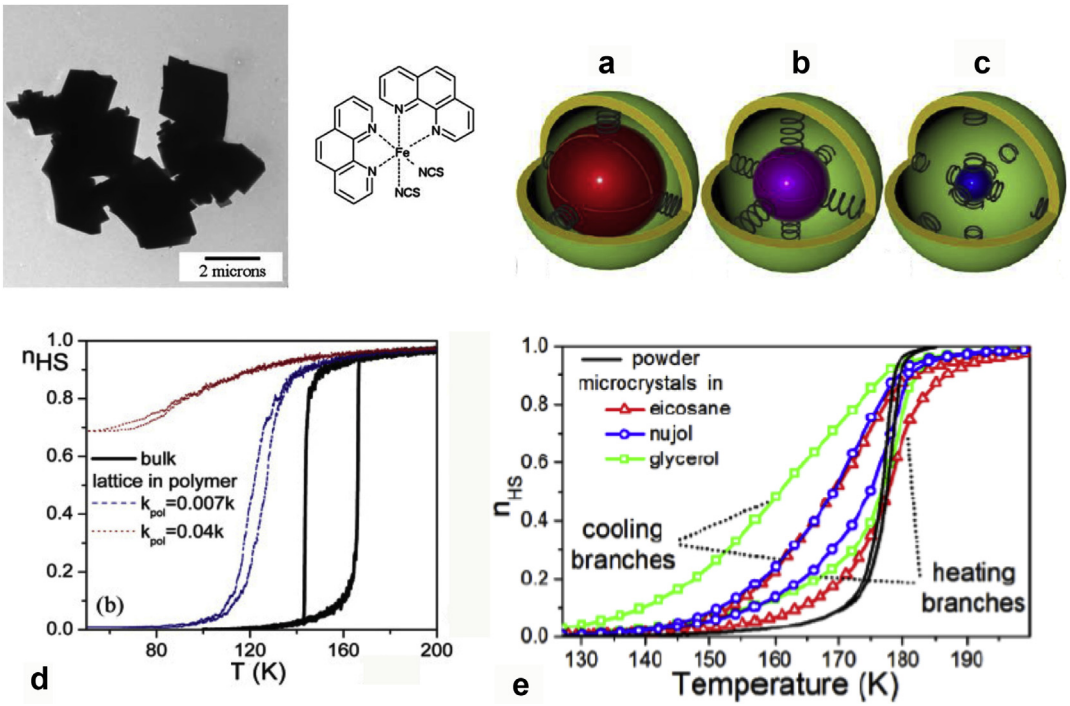

Fig. 21. Schematic model of interaction between matrix and particle with (a) HS particle, (b) during transition to LS with negative pressure exerted by the matrix, and (c) disruption of the interaction and "freed" particle. (d) Mechanoelastic model with k_{pol} representing the interaction of the polymer with the particle (weak interaction, blue curve; strong interaction, red curve). (e) Experimental data obtained on microcrystals of $[Fe(phen)_2(NCS)_2]$ embedded in eicosane (red), nujol (blue), and glycerol (green). Adapted from Refs. [112,133,134].

important fraction of iron centers involved in the abrupt hysteretic transition and an additional fraction involved in a consecutive gradual conversion, whereas the Pt derivative nanocomposite exhibited only a smooth and very incomplete spin conversion. Such difference may be explained by the increasing presence of structural defects of the cyanide-bridged structure associated with the decreasing basicity of the nitrogen atoms in the $[M(CN)_4]^{2-}$ building block in the series Ni > Pd > Pt and the concomitant decrease in the reactivity.

One important study performed by Mikolasek et al. [122] is the use of NIS to probe the viscoelastic properties of various sub-5 nm $[Fe(pz)\{M(CN)_4\}]$ NPs embedded in chitosan or AOT. This technique provides information on the vibrational density of state (of Fe), from which the lattice stiffness and vibrational entropy may be extracted. The Debye sound velocity that is associated with the elastic energy change during the SCO transition may be estimated from these NIS measurements and provides direct information on the cooperativity of the SCO phenomena. Besides confirming the expected larger stiffness in the LS state than in the HS state, these measurements revealed a larger stiffness when decreasing size less than 5 nm as an additional vibrational mode was observed in the low energy region for the chitosan matrix only. Moreover, the matrix plays an important role, as this additional feature is almost not observed with the AOT composite. This was interpreted as a possible sign of the free vibration of the whole particle in the less dense and strained environment of chitosan than with AOT, where a damping of the elastic waves may arise in a softer, viscous environment. Importantly, although at high temperature similar Debye sound velocities were observed in both matrices, the sound velocity showed a strong decrease for the chitosan matrix only, meaning that a strong stiffness variation occurs in this matrix when undergoing the SCO, which can be related to the stronger cooperativity observed for this sample.

Other examples of large influence of silica matrices on SCO particles were reported by several groups. Direct synthesis of $[Fe(Htrz)_2(trz)](BF_4)$ 3–5 nm particles in mesoporous silica templates exhibit larger hysteresis loops than the reference compound [30] (Fig. 22). In the case reported by Faulman et al. [27], the presence of Fe^{III} sites detected by Mössbauer explains the low proportion of Fe^{II} sites that undergo SCO. In both cases, the transition is partial and not fully reversible. Moreover, the growth of a thick silica shell on larger $[Fe(Htrz)_2(trz)](BF_4)$ rods by Herrera et al. [137] shows also such a widening of the hysteresis loop, with cyclability. In this case as contrary to NPs of the $[Fe(pz)\{M(CN)_4\}]$ family, one has to underline that particles are prepared in the LS state, so that when increasing the temperature, the particle feels a positive pressure due to the presence of the template. This is expected to lead to a slightly higher transition temperature for the ascending branch LS to HS, and may in some cases lead to damage in the nanomaterial's crystallinity because of the strain exerted by the matrix, reducing the cyclability.

The confinement of the same compound in ordered mesoporous silica MCM-41 reported by Zhao et al. [89] has also evidenced important changes in the hysteresis width

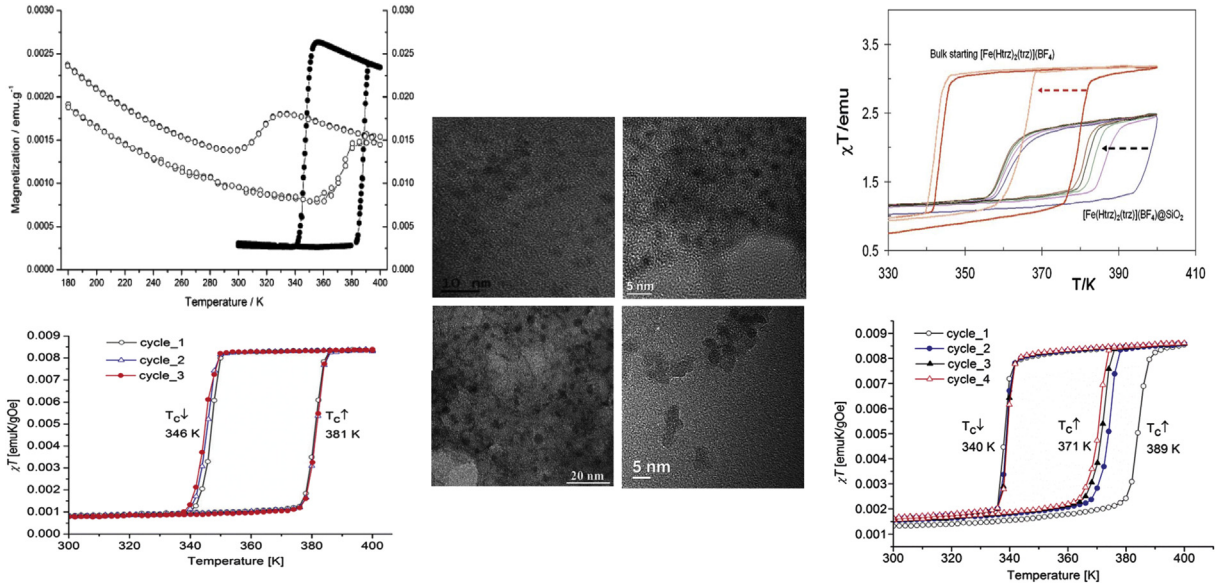

Fig. 22. TEM micrographs of 3–5 nm particles of $[Fe(Htrz)_2(trz)](BF_4)$ prepared in silica matrices and the differences in $\chi T = f(T)$ plots with different cycles: (a) in silica from Ref. [30]; (b) from Ref. [27]; (c, d) from Ref. [89] depending on the solvent used during the synthesis.

depending on the water content and solvent used in the synthesis (MeOH vs EtOH). Importantly, water was proposed to promote positive pressure, without any phase transition (contrary to the bulk sample). This set of results shows that not only the size of the particles and matrix nature may influence, as they are very similar, but also that minute changes in interaction between the matrix and the particle have considerable effects on the cooperativity, which may be related to H-bonding between silica and particle surface. In any case, this shows that sub-5 nm particles embedded in silica may retain a large cooperative character. Other composites embedding iron triazole SCO particles revealed such a modification in the cooperativity as in polypyrrole [138] and SU-8 [139].

These examples illustrate the special attention that has to be paid when using particles that are interacting with any kind of stabilizer, polymer, or matrix, especially when dealing with nanoscale materials. It appears of utmost importance to provide for more examples of matrix effects on nanocrystals of the same compound, same size, and shape homogeneously dispersed (aggregates may not be considered as well coated by the matrix) to further rationalize and optimize these effects. The study by NIS of more nanocrystal samples produced by the same synthetic process with different environments should provide crucial information on the role played by the interface nature and mechanical properties of the matrix on the cooperativity and phase stability. All of these experimental and theoretical approaches provide to the chemist important guidelines to fine-tune the SCO cooperativity by engineering the particle and matrix interface.

3. SCO nanohybrid/nanocomposite materials

The elaboration of functionalized nanocomposite or nanohybrid materials with potential applications in the field of switchable materials has recently attracted great attention in particular by the construction of core–shell particles [140–142]. Remarkable examples appeared recently in the literature of sophisticated structures involving SCO materials associated with other active (magnetic, fluorescent, plasmonic, conducting, piezoelectric, etc.) counterparts are gathered in this section.

3.1. SCO/magnetic core–shells

Among the various synergies that may be targeted, SCO/CTIST may be combined with ferromagnetism in a synergistic manner. As already mentioned, some PBAs display electron transfers induced by light and/or temperature and accompanied by a spin change, as for $[ACo(FeCN)_6]_y$ and $[AMn(FeCN)_6]_y$ (A = alkali such as Rb^+ or Cs^+) PBAs [143,144], or SCO as in $[CsFe(CrCN)_6]_y$ [145] but they also exhibit a large variety of magnetic behaviors such as ferro/ferrimagnetic ordering with fairly high Curie temperatures in the $[AM(CrCN)_6]_y$ series with $M = Ni^{II}$, Co^{II}, Cr^{II}, V^{II}, and so forth [146,147]. Because of the weak variation in cell parameters between most PBAs, epitaxial/heteroepitaxial growth of the same/different PBA networks is achievable in one nanocrystal (typically less than 5% misfit). In 2009, Catala et al. [50] reported the synthesis of self-standing charged PBA particles and core–shells/heterostructures through homo- and heteroepitaxial growth on PBA charged seeds without any surfactant. This one-step synthesis enables to prepare heterostructures with controlled and predetermined thicknesses of several PBAs opening interesting new synergies. Composition profiles performed by STEM-EELS revealed the segregation of the different PBA components, with no intermixing (Fig. 23).

Using Cs^+ as the alkali enables a one-pot approach because it inserts easily in the network with a weak number of remaining vacancies in hexacyanometallate so that

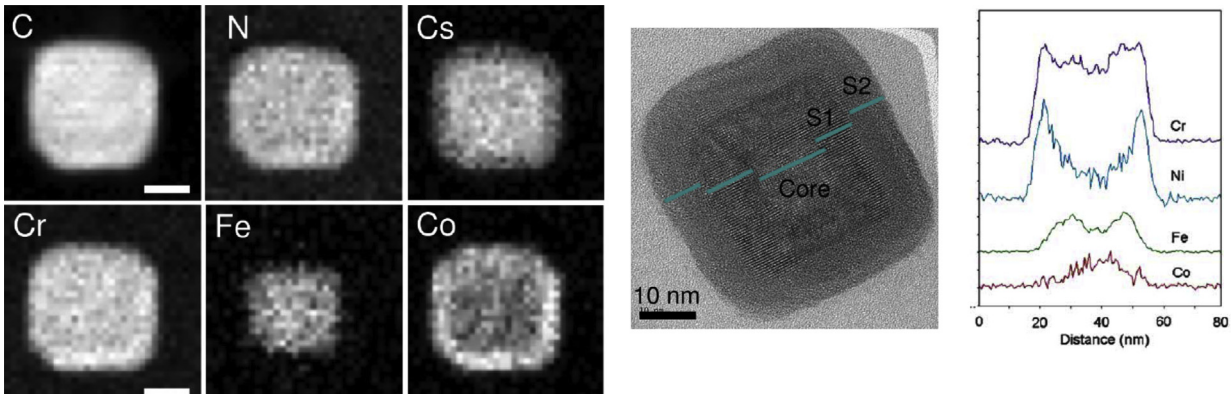

Fig. 23. (Left) Example of STEM-EELS mapping of CsFeCr@CoCr showing the core–shell architecture. (Right) Example of a high-resolution TEM micrograph of a CsCoCr@CsFeCr@CsNiCr heterostructure and the elemental profile across the particle. Adapted from Ref. [50].

the initial stoichiometry of precursors is obtained in the final nanostructures. When the core contains alkali other than Cs^+ and an excess of hexacyanometallate that is different between the core and the shell, the process may have to be adapted: intermediate stages are isolated and washed with hexacyanometallate solutions to circumvent any contamination at the interface [148]. Above a certain critical lattice misfit between the lattices in the core and shells (around 4–5%) the growth mode may change and formation of islands on the edges relaxes the strain as shown by Risset and Talham [149]. Heterostructures gathering a core that exhibits a CTIST (either photoinduced and/or thermoinduced) and ferromagnetic shells were studied in parallel by three different groups [150–152]. One example was given with 42 nm CsNiCr@$Co^{III}Fe^{II}$@CsNiCr particles (10 nm photoactive shell sandwiched between a 12 nm ferromagnetic core and 5 nm external ferromagnetic shell) obtained by Dia et al. [151] with a good crystallinity despite the significant misfit ($a_{core/shell2}$ = 10.40 Å, a_{shell} = 9.95 Å, and f = −4.5%). In this case, the photo-transformation based on light-induced CTIST ($Co^{III}Fe^{II}$ to $Co^{II}Fe^{III}$ switching) was observed probably because the external shell is 5 nm thick only and because the photo-conversion reduces the misfit at the interface when the $Co^{II}Fe^{III}$ pairs are formed. Because of the strain the photo-conversion remained partial and only paramagnetic state was achieved (when it was checked on a model that full $Co^{II}Fe^{III}$ would lead to ordering). A persistent increase in the magnetization up to 60 K corresponding to the ordering temperature of the ferromagnetic CsNiCr was observed due to the alignment of the photoinduced paramagnetic pairs by the magnetic field produced by the ferromagnetic CsNiCr shell (Fig. 24, left). In this case, the synergy is because of *magnetic dipolar* interactions between the core and the shells rather than the mechanical coupling.

Larger particles of formula $Rb_{0.5}Co^{III}Fe^{II}{}_{0.8}$@$Rb_{0.2}NiCr_{0.7}$ (45 nm core and 26 nm shell) were prepared by Presle et al. [152] with a similar misfit and a cube-on-cube growth mode. However, almost no phototransformation occurred probably because of the high coupling between the core and shell and the ratio between the core and shell thicknesses that impedes photoexpansion of the core and reduces the decay temperature of the photoexcited state (i.e., lower with Rb^+ than with Cs^+). A third and highly interesting example is provided by larger heterostructures (greater than 200 nm) of $Rb_{0.2}Co^{II}Fe^{III}$@RbMCr that were studied for M = Ni, Co, and Cr by Talham and co-workers. [150,153,154]. These core–shells have a much lower misfit parameter because a low Rb^+ content leads to the presence of Fe^{III}–CN–Co^{II} pairs at room temperature and to a cell parameter of the $Rb_{0.2}Co^{II}Fe^{III}$ core a = 10.30 Å (at 300 K) very close to that of the shell. $Rb_{0.2}Co^{II}Fe^{III}$ cubic cores of 160 nm were coated with a shell of KNiCr (a = 10.45 Å at 300 K) with variable thickness (15–95 nm) and revealed apparent crystallinity due to the low misfit (f = 0.9%). When irradiating these particles at low temperature, a persistent decrease in the magnetization was observed up to 90 K as in the layered films (Fig. 25, bottom right). Indeed, in this specific case, a thermal CTIST occurs when cooling down from 300 to 100 K with the core switching from HS $Rb_{0.2}Co^{II}Fe^{III}$ (a = 10.30 Å) to LS $Rb_{0.2}Co^{III}Fe^{II}$ (a = 9.96 Å) with a shrinking of the core volume. Powder XRD at variable temperature showed the contraction of the core [154]. A strained layer was proposed with a thickness of 24 nm for KCoCr and 43 nm for KNiCr above which a bulk behavior may be considered [155]. This emphasizes the importance of the volume ratios between the core and the shell to optimize these mechanical effects, both for the influence of the SCO core on the shell and the reverse case. The strain induced by this contraction of the core is released when irradiating at low temperature and leads to a realignment of the anisotropy axes causing a reduced magnetization according to the authors. This is a clear demonstration of mechanical coupling due to the change in volume provoked by the CTIST. Other heterostructures of RbCoFe@KCoCr exhibit similar features with more details provided on the influence of the thickness on the thermal CTIST [155].

Contrary to what may be expected, the CTIST is not dependent on the thickness, and for three thicknesses the core showed a complete CTIST at lower temperature whatever the thickness explored, with a gradual transition without hysteresis even for the thinnest 11 nm KCoCr shell (even if apparently more gradual for larger shells as the SCO transition is masked by the larger KCoCr signal, as seen in

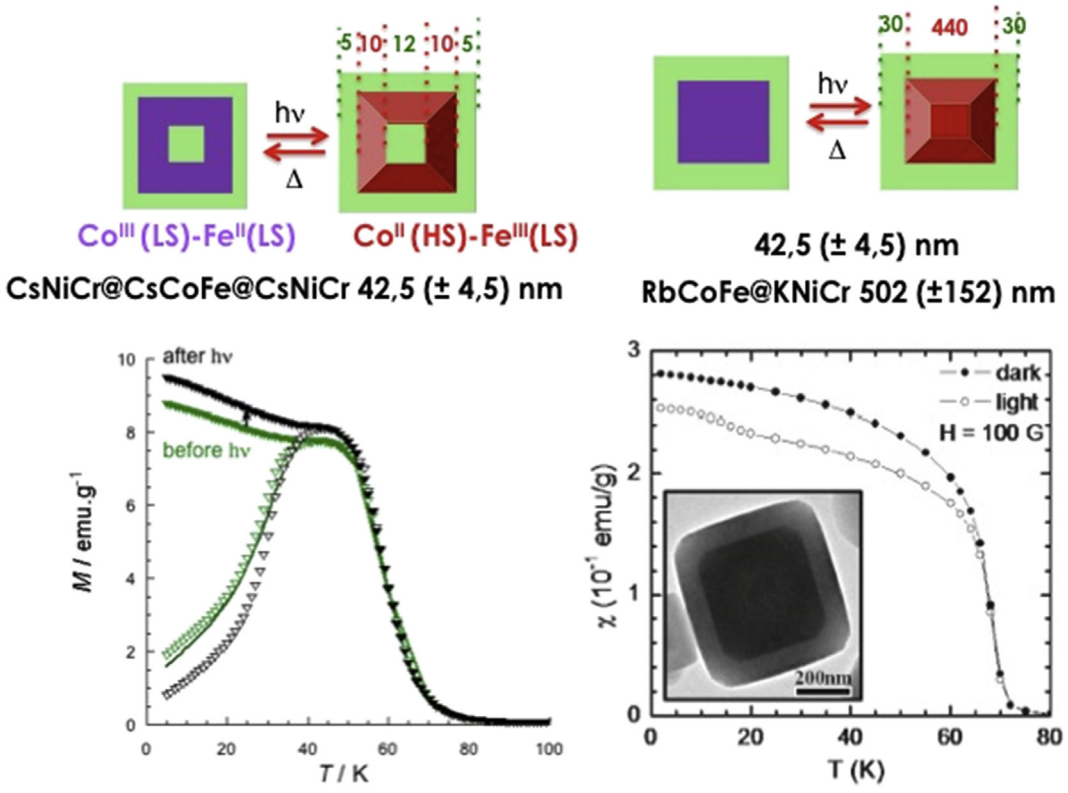

Fig. 24. Two examples of heterostructures gathering a photomagnetic and ferromagnetic PBA. (Left) Three shell particles of 42 nm size showing a persistent and reversible photoinduced increase in the magnetization up to the ordering temperature. (Right) Particles of 500 nm size showing persistent decrease in the magnetization under light (TEM micrograph as inset). Adapted from Refs. [150,151].

Fig. 25). The strong mechanical coupling hampers the internal elastic interactions. However, the most important point is that the SCO is maintained at slightly lower transition temperature (although without hysteresis) with a complete core contraction despite the strain exerted by the CsNiCr shell. This is probably because the shell has some defects and/or large core/shell thicknesses. These examples provide nice illustrations of synergies obtained by the elastic coupling of the core to a magnetic shell. Another example of combining photoactive to magnetic PBAs was reported using Hofmann clathrate nanoplatelets that display an LIESST effect, which were tentatively combined with a KNiCr shell [156]. However, only a weak effect on the magnetization was observed after irradiation at low temperature.

Apart from these PBA-based core–shells, an interesting example was provided on iron triazole–based core–shells that gather a $[Fe(NH_2trz)_3](BF_4)_2$ core and a $[Fe(Htrz)_2(trz)](BF_4)$ shell with the aim to couple different SCO behaviors [157]. Synthesis of the cores was performed in microemulsion using Triton X-100 as surfactant and hexanol as cosurfactant, leading to cylindrical particles of 450 nm in diameter and around 130 nm in height. The shell was obtained by alternative addition of aqueous solutions of $Fe(BF_4)_2$ and triazole in the microemulsions containing the cores. The growth of the shell was monitored by SEM as it takes 8 h to be complete, which revealed the assembly of rod-like crystallites that constitute the shell (Fig. 26). The length of the rods on the upper/bottom sides of the core is smaller than that of the rods growing on the sides of the core. The former are all oriented in the direction of the cylinder axis, whereas two directions of growth are seen for the latter. The authors invoke a shell of mixed composition with $[Fe(NH_2trz)_{3z}(Htrz)_{3-3z}](BF_4)_2$ rather than pure $[Fe(Htrz)_2(trz)](BF_4)$. The total SCO behavior reflects the presence of three SCO transitions (core, shell, and interface layer) on the ascending branch, whereas a rather gradual conversion around 285 K because of the $[Fe(NH_2trz)_{3z}(Htrz)_{3-3z}](BF_4)_2$ shell that has intermediate temperatures. It would be highly interesting to avoid this random distribution to have more abrupt SCO conversions.

These heterostructures are ideal systems with well-controlled interfaces and the back and forth between experiment and modeling is expected to guide the chemist to design new optimized combinations in the future.

3.2. SCO/fluorescent dyes

Various multifunctional materials combining luminescence and SCO properties have been reported mainly with the aim of achieving luminescence signal modulation resulting from the spin state switching phenomenon for an appropriate combination of the two components (see Ref. [158] and references herein). Thus a luminophore may be used to report upon the spin state of SCO nanomaterials because in many cases the detection of a luminescence

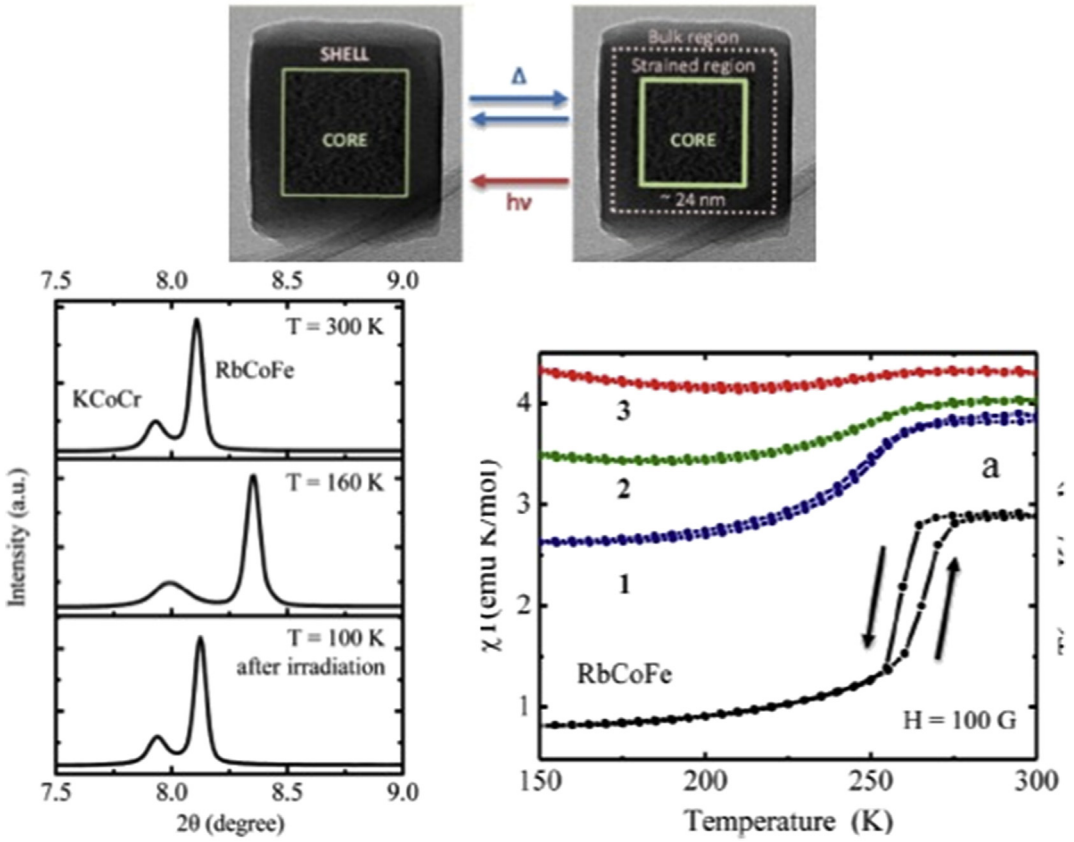

Fig. 25. RbCoFe@KCoCr heterostructures and scheme showing the presence of a strained region released by light. (Bottom left) XRD diagrams showing the contraction of the core and strained shell at 160 K and the released strain under light. (Bottom right) $\chi T = f(T)$ plots for heterostructures comprising a 137 ± 12 nm core and thicknesses of 11 nm (1), 23 nm (2), and 37 nm (3) showing SCO of the core at the same temperature. Adapted from Ref. [155].

signal is more efficient or easier to implement than other techniques commonly used in the SCO field. There is also a fundamental interest in studying energy transfer mechanisms between luminophores and transition metal complexes in the two spin states. Moreover, this asset can also be used advantageously in various photonic applications including photonic switches, thermometers, gas sensors, and so forth [7,159,160].

Salmon et al. [7] have developed a two-component system comprising ultrasmall SCO NPs and an appropriate luminophore. Synthesis of the composite NPs of $[Fe(NH_2trz)_3](tos)_2$ (tos = tosylate) was realized using the reverse micelle technique (surfactant is sodium bis(2-ethylhexyl) sulfosuccinate—NaAOT) in the presence of the rhodamine-110 (Rh110) molecule. Such fluorophore was selected because it exhibits only a very weak thermal extinction of the luminescence around room temperature, its emission spectrum overlaps the $^1A_1 \rightarrow {}^1T_1$ absorption band of the Fe^{II}-triazole complex and it exhibits a relatively weak photobleaching. The thermal variation in the fluorescence intensity at 540 nm, measured on a stable composite NP suspension shown in Fig. 27, indicated the maintaining of the bistability for such small (ca. 10 nm) NPs. A particular attention was paid on the effect of the rhodamine concentration on its emission intensity and variation upon SCO. Rhodamine 0.1% was determined as the ideal concentration to avoid the concentration-quenching of the luminescence, whereas a concentration of 0.001% was adapted to see the fluorescence modulation with the eyes (inset of Fig. 27). This doping strategy makes difficult the fine analysis of the composition of the resulting composite but it was supposed that the positively charged Rh110 molecules could interact with the negatively charged head groups of the surfactant molecules wrapping the NPs suggesting a radiative energy transfer mechanism, that is, the emitted radiation of the fluorophore is simply reabsorbed by the NPs in the LS state. Similar approach was used to combine various fluorophores with various Fe-triazole SCO NPs [7,94]. In particular the SCO properties of single 150 nm NPs of the $[Fe(hptrz)_3](tos)_2$ (where hptrz = 4-heptyl-1,2,4-triazole) derivative doped with acridine orange was probed by the fluorescence modulation of the fluorophore upon SCO [94]. The composite nano-object was elaborated via a soft lithography method. In this case, although again no precise structural information concerning the localization of the luminophore molecules in the network is possible, the mechanism responsible for quenching the luminescence can be attributed essentially to a nonradiative transfer between the acridine orange and the Fe^{II} ions present in

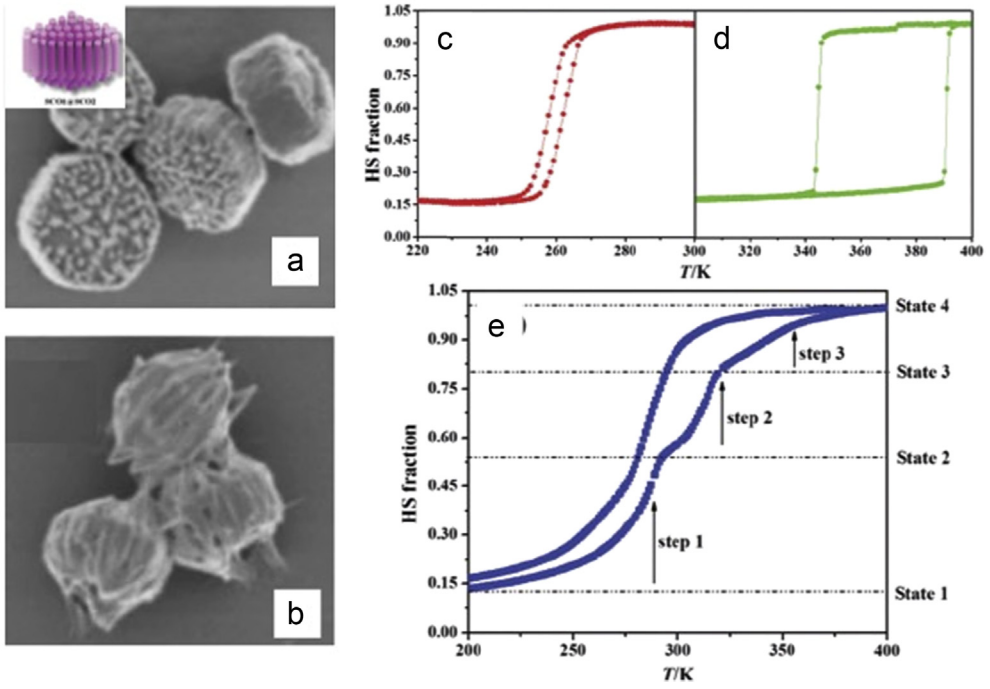

Fig. 26. SEM images of the SCO@SCO particles at early stage (a) and final stage (b). $\chi T = f(T)$ plots for the core alone (c), the shell alone (d), and the resulting core shells (e). Adapted from Ref. [157].

the complex. This hypothesis corroborates the increase in 50% of the signal during the transition and is in agreement with the negligible absorbance of such single SCO nano-objects. Moreover, in contrast to the positively charged rhodamine molecule that tends to be repulsed from the iron cations, the neutral and bearing a coordinating nitrogen atom acridine orange molecule could be in closed contact with the SCO iron chains.

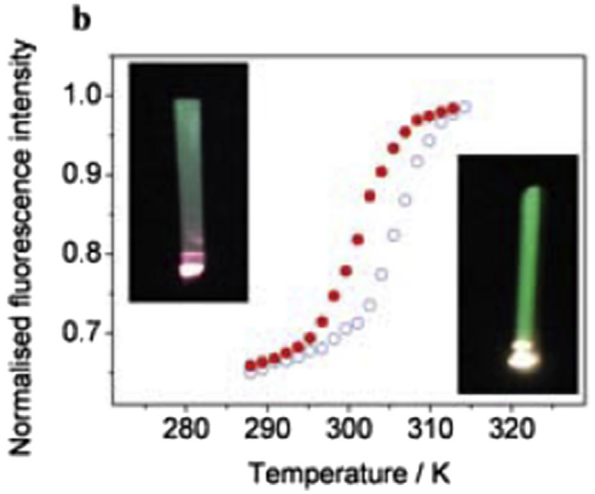

Fig. 27. Thermal variation in the emission intensity at 540 nm in the heating (open symbols) and cooling (closed symbols) modes for the Rh110 doped $[Fe(NH_2trz)_3](tos)_2$ (tos = tosylate) NP suspension. The insets show the photographs of the sample (0.001% Rh110) under white light excitation at 295 and 320 K. Adapted from Ref. [7].

A different approach to the combination of luminescence with nanoscale SCO materials was presented by Titos-Padilla et al. [90], in which a core (SCO)–shell (luminescence) NP architecture was used. This approach may also be considered as a form of doping luminophores into the SCO material, the essential distinction being that the location of the luminophore is known and confined to the surface of the hybrid particles. They reported a bifunctional nanocomposite system with the CP $[Fe(Htrz)_2(trz)](BF_4)$ (Htrz = 1,2,4-triazole and trz = 1,2,4-triazolato) as a core and a shell of silica. The use of silica is of great interest because of the possibility of grafting other functionalities on its surface. In this case, the luminophore 3-(dansylamido)-propyltrimethoxysilane was grafted on the surface of the NPs (see Fig. 28). Reverse micelle with Triton X-100 as a surfactant in the presence of the silica precursors was also used for the synthesis of the composite. The fluorescence data of the thus obtained rod-like NP with an average side length and width of 150 and 90 nm, respectively, and a shell of SiO_2 of ca. 12 nm revealed the maintaining of the SCO properties measured for the bulk compound. Metal dilution effects were also investigated by replacing a proportion of the iron centers with zinc. As expected, as the proportion of Zn^{II} ions doped into the SCO material increases, the transition is shifted to lower temperatures, becomes more gradual, and the hysteresis width narrows. The dansyl luminescence is quenched by the LS form of the Fe complex in the core of the particle via a supposed energy transfer mechanism, resulting from a degree of spectral overlap between the dansyl luminescence and the absorption band of the LS ion. More recently, the same authors studied the time-dependent

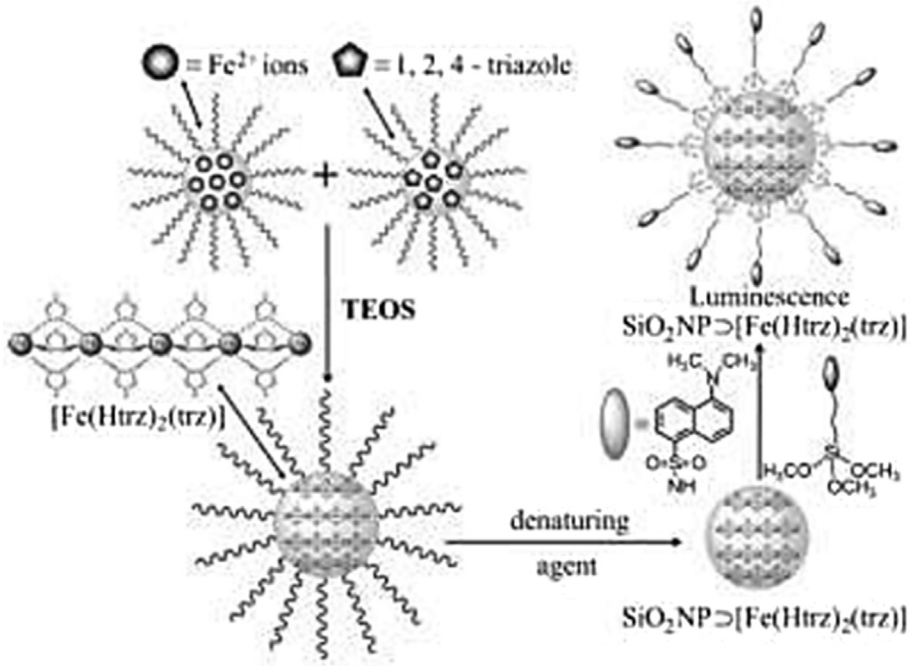

Fig. 28. Synthetic route and schematic representation of the SCO/dansyl SiO_2 NPs. Adapted from Ref. [90].

luminescence of these core–shell structures in comparison with similar particles without the active SCO core, which supported the existence of a dansyl-Fe^{II}(LS) nonradiative energy transfer with a rate of ca. 5.3×10^7 s^{-1} [137].

Inspired by this strategy, various kinds of fluorophores (quantum dots, lanthanide, and organic molecules) were grafted on the outer silica shell of the $[Fe(Htrz)_2(trz)](BF_4)$ @SiO_2 core–shell particles [161–163]. A terbium complex bearing a trimethoxysilane moiety was grafted on the silica shell. The Tb–SCO nanocomposite consists of elongated, aggregated NPs [161]. Their average length and width are 120 and 30 nm, respectively. The SCO and photophysical properties of this bistable luminescent composite have been fully characterized. This nanocomposite exhibits high resistance to photobleaching and remains stable over several consecutive thermal cycles. The terbium luminescence lifetime investigations at various temperatures (0.662 and 0.668 ms for the LS and HS state, respectively) have revealed no lifetime dependence on the spin state of the complex in agreement with a luminescence reabsorption energy transfer mechanism (see Fig. 29).

Triethoxysilane-functionalized pyrene molecule was also grafted on the SiO_2 particle surface. Platelet-like particles with a length (width) between ca. 60 and 150 nm (40 and 90 nm) were obtained by varying the cyclohexane quantity used in the microemulsion preparation [162]. Such fluorescent composite displayed both monomer and excimer luminescence centered around 430 and 605 nm, respectively. It was shown that the spin state switching influences, in a perfectly reversible manner, the intensity, the wavelength, and the excited state lifetime of pyrene excimer luminescence, whereas the monomer emission remains nearly unaffected. The spin state sensitivity of the excimer emission was attributed to pyrene–pyrene distances and orientation changes driven by the spontaneous strain accompanying the spin transition, even if

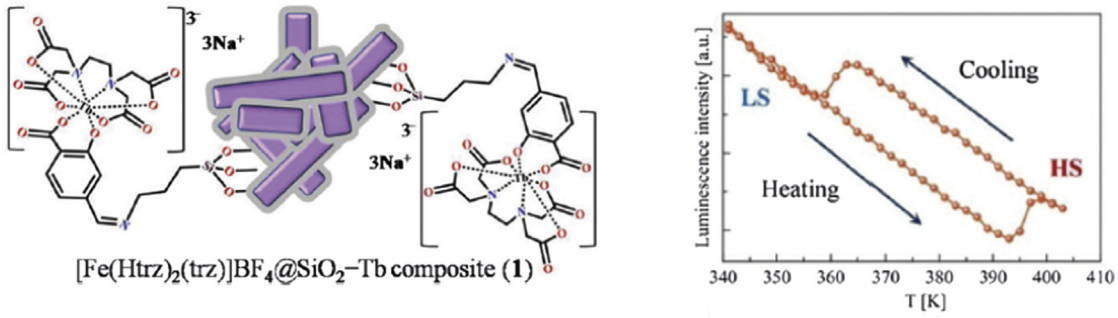

Fig. 29. Scheme and temperature-dependent luminescence intensity variation in the $[Fe(Htrz)_2(trz)](BF_4)$@SiO_2–Tb composite. Adapted from Ref. [161].

contributions from energy transfer processes could not be excluded. This new concept of hybrid luminescent SCO materials based on the spatial sensitivity of excimer luminescence provides a novel example for the quickly growing interest of using the mechanical strain of SCO materials in hybrid systems.

Nanocomposite materials containing cadmium telluride (CdTe) nanocrystals and $[Fe(Htrz)_2(trz)]BF_4$ NPs were also synthesized and investigated for the coupling between their photoluminescent and SCO properties [163]. In this case, the naked particles were covered by an intermediate branched polyethylenimine (BPEI) polymer to connect the 2 nm CdTe nanocrystals coated with COOH groups. Modifying the concentration of the reagents the shape of the $[Fe(Htrz)_2(trz)](BF_4)$ core was rather spherical with an average diameter of 40 nm in comparison with the rather rod shape obtained for all of the previous fluorescent composite materials. Upon heating, the luminescence of the nanocomposite sample exhibits a linear decrease, which corresponds to the usual thermal quenching phenomenon and upon thermal cycling the thermal hysteresis associated with the spin transition is clearly discernible. It is interesting to compare this behavior with analogous nanocomposite materials based on $[Fe(Htrz)_2(trz)](BF_4)$ @SiO_2 core–shell NPs and different luminophores. In each of these examples, the overall temperature dependence of the luminescence exhibits a very similar hysteresis, which compares well with that observed for magnetic measurements for the bulk sample. Indeed, although, matrix effect has been evidenced [137,163], the maintaining of the bistability is confirmed. Functionalization with the organic fluorophore 3-(dansylamido)propyltrimethoxysilane led to a marked luminescence intensity drop of ca. 80% when going from the HS to the LS state, which is attributed to a Förster-type energy transfer process. This change was reproducible on the reverse transition, but, for each thermal cycle, an irreversible decrease of ca. 20% in the luminescence occurred as well, which is explained by the thermal decomposition of the luminophore at high temperatures. Interestingly, the emission peak maximum shifted also from ca. 490 (LS) to 500 nm (HS) upon the SCO. Concerning the pyrene-grafted composite, when switching from the HS to the LS state the excimer luminescence intensity decreased by ca. 25–45% (depending on the luminophore quantity) and the emission spectra were red-shifted by ca. 15 nm. Photobleaching of the luminophore was also observed. A relatively small (ca. 2%), but very well reproducible decrease in the most intense transition centered at 545 nm accompanying the HS to LS transition was observed for the grafted Tb^{3+} complex on the $[Fe(Htrz)_2(trz)](BF_4)$@SiO_2 particles. Moreover, because this intensity modulation was not accompanied by any observable change in the luminescence lifetime, a radiative energy transfer mechanism via (partial) reabsorption of the emitted photons by the LS complexes was supposed. The relatively weak variation in the luminescence intensity accompanying the SCO in the CdTe composites (0.03%) suggests that probably a radiative energy transfer process occurs between the luminophore and the iron complex. So, it appears that by an appropriate choice of the spectral characteristics of the luminophore its emission will be inexorably modulated by the SCO phenomenon in this type of hybrid nanocomposites. The nature of the luminophore used and the way it is mixed with the SCO entities will determine "merely" the magnitude of the luminescence modulation. This allows one to change the luminescent properties of the composite material (e.g., the Tb^{3+} emission is characterized by sharp lines and long decays, whereas pyrene and CdTe exhibit broad emission bands and fast decays), while keeping virtually the same SCO properties.

One of the interesting perspectives of these works was the investigation of the relationship between the spectral overlap of the two entities and the luminescence modulation. Indeed, in each example reported above on luminescent SCO composites the luminescence signal was more intense in the HS state and up to now no "reverse switching" phenomenon (i.e., luminescence decrease in the HS state) was observed. With the aim to obtain such "reverse material" a cyanine dye (Cy7-NHS), emitting in the near infrared (800 nm) region was combined with the $[Fe(Htrz)_2(trz)](BF_4)$ SCO complex [164]. This latter display a broad HS absorption band in the near-infrared spectral range, wherein the LS phase is transparent, providing thus scope for reverse switching. The acid form of Cy7 activated with NHS (*N*-hydroxysuccinimide) was reacted with amine groups of BPEI forming the corresponding amide groups containing polymer Cy7-BPEI, which was combined with the $[Fe(Htrz)_2(trz)](BF_4)$ SCO NPs (see Fig. 30).

Contrary to that was expected, luminescence measurements revealed the strong increase (350–400%) in the emission intensity in the HS state. Because in this spectral region only the HS state absorbs light, this result cannot be interpreted by enhanced reabsorption or resonant energy transfer phenomena. The change in the properties of the crystal lattice (volume, stiffness, etc.) of the SCO NPs could explain this behavior. Further mechanistic studies will be necessary to clarify the origin of the interplay between these phenomena.

3.3. SCO/Nobel metal

The field of plasmonics represents an exciting new area for the application of surface and NP plasmons (i.e., collective oscillations of free electrons in metals) in nanotechnology. As a pioneering work in the field concerning SCO materials, Felix et al. [165] demonstrated that surface plasmon polariton waves propagating along the interface between a metal (gold) and a dielectric layer ($[Fe(hptrz)_3](OTs)_2$ complex with hptrz = 4-heptyl-1,2,4-triazole and OTs = tosylate) can be used to detect the spin state changes in the latter with high sensitivity. Following the surface plasmon resonance angle shift associated with the refractive index change, which occurs primarily because of the volume change accompanying the SCO, detection of nanometric thin films (30 nm) was achieved. Alternatively, using conventional electron beam lithography and liftoff, localized surface plasmons consisting of a series of arrays of gold nanorods with various geometries were also used to detect the SCO properties of similar layers [95]. Although such results should be applicable for most SCO compounds, another interesting perspective is the possibility to use SCO

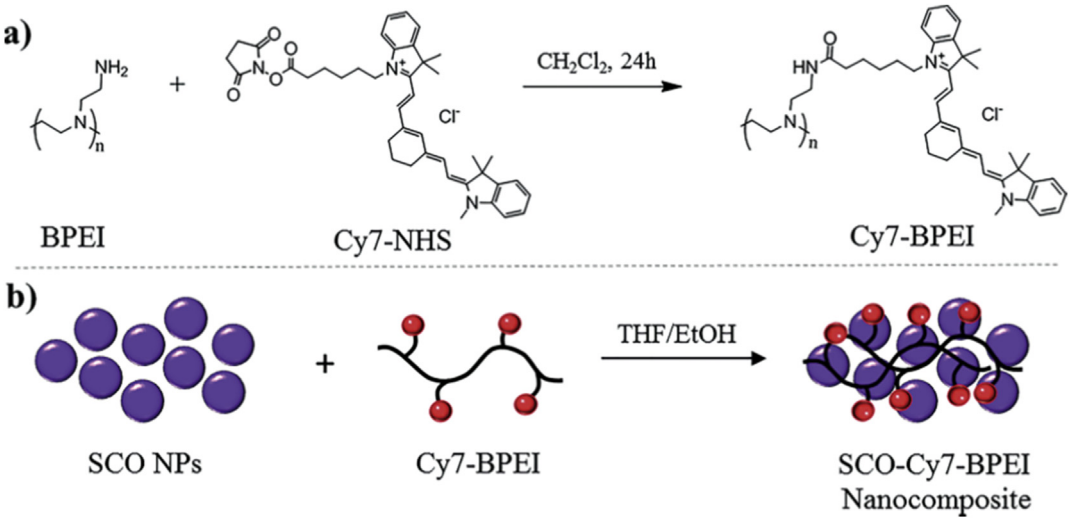

Fig. 30. Synthetic route for the preparation of the Cy7-BPEI polymer (a) and the SCO-Cy7-BPEI nanocomposite (b).

nanomaterials to modulate the propagation of electromagnetic waves in plasmonic or other type of guided wave devices.

Although extinction, absorption, and scattering are still the primary optical properties of interest, other spectroscopic techniques are also being brought to bear on these metallic nano-objects, including surface-enhanced Raman spectroscopy (SERS). SERS refers to the fact that chemical species deposited on specifically prepared metal surfaces exhibit very intense Raman spectra exceeding by several orders of magnitude what is observed on "normal" surfaces. Indeed, besides the detection of molecular spin state changes in thin films of SCO compounds, another critical issue is the analysis of their composition and structure. Several synthetic strategies have been used to elaborate the active SERS substrate. Comparison of the Raman spectrum of an SCO film deposited both inside and outside of the SERS active region of the arrays of gold nanorods used for the previous mentioned localized surface plasmon measurements did not reveal a clear enhancement for the SERS active region [140]. More elaborate architecture based on the layer-by-layer deposition of the [Fe(pz){Pt(CN)$_4$}] SCO CP was also used for the SERS enhancement. In particular, a specific SERS substrate was based on the introduction of gold NPs into a multilayer of the [Fe(pz){Pt(CN)$_4$}] film (5 nm) [140]. Although, the system allowed us to demonstrate the usefulness of the SERS approach for obtaining the spectral signature of very thin (5 nm) layers of SCO complexes, the temperature-dependent SERS spectra did not allow us to evidence clearly the thermal SCO. The extreme surface sensitivity of the method leads to the exaltation of the signal mainly from the first deposited layer, which is often not representative for the ensemble of the film because of the possible presence of impurities, anchoring layers (thiols in our case), or distorted/incomplete coordination environments around the Fe^{II} ions. Moreover, laser-induced heating in the regions of field enhancement may also arise. Other fabrication approaches concerning micro- and nanopattern covered with a rough gold film and layer-by-layer assembly on a substrate previously patterned with a gold NP array gave the same results [166].

SCO NPs were also combined with gold NPs. Forestier et al. [60] reported the coating of gold NPs on [Fe(NH$_2$trz)$_3$](Br) to highlight the presence of amino group on the surface of the SCO particles. A first way was to use the negative charge of carboxylated gold clusters to electrostatically interact with the protonated amino groups of SCO particles, whereas a second approach was based on the ligand exchange of weakly adsorbed polymer macromolecules on the gold surface by the amino groups of the SCO particles. The idea to use a composite SCO/gold nanostructure to obtain a plasmon-enhanced photothermal effect to reduce the energy needed to switch the SCO compound was reported by Suleimanov et al. [167]. In fact, SCO [Fe(Htrz)$_2$(trz)](BF$_4$) NPs were combined with gold NPs (2 nm) by means of an intermediate-decorated silica shell with the aim of using the ability of gold NPs to absorb light and convert it to heat. Using various power density laser excitation, a full LS to HS conversion was realized and a plasmonic enhancement of this photothermal spin state switching effect was evidenced. In fact, despite the volume fraction of gold within the nanocomposite being only 0.5%, the laser power required for the complete spin transition is reduced by ca. 70% in the presence of the gold NPs. Aiming to increase the size of the gold NPs attached to the SCO NPs, in situ additional reduction of aurum salt was performed leading to ca. 15 nm gold NPs (the formation of a complete gold shell was not possible). All attempts to get the Raman spectrum of the SCO@silica–larger gold NPs were unsuccessful. This could be explained by the SERS effect associated with the larger particles (see Fig. 31).

This in situ grafting of gold NP was also used by Qiu et al. [168] to elaborate identical nanocomposite SCO/gold objects showing the same photothermal effect. It is interesting to note here that a similar strategy for low-power laser switching was also developed using the strong infrared absorption of a polymer matrix in a polymer–SCO

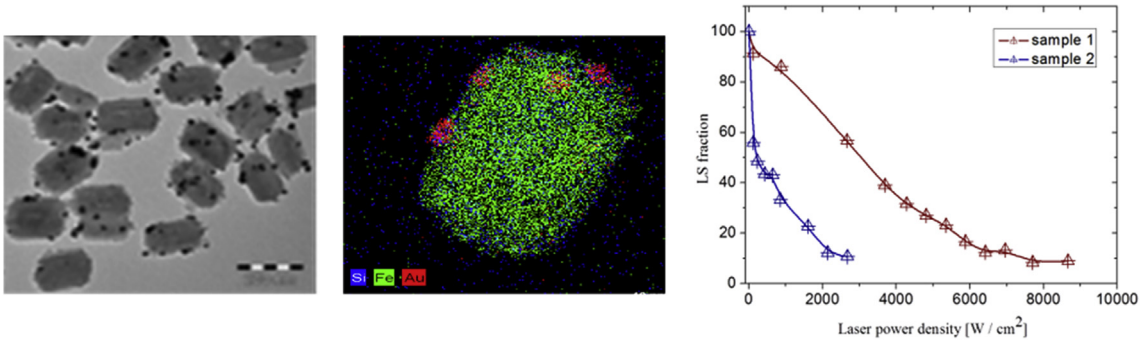

Fig. 31. Gold-decorated SCO–SiO_2 NPs and TEM/STEM-EDX images of the particles and laser power dependence of the converted fraction with (sample 2) and without (sample 1) gold NPs. Adapted from Ref. [167].

composite material [169]. Moulet et al. [170] reported the direct grafting (without intermediate silica shell) of various sized gold NPs, from 4 to 45 nm, on the surface of the $[Fe(Htrz)_2(trz)](BF_4)$ NPs by taking advantage of the likely affinity of the coordination ligand for Au. TEM revealed the control of the grafting and the good coverage of the gold NPs on the SCO particles (Fig. 32) but no photothermal effect was measured, certainly because of the insufficient power of the laser used.

Silver nanowires (AgNWs) decorated with $[Fe(Htrz)_2(trz)](BF_4)$ and [Fe(pz){Pt(CN)4}] NPs were also constructed by an in situ growing method [171]. It was shown that in such AgNWs@SCO nanocomposites, the electrical conductivity of the silver nanowires is not affected by the SCO NPs (see Fig. 33).

3.4. Miscellaneous SCO hybrids

Organic conducting polymers that can allow for conversion between mechanical and electrical forms of energy via the electromechanical effect have been combined with SCO particles [138,172]. In fact, under pressure, the distance between the conducting polymer chains decreases, reducing the energy barriers, and increasing the density of states at the Fermi level. So, the incorporation of an SCO material, which presents a change in volume during the spin transition, was supposed to change the internal pressure and consequently the conducting behavior. This approach was successfully used to modulate the conductivity of piezoresistive polypyrrole polymer, thanks to the incorporation of ca. 450 nm particles of the $[Fe(Htrz)_2(trz)](BF_4)$ complex [138]. The thermally induced change in volume of the SCO compound is accompanied by a variation in the conductivity of the polymer up to 300% (Fig. 34). SCO particles of formula $[Fe\{(Htrz)_2(trz)\}_{0.9}(NH_2\text{-}trz)_{0.3}](BF_4)_{1.1}$ have been homogeneously dispersed in P(VDF-TrFE) and PVDF matrices (Fig. 35) [172]. The composite materials display both discharge current and mechanical actuation peaks on cycling around the spin transition temperatures. Analysis of mechanical and dielectric properties reveals that both strain (1%) and permittivity (40%) changes in the composite accompany the spin transition in the particles, giving direct evidence for strong electromechanical couplings between the components. This new property, which arises from the synergy between the particles and the matrix, could be exploited for applications in electromechanical actuators and energy harvesting devices.

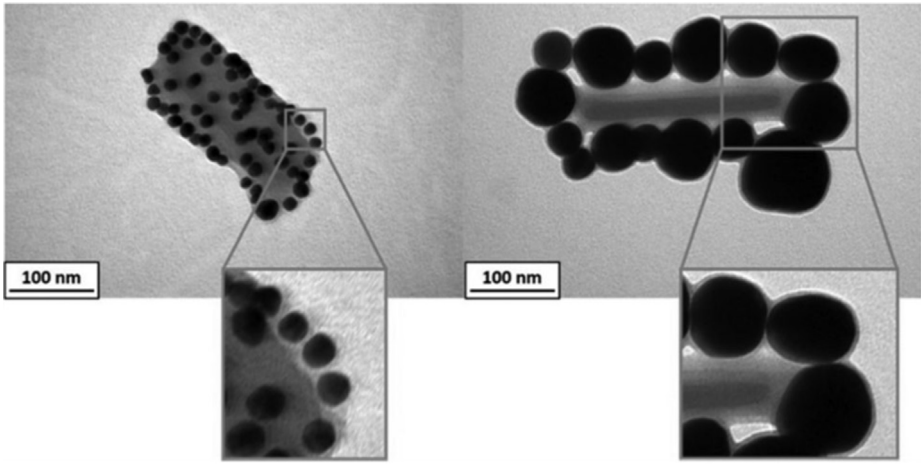

Fig. 32. TEM images of nanografted $[Fe(Htrz)_2(trz)](BF_4)$@Au particles for (right) 10 nm and (left) 45 nm gold particles. Adapted from Ref. [170].

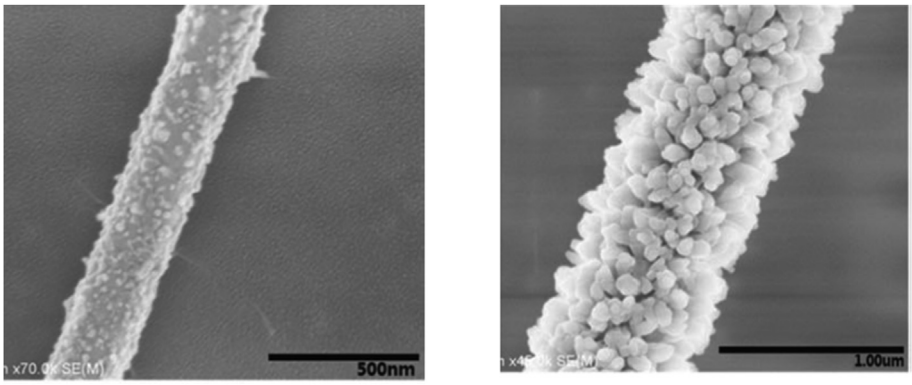

Fig. 33. SEM images of AgNWs@[Fe(Htrz)$_2$(trz)](BF$_4$) nanocomposite with increasing amounts of precursors (n(Fe^{II}) = 0.10 and 0.30 mmol). Adapted from Ref. [171].

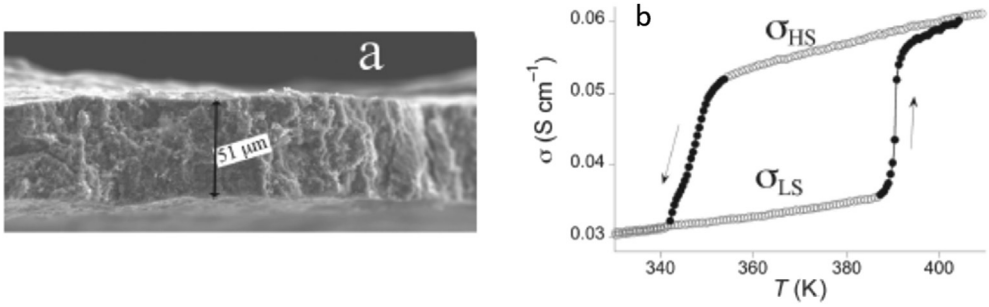

Fig. 34. Characterization of [Fe(Htrz)$_2$(trz)](BF$_4$)/ppy films: (a) TEM image of the film thickness; (b) thermal hysteresis in the conductivity data at 1 K min^{-1} scan rate, showing the two conducting regimes (empty circles) and the transition processes (full circles). Adapted from Ref. [138].

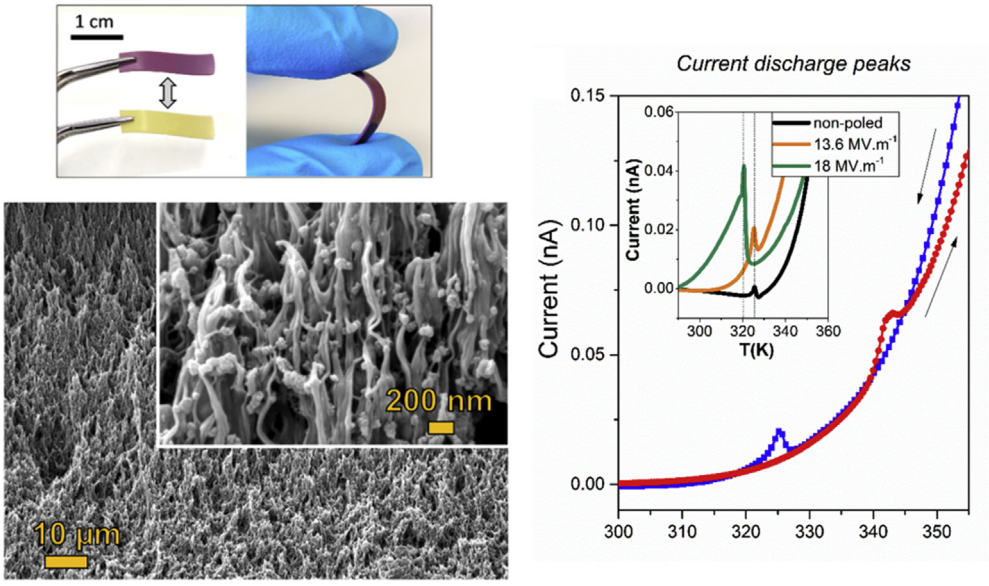

Fig. 35. Photographs of the flexible, freestanding SCO/P(VDF-TrFE) film in the LS (violet) and HS (yellow) states. Representative SEM micrographs of the composite cross-section. Short-circuit current under zero applied bias on heating and cooling at rates of ±2 K min^{-1}. Measurements were done after poling the sample in a 13.6 MV m^{-1} electrical field. The inset shows the modulation of the amplitude and temperature of the discharge current peak (cooling mode) controlled by the initial polarization. Adapted from Ref. [172].

Recent studies reported the coupling of graphene with SCO molecules [173–176] and SCO NPs [177–179]. Qiu et al. [177] prepared SCO–graphene nanocomposites by non-covalently anchoring NPs of the SCO CP $[Fe(Htrz)_2(trz)](BF_4)$ on graphene. The spherical NPs (50 nm) synthesized by a modified reverse microemulsion technique were simply deposited on the surface of graphene by sonication. They observed modifications of the temperature transition and width of the hysteresis loop because of the graphene surface interaction. More elaborated devices were obtained either by trapping in between single-layer graphene electrode $[Fe(Htrz)_2(trz)](BF_4)@SiO_2$ NPs using a dielectrophoresis method [178] or by deposition of a SCO $[Fe(Htrz)_2(trz)](BF_4)$ NP thin film by μ-contact printing on a chemical vapor deposition graphene layer on top of a silicon–silicon oxide substrate (Fig. 36) [179]. In the latter case, the SCO properties of the particles can be probed by measuring the variation in the conductivity of the graphene. In fact, the SCO is used via interface coupling to switch the carrier mobility of the graphene layer. It was proposed that this effect occurs because of the spin state dependence of charge carrier scattering at the interface, which is certainly related to the variation in the dielectric permittivity of the SCO layer.

SCO actuators have been elaborated by embedding the SCO material in various polymer matrices [6,180–182]. In particular, based on $[Fe(Htrz)_2(trz)](BF_4)$ NPs, macroscopic (centimeter scale) rectangular or six-petal flower bilayer actuator devices comprising a 50 μm thick freestanding polyester film on top of which was spray coated a 22 μm thick film of the $[Fe(Htrz)_2(trz)](BF_4)$/SU-8 composite were fabricated [183]. These soft actuators were then used to generate macroscale mechanical movements induced by the change in volume in the molecular complexes upon SCO. These soft actuators displayed large deflections and perceptible color changes upon the SCO (Fig. 37). The reversible opening of flowers upon temperature increase demonstrates the possibility to exploit such devices in the field of biomimetic artificial muscles whereas cantilevers were used to lift weight (Fig. 37B).

Interesting mechanical effects were also measured in composite materials made of cellulose fibers and SCO particles [9,184,185]. The linter cellulose fiber composite with 50 wt % loading of $[Fe(Htrz)_2(trz)](BF_4)$ particles was investigated by dynamic mechanical analysis. It was found that the storage modulus of the cellulose handsheet (0.6 GPa at room temperature) is significantly enhanced in the composite (1.7 GPa). The latter also displays a reversible increase in ca. 10% when switching the magnetic spin state of the particles from the LS to the HS form (Fig. 38). Around the spin transition temperature a peak in loss modulus is also observed, highlighting the strong viscoelastic coupling between the particles and the cellulose matrix. These results pave the way for the development of a novel family of actuator materials based on SCO–polymer composites.

4. Conclusions and perspectives

This contribution has provided an overview of the different synthetic pathways to produce SCO NPs, their inclusion in nanocomposites, the design of hybrid synergistic nanostructures and heterostructures, and their associated SCO behavior. Since the first examples reported a decade ago, a lot of knowledge has been gained on the fundamental understanding of the influence of downsizing SCO compounds at the nanoscale. The crucial role of the surface effects/stress and interface has been clearly evidenced, with an unexpected reopening of the thermal hysteresis below a critical size. The matrix has also shown to be key in the preservation/alteration of the hysteresis width; some matrix-induced hysteresis have been observed first unexpectedly and then by design, using specific viscoelastic properties of the matrices. Continuous back and forth between experiment and modelization have been pursued successfully, first with models post-rationalizing experiments and then anticipating new behaviors in prospective nanostructures. An important role is still played by chemists and physicochemists as more examples of well-defined nanosystems are needed to disentangle the roles of the surface, interface, viscoelastic

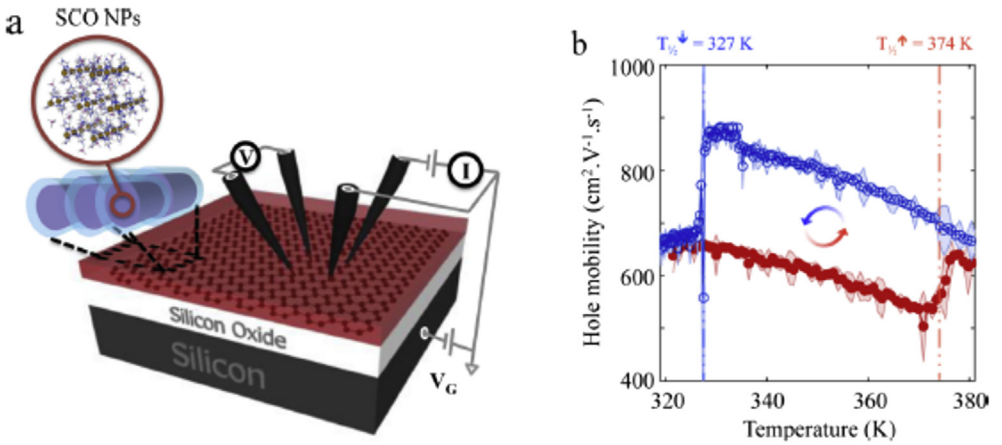

Fig. 36. a) Schematic of the device with chemical vapor deposition graphene on top of a silicon–silicon oxide substrate and after deposition of a $[Fe(Htrz)_2(trz)](BF_4)$ NP thin film prepared by μ-contact printing. The transport properties of graphene have been determined from the four-probe sample resistance in a van der Pauw configuration. (b) Hole mobility vs temperature for the heating and cooling modes. Adapted from Ref. [179].

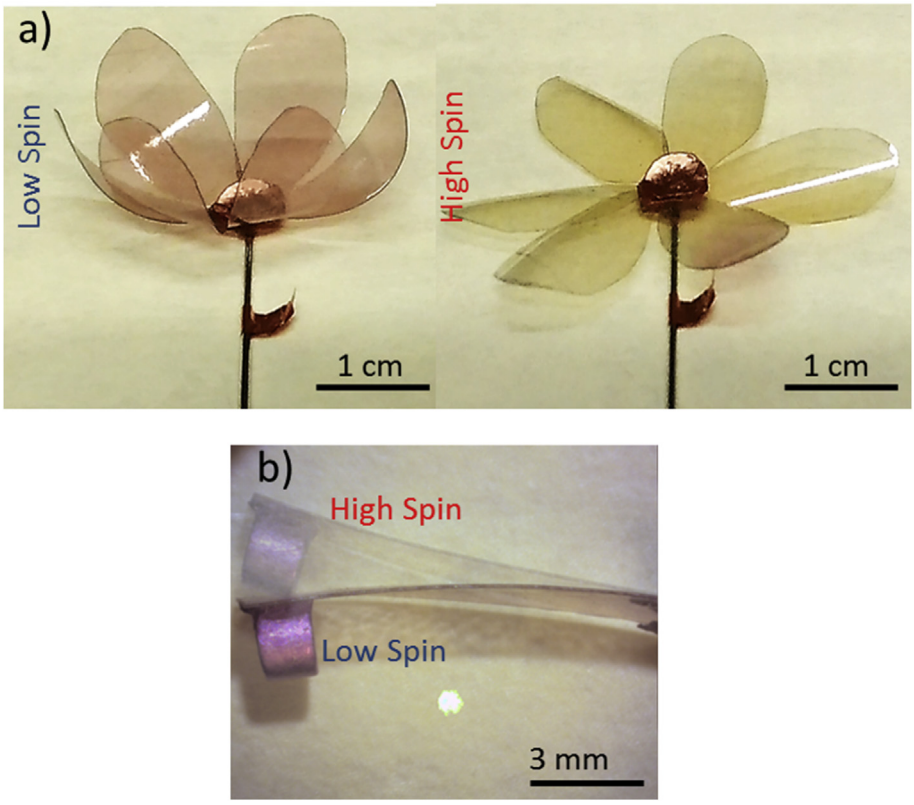

Fig. 37. a) Macroscopic flower opening and (b) cantilever bending with ca. 5 mg load. The cantilever dimensions are $w = 2$ mm, $t = 0.0\ 75$ mm, and $l = 11$ mm. Adapted from Ref. [183].

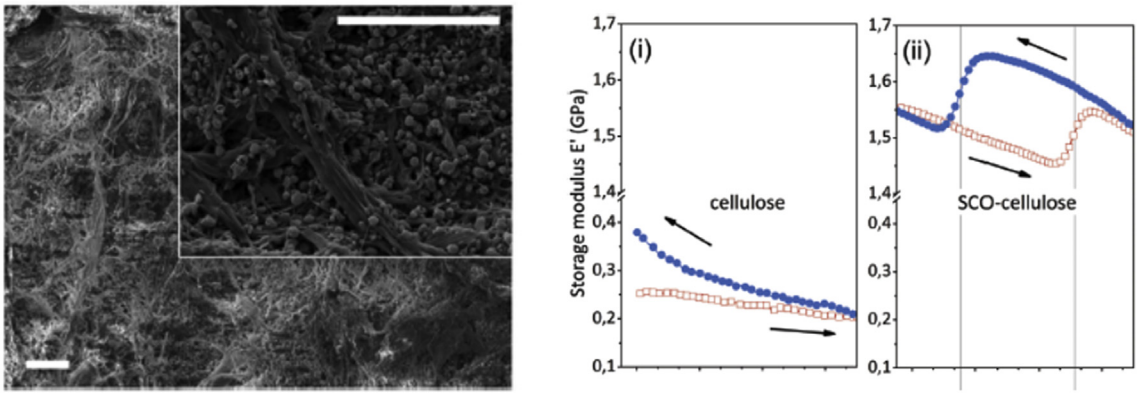

Fig. 38. SEM images of the $[Fe(Htrz)_2(trz)](BF_4)$/cellulose composite (the inset shows a zoomed image), scale bars are 10 mm. Storage modulus of the pure and composite cellulose sheets at different temperatures in the heating (red open symbols) and cooling (blue closed symbols) modes. Arrows indicate heating and cooling.

properties of the surrounding on the SCO cooperativity, and validate theoretical assumptions. Specific measurements such as NIS performed on reference nanocrystals with well-defined coatings are strongly required to give a complete description of the interplay between the SCO material and its surrounding. One major task to tackle is to fully control and analyze the interface nature in ultrasmall nanosystems (defects, types of bonds, etc.). Computational methods will be determinant to evaluate some surface/interface energies and guide the chemists to optimize nanostructures. Besides the microscopic and fundamental description, the processing of SCO nanocomposites in several displays has been already addressed and synergies have emerged between SCO and optical, magnetic, electric, and mechanical properties. The use of piezoelectric polymer is one promising approach, but no

doubt that many new outcomes will be produced in the forthcoming years and help to progress on the route toward technologically relevant SCO-based devices.

References

[1] O. Kahn, C.J. Martinez, Science 279 (1998) 44–48.
[2] C.-M. Jureschi, J. Linares, A. Boulmaali, P. Dahoo, A. Rotaru, Y. Garcia, Sensors 16 (2016) 187.
[3] K. Boukheddaden, M.H. Ritti, G. Bouchez, M. Sy, M.M. Dîrtu, M. Parlier, J. Linares, Y. Garcia, J. Phys. Chem. C 122 (2018) 7597–7604.
[4] Y. Guo, S. Xue, M.M. Dîrtu, Y. Garcia, J. Mater. Chem. C 6 (2018) 3895–3900.
[5] C. Bartual-Murgui, A. Akou, C. Thibault, G. Molnár, C. Vieu, L. Salmon, J. Mater. Chem. C 3 (2015) 1277–1285.
[6] H.J. Shepherd, I.A. Gural'skiy, C.M. Quintero, S. Tricard, L. Salmon, G. Molnár, A. Bousseksou, Nat. Commun. 4 (2013).
[7] L. Salmon, G. Molnár, D. Zitouni, C. Quintero, C. Bergaud, J.-C. Micheau, A. Bousseksou, J. Mater. Chem. C 20 (2010) 5499.
[8] J.-F. Létard, P. Guionneau, L. Goux-Capes, in: Spin Crossover in Transition Metal Compounds III, Springer-Verlag, Berlin/Heidelberg, 2004, pp. 221–249.
[9] V. Nagy, I. Suleimanov, G. Molnár, L. Salmon, A. Bousseksou, L. Csóka, J. Mater. Chem. C 3 (2015) 7897–7905.
[10] L. Salmon, A. Bousseksou, B. Donnadieu, J.-P. Tuchagues, Inorg. Chem. 44 (2005) 1763–1773.
[11] A. Bousseksou, F. Varret, M. Goiran, K. Boukheddaden, J.P. Tuchagues, in: Spin Crossover in Transition Metal Compounds III, Springer-Verlag, Berlin/Heidelberg, 2004, pp. 65–84.
[12] A. Hauser, in: Spin Crossover in Transition Metal Compounds II, Springer, Berlin, Heidelberg, 2004, pp. 155–198.
[13] V. Ksenofontov, A.B. Gaspar, P. Gütlich, in: Spin Crossover in Transition Metal Compounds III, Springer-Verlag, Berlin/Heidelberg, 2004, pp. 23–64.
[14] S. Cobo, D. Ostrovskii, S. Bonhommeau, L. Vendier, G. Molnár, L. Salmon, K. Tanaka, A. Bousseksou, J. Am. Chem. Soc. 130 (2008) 9019–9024.
[15] A. Bousseksou, G. Molnár, L. Salmon, W. Nicolazzi, Chem. Soc. Rev. 40 (2011) 3313.
[16] H.J. Shepherd, G. Molnár, W. Nicolazzi, L. Salmon, A. Bousseksou, Eur. J. Inorg. Chem. 2013 (2013) 653–661.
[17] M. Cavallini, Phys. Chem. Chem. Phys. 14 (2012) 11867.
[18] C.R. Mario Ruben, in: M. Halcrow (Ed.), Spin-crossover Materials: Properties and Applications, 2013, pp. 375–404.
[19] G. Molnár, L. Salmon, W. Nicolazzi, F. Terki, A. Bousseksou, J. Mater. Chem. C 2 (2014) 1360–1366, https://doi.org/10.1039/C3TC31750A.
[20] M. Imperor-Clerc, D. Bazin, M.D. Appay, P. Beaunier, A. Davidson, Chem. Mater. 16 (2004) 1813–1821.
[21] L. Catala, T. Mallah, Coord. Chem. Rev. 346 (2017) 32–61.
[22] O. Sato, T. Iyoda, A. Fujishima, K. Hashimoto, Science 272 (1996) 704–705.
[23] G. Champion, V. Escax, C.C.D. Moulin, A. Bleuzen, F.O. Villain, F. Baudelet, E. Dartyge, N. Verdaguer, J. Am. Chem. Soc. 123 (2001) 12544–12546.
[24] S. Ohkoshi, H. Tokoro, Acc. Chem. Res. 45 (2012) 1749–1758.
[25] J.G. Moore, E.J. Lochner, C. Ramsey, N.S. Dalal, A.E. Stiegman, Angew. Chem., Int. Ed. 42 (2003) 2741–2743.
[26] G. Fornasieri, A. Bleuzen, Angew. Chem. Int. Ed. 47 (2008) 7750–7752.
[27] C. Faulmann, J. Chahine, I. Malfant, D. de Caro, B. Cormary, L. Valade, Dalton Trans. 40 (2011) 2480.
[28] A. Tissot, J.-F. Bardeau, E. Rivière, F. Brisset, M.-L. Boillot, Dalton Trans. 39 (2010) 7806.
[29] G. Fornasieri, M. Aouadi, P. Durand, P. Beaunier, E. Riviere, A. Bleuzen, Chem. Commun. 46 (2010) 8061–8063.
[30] P. Durand, S. Pillet, E.-E. Bendeif, C. Carteret, M. Bouazaoui, H. El Hamzaoui, B. Capoen, L. Salmon, S. Hébert, J. Ghanbaja, L. Aranda, D. Schaniel, J. Mater. Chem. C. 1 (2013) 1933.
[31] T. Zhao, I. Boldog, V. Spasojevic, A. Rotaru, Y. Garcia, C. Janiak, J. Mater. Chem C. 4 (2016).
[32] R. Moulin, E. Delahaye, A. Bordage, E. Fonda, J.P. Baltaze, P. Beaunier, E. Riviere, G. Fornasieri, A. Bleuzen, Eur. J. Inorg. Chem. (2017) 1303–1313.
[33] P.H. Zhou, D.S. Xue, H.Q. Luo, J.L. Yao, H.G. Shi, Nanotechnology 15 (2004) 27–31.
[34] Y.M. Shi, B. Zhou, P. Wu, K.Y. Wang, C.X. Cai, J. Electroanal. Chem. 611 (2007) 1–9.
[35] P.N. Martinho, T. Lemma, B. Gildea, G. Picardi, H. Müller-Bunz, R.J. Forster, T.E. Keyes, G. Redmond, G.G. Morgan, Angew. Chem. Int. Ed. 51 (2012) 11995–11999.
[36] Y.-X. Wang, D. Qiu, Z.-H. Li, Z.-G. Gu, X. Ren, Z. Li, Eur. J. Inorg. Chem. 28 (2016) 4581–4585.
[37] M.P. Pileni, Adv. Colloid. Interface Sci 46 (1993) 139–163.
[38] S. Vaucher, M. Li, S. Mann, Angew. Chem. Int. Ed. 32 (2000) 1793.
[39] F.J. Valverde-Muñoz, A.B. Gaspar, S.I. Shylin, V. Ksenofontov, J.A. Real, Inorg. Chem. 54 (2015) 7906–7914.
[40] E. Coronado, J.R. Galán-Mascarós, M. Monrabal-Capilla, J. García-Martínez, P. Pardo-Ibáñez, Adv. Mater. 19 (2007) 1359–1361.
[41] Y. Raza, F. Volatron, S. Moldovan, O. Ersen, V. Huc, C. Martini, F. Brisset, A. Gloter, O. Stéphan, A. Bousseksou, L. Catala, T. Mallah, Chem. Commun. 47 (2011) 11501–11503.
[42] S. Forster, M. Antonietti, Adv. Mater. 10 (1998) 195.
[43] O. Klimm, C. Göbel, S. Rosenfeldt, F. Puchtler, N. Miyajima, K. Marquardt, M. Drechsler, J. Breu, S. Förster, B. Weber, Nanoscale 8 (2016) 19058–19065.
[44] F. Volatron, Paris Sud 11 (2011).
[45] V. Martinez, I. Boldog, A.B. Gaspar, V. Ksenofontov, A. Bhattacharjee, P. Gutlich, J.A. Real, Chem. Mater. 22 (2010) 4271–4281.
[46] I.A. Gural'skiy, C.M. Quintero, G. Molnár, I.O. Fritsky, L. Salmon, A. Bousseksou, Chem. Eur J. 18 (2012) 9946–9954.
[47] V.K. Lamer, R.H. Dinegar, J. Am. Chem. Soc. 72 (1950) 4847–4854.
[48] M. Oh, C.A. Mirkin, Nature 438 (2005) 651–654.
[49] I. Imaz, D. Maspoch, C. Rodriguez-Blanco, J.M. Perez-Falcon, J. Campo, D. Ruiz-Molina, Angew. Chem. Int. Ed. 47 (2008) 1857–1860.
[50] L. Catala, D. Brinzei, Y. Prado, A. Gloter, O. Stephan, G. Rogez, T. Mallah, Angew. Chem. Int. Ed. 48 (2009) 183–187.
[51] K. Robertson, P.B. Flandrin, H.J. Shepherd, C.C. Wilson, Chim. Oggi-Chem. Today 35 (2017) 19.
[52] N. Daro, L. Moulet, N. Penin, N. Paradis, J.-F. Létard, E. Lebraud, S. Buffière, G. Chastanet, P. Guionneau, Materials 10 (2017) 60.
[53] O. Roubeau, Chem. Eur J. 18 (2012) 15230–15244.
[54] L.G. Lavrenova, O.G. Shakirova, Eur. J. Inorg. Chem. 2013 (2013) 670–682.
[55] A. Grosjean, N. Daro, B. Kauffmann, A. Kaiba, J.-F. Létard, P. Guionneau, Chem. Commun. 47 (2011) 12382.
[56] A. Grosjean, P. Négrier, P. Bordet, C. Etrillard, D. Mondieig, S. Pechev, E. Lebraud, J.-F. Létard, P. Guionneau, Eur. J. Inorg. Chem. 2013 (2013) 796–802.
[57] J. Haasnoot, G. Vos, W.L. Groeneveld, Z. Naturforsch. B. 32 (1977) 1421–1430.
[58] M.M. Dîrtu, C. Neuhausen, A.D. Naik, A. Rotaru, L. Spinu, Y. Garcia, Inorg. Chem. 49 (2010) 5723–5736.
[59] J.-F. Létard, O. Nguyen, N. Daro. Patent FR2894581, 2007.
[60] T. Forestier, S. Mornet, N. Daro, T. Nishihara, S. Mouri, K. Tanaka, O. Fouché, E. Freysz, J.-F. Létard, Chem. Commun. (2008) 4327–4329.
[61] T. Forestier, Synthèse de nanoparticules à transition de spin en milieu confiné, Université de Bordeaux, 2008.
[62] M.-Y. Chen, X.-R. Chen, W.-H. Ning, X.-M. Ren, RSC Adv. 4 (2014) 39126–39131.
[63] A. Tokarev, L. Salmon, Y. Guari, W. Nicolazzi, G. Molnár, A. Bousseksou, Chem. Commun. 46 (2010) 8011.
[64] A. Tokarev, L. Salmon, Y. Guari, G. Molnár, A. Bousseksou, New J. Chem. 35 (2011) 2081.
[65] T. Forestier, A. Kaiba, S. Pechev, D. Denux, P. Guionneau, C. Etrillard, N. Daro, E. Freysz, J.-F. Létard, Chem. Eur J. 15 (2009) 6122–6130.
[66] A. Rotaru, F. Varret, A. Gindulescu, J. Linares, A. Stancu, J.F. Létard, T. Forestier, C. Etrillard, Eur. Phys. J. B 84 (2011) 439–449.
[67] C. Arnaud, T. Forestier, N. Daro, E. Freysz, J.-F. Létard, G. Pauliat, G. Roosen, Chem. Phys. Lett. 470 (2009) 131–135.
[68] J.R. Galán-Mascarós, E. Coronado, A. Forment-Aliaga, M. Monrabal-Capilla, E. Pinilla-Cienfuegos, M. Ceolin, Inorg. Chem. 49 (2010) 5706–5714.
[69] M. Giménez-Marqués, M.L. García-Sanz de Larrea, E. Coronado, J. Mater. Chem. C 3 (2015) 7946–7953.
[70] I. Suleimanov, J.S. Costab, G. Molnárb, L. Salmon, I.O. Fritsky, A. Bousseksou, French-Ukrainian J. Chem. 3 (2015) 66.
[71] C. Bartual-Murgui, E. Natividad, O. Roubeau, J. Mater. Chem. C 3 (2015) 7916–7924.
[72] L. Moulet, N. Daro, C. Etrillard, J.-F. Létard, A. Grosjean, P. Guionneau, Magnetochemistry 2 (2016) 10.

[73] A. Grosjean, N. Daro, S. Pechev, L. Moulet, C. Etrillard, G. Chastanet, P. Guionneau, Eur. J. Inorg. Chem. 2016 (2016) 1961–1966.
[74] A. Grosjean, N. Daro, S. Pechev, C. Etrillard, G. Chastanet, P. Guionneau, Eur. J. Inorg. Chem. 2018 (2018) 429–434.
[75] M. Manrique-Juárez, I. Suleimanov, E. Hernández, L. Salmon, G. Molnár, A. Bousseksou, Materials 9 (2016) 537.
[76] C. Lefter, R. Tan, S. Tricard, J. Dugay, G. Molnár, L. Salmon, J. Carrey, A. Rotaru, A. Bousseksou, Polyhedron 102 (2015) 434–440.
[77] D. Tanaka, N. Aketa, H. Tanaka, T. Tamaki, T. Inose, T. Akai, H. Toyama, O. Sakata, H. Tajiri, T. Ogawa, Chem. Commun. 50 (2014) 10074–10077.
[78] C. Thibault, G. Molnár, L. Salmon, A. Bousseksou, C. Vieu, Langmuir 26 (2010) 1557–1560.
[79] C. Lefter, V. Davesne, L. Salmon, G. Molnár, P. Demont, A. Rotaru, A. Bousseksou, Magnetochemistry 2 (2016) 18.
[80] A. Rotaru, I.A. Gural'skiy, G. Molnár, L. Salmon, P. Demont, A. Bousseksou, Chem. Commun. 48 (2012) 4163–4165.
[81] A. Rotaru, J. Dugay, R.P. Tan, I.A. Guralskiy, L. Salmon, P. Demont, J. Carrey, G. Molnár, M. Respaud, A. Bousseksou, Adv. Mater. 25 (2013) 1745–1749.
[82] J. Dugay, M. Giménez-Marqués, T. Kozlova, H.W. Zandbergen, E. Coronado, H.S.J. van der Zant, Adv. Mater. 27 (2015) 1288–1293.
[83] C. Lefter, S. Tricard, H. Peng, G. Molnár, L. Salmon, P. Demont, A. Rotaru, A. Bousseksou, J. Phys. Chem. C 119 (2015) 8522–8529.
[84] C. Etrillard, V. Faramarzi, J.-F. Dayen, J.-F. Letard, B. Doudin, Chem. Commun. 47 (2011) 9663–9665.
[85] C. Lefter, R. Tan, J. Dugay, S. Tricard, G. Molnár, L. Salmon, J. Carrey, A. Rotaru, A. Bousseksou, Phys. Chem. Chem. Phys. 17 (2015) 5151–5154.
[86] C. Lefter, R. Tan, J. Dugay, S. Tricard, G. Molnár, L. Salmon, J. Carrey, W. Nicolazzi, A. Rotaru, A. Bousseksou, Chem. Phys. Lett. 644 (2016) 138–141.
[87] F. Prins, M. Monrabal-Capilla, E.A. Osorio, E. Coronado, H.S.J. van der Zant, Adv. Mater. 23 (2011) 1545–1549.
[88] G. Gallé, C. Etrillard, J. Degert, F. Guillaume, J.-F. Létard, E. Freysz, Appl. Phys. Lett. 102 (2013) 063302.
[89] T. Zhao, L. Cuignet, M.M. Dîrtu, M. Wolff, V. Spasojevic, I. Boldog, A. Rotaru, Y. Garcia, C. Janiak, J. Mater. Chem. C 3 (2015) 7802–7812.
[90] S. Titos-Padilla, J.M. Herrera, X.-W. Chen, J.J. Delgado, E. Colacio, Angew. Chem., Int. Ed. 50 (2011) 3290–3293.
[91] I.A. Gural'skiy, G. Molnár, I.O. Fritsky, L. Salmon, A. Bousseksou, Polyhedron 38 (2012) 245–250.
[92] T.Q. Hung, F. Terki, S. Kamara, M. Dehbaoui, S. Charar, B. Sinha, C. Kim, P. Gandit, I.A. Gural'skiy, G. Molnar, L. Salmon, H.J. Shepherd, A. Bousseksou, Angew. Chem., Int. Ed. 52 (2013) 1185–1188.
[93] A. Akou, I.A. Gural'skiy, L. Salmon, C. Bartual-Murgui, C. Thibault, C. Vieu, G. Molnár, A. Bousseksou, J. Mater. Chem. C 22 (2012) 3752.
[94] C.M. Quintero, I.A. Gural'skiy, L. Salmon, G. Molnár, C. Bergaud, A. Bousseksou, J. Mater. Chem. C 22 (2012) 3745.
[95] K. Abdul-Kader, M. Lopes, C. Bartual-Murgui, O. Kraieva, E.M. Hernández, L. Salmon, W. Nicolazzi, F. Carcenac, C. Thibault, G. Molnár, A. Bousseksou, Nanoscale 5 (2013) 5288.
[96] I.A. Gural'skiy, V.A. Reshetnikov, A. Szebeszczyk, E. Gumienna-Kontecka, A.I. Marynin, S.I. Shylin, V. Ksenofontov, I.O. Fritsky, J. Mater. Chem. C 3 (2015) 4737–4741.
[97] H. Peng, G. Molnár, L. Salmon, A. Bousseksou, Eur. J. Inorg. Chem. (2015) 3336–3342.
[98] H. Peng, G. Molnár, L. Salmon, A. Bousseksou, Chem. Commun. 51 (2015) 9346–9349.
[99] I. Boldog, A.B. Gaspar, V. Martínez, P. Pardo-Ibañez, V. Ksenofontov, A. Bhattacharjee, P. Gütlich, J.A. Real, Angew. Chem., Int. Ed. 47 (2008) 6433–6437.
[100] F. Volatron, L. Catala, E. Rivière, A. Gloter, O. Stéphan, T. Mallah, Inorg. Chem. 47 (2008) 6584–6586.
[101] R.M. van der Veen, O.-H. Kwon, A. Tissot, A. Hauser, A.H. Zewail, Nat. Chem. 5 (2013) 395–402.
[102] D.M. Sagar, F.G. Baddour, P. Konold, J. Ullom, D.A. Ruddy, J.C. Johnson, R. Jimenez, J. Phys. Chem. Lett. 7 (2016) 148–153.
[103] J. Larionova, L. Salmon, Y. Guari, A. Tokarev, K. Molvinger, G. Molnár, A. Bousseksou, Angew. Chem. Int. Ed. 47 (2008) 8236–8240.
[104] W.L. Teng, E. Khor, T.K. Tan, L.Y. Lim, S.C. Tan, Carbohydr. Res. 332 (2001) 305–316.
[105] S. Cobo, G. Molnár, J.A. Real, A. Bousseksou, Angew. Chem. Int. Ed. 45 (2006) 5786–5789.
[106] H. Peng, S. Tricard, G. Félix, G. Molnár, W. Nicolazzi, L. Salmon, A. Bousseksou, Angew. Chem. Int. Ed. 53 (2014) 10894–10898.
[107] T. Kawamoto, S. Abe, Chem. Commun. (2005) 3933–3935.
[108] H. Oubouchou, A. Slimani, K. Boukheddaden, Phys. Rev. B 87 (2013).
[109] G. Félix, W. Nicolazzi, L. Salmon, G. Molnár, M. Perrier, G. Maurin, J. Larionova, J. Long, Y. Guari, A. Bousseksou, Phys. Rev. Lett. 110 (2013) 235701.
[110] D. Chiruta, J. Linares, M. Dimian, Y. Alayli, Y. Garcia, Eur. J. Inorg. Chem. 2013 (2013) 5086–5093.
[111] M. Mikolasek, G. Félix, W. Nicolazzi, G. Molnár, L. Salmon, A. Bousseksou, New J. Chem. 38 (2014) 1834.
[112] R. Tanasa, J. Laisney, A. Stancu, M.-L. Boillot, C. Enachescu, Appl. Phys. Lett. 104 (2014) 031909.
[113] D. Chiruta, C.-M. Jureschi, J. Linares, J. Nasser, A. Rotaru, Phys. B: Condens. Matter. 476 (2015) 61–70.
[114] I. Gudyma, A. Maksymov, L. Spinu, Appl. Surf. Sci. 352 (2015) 60–65.
[115] C. Enachescu, R. Tanasa, A. Stancu, A. Tissot, J. Laisney, M.-L. Boillot, Appl. Phys. Lett. 109 (2016) 031908.
[116] J. Linares, C. Jureschi, K. Boukheddaden, Magnetochemistry 2 (2016) 24.
[117] J. Linares, C.-M. Jureschi, A. Boulmaali, K. Boukheddaden, Phys. B: Condens. Matter. 486 (2016) 164–168.
[118] C. Jureschi, J. Linares, A. Rotaru, Y. Garcia, Magnetochemistry 2 (2016) 13.
[119] M. Mikolasek, W. Nicolazzi, F. Terki, G. Molnár, A. Bousseksou, Phys. Chem. Chem. Phys. 19 (2017) 12276–12281.
[120] I. Gudyma, V. Ivashko, A. Bobák, Nanoscale Res. Lett. 12 (2017).
[121] G. Félix, M. Mikolasek, H. Peng, W. Nicolazzi, G. Molnár, A.I. Chumakov, L. Salmon, A. Bousseksou, Phys. Rev. B 91 (2015).
[122] M. Mikolasek, G. Felix, H. Peng, S. Rat, F. Terki, A.I. Chumakov, L. Salmon, G. Molnar, W. Nicolazzi, A. Bousseksou, Phys. Rev. B 96 (2017).
[123] A. Tissot, L. Rechignat, A. Bousseksou, M.-L. Boillot, J. Mater. Chem. 22 (2012) 3411.
[124] R. Bertoni, M. Lorenc, A. Tissot, M. Servol, M.-L. Boillot, E. Collet, Angew. Chem., Int. Ed. 51 (2012) 7485–7489.
[125] P. Chakraborty, M.-L. Boillot, A. Tissot, A. Hauser, Angew. Chem., Int. Ed. 52 (2013) 7139–7142.
[126] L. Zhang, J.-J. Wang, G.-C. Xu, J. Li, D.-Z. Jia, S. Gao, Dalton Trans. 42 (2013) 8205–8208.
[127] J. Laisney, A. Tissot, G. Molnár, L. Rechignat, E. Rivière, F. Brisset, A. Bousseksou, M.-L. Boillot, Dalton Trans. 44 (2015) 17302–17311.
[128] L.L. Nguyen, R. Guillot, J. Laisney, L. Rechignat, S. Bedoui, G. Molnár, E. Rivière, M.-L. Boillot, New J. Chem. 39 (2015) 1603–1610.
[129] S.M. Neville, C. Etrillard, S. Asthana, J.-F. Létard, Eur. J. Inorg. Chem. (2010) 282–288.
[130] C. Göbel, O. Klimm, F. Puchtler, S. Rosenfeldt, S. Förster, B. Weber, Beilstein J. Nanotechnol. 8 (2017) 1318–1327.
[131] G. Molnár, S. Rat, L. Salmon, W. Nicolazzi, A. Bousseksou, Adv. Mater. 30 (2018) 1703862, https://doi.org/10.1002/adma.201703862.
[132] A. Slimani, H. Khemakhem, K. Boukheddaden, Phys. Rev. B 95 (2017) 174104.
[133] L. Stoleriu, P. Chakraborty, A. Hauser, A. Stancu, C. Enachescu, Phys. Rev. B 84 (2011) 132105.
[134] A. Tissot, C. Enachescu, M.-L. Boillot, J. Mater. Chem. 22 (2012) 20451.
[135] A. Tokarev, J. Long, Y. Guari, J. Larionova, F. Quignard, P. Agulhon, M. Robitzer, G. Molnár, L. Salmon, A. Bousseksou, New J. Chem. 37 (2013) 3420.
[136] D.J. McHugh, A Guide to the Seaweed Industry, Food and Agriculture Organization of the United Nations, Rome, 2003.
[137] J.M. Herrera, S. Titos-Padilla, S.J.A. Pope, I. Berlanga, F. Zamora, J.J. Delgado, K.V. Kamenev, X. Wang, A. Prescimone, E.K. Brechin, E. Colacio, J. Mater. Chem. C 3 (2015) 7819–7829.
[138] Y.-S. Koo, J.R. Galán-Mascarós, Adv. Mater. 26 (2014) 6785–6789.
[139] M.D. Manrique-Juárez, Micro and Nanoactuators Based on Bistable Molecular Materials, 2018. Toulouse.
[140] I.A. Gural'skiy, C.M. Quintero, K. Abdul-Kader, M. Lopes, C. Bartual-Murgui, L. Salmon, P. Zhao, G. Molnár, D. Astruc, A. Bousseksou, J. Nanophoton. 6 (2012), 063517–1.
[141] C.M. Quintero, G. Félix, I. Suleimanov, J. Sánchez Costa, G. Molnár, L. Salmon, W. Nicolazzi, A. Bousseksou, Beilstein J. Nanotechnol. 5 (2014) 2230–2239.
[142] K. Senthil Kumar, M. Ruben, Coord. Chem. Rev. 346 (2017) 176–205.

[143] V. Escax, A. Bleuzen, C. Cartier dit Moulin, F. Villain, A. Goujon, F. Varret, M. Verdaguer, J. Am. Chem. Soc. 123 (2001) 12536–12543.
[144] S. Ohkoshi, H. Tokoro, K. Hashimoto, Coord. Chem. Rev. 249 (2005) 1830–1840.
[145] W. Kosaka, K. Nomura, K. Hashimoto, S.I. Ohkoshi, J. Am. Chem. Soc. 127 (2005) 8590–8591.
[146] T. Mallah, S. Thiebaut, M. Verdaguer, P. Veillet, Science 262 (1993) 1554–1557.
[147] M. Verdaguer, A. Bleuzen, V. Marvaud, J. Vaissermann, M. Seuleiman, C. Desplanches, A. Scuiller, C. Train, R. Garde, G. Gelly, C. Lomenech, I. Rosenman, P. Veillet, C. Cartier, F. Villain, Coord. Chem. Rev. 190 (1999) 1023–1047.
[148] M. Presle, J. Lemainque, J.-M. Guigner, E. Larquet, I. Maurin, J.-P. Boilot, T. Gacoin, New J. Chem. 35 (2011) 1296.
[149] O.N. Risset, D.R. Talham, Chem. Mater. 27 (2015) 3838–3843.
[150] M.F. Dumont, E.S. Knowles, A. Guiet, D.M. Pajerowski, A. Gomez, S.W. Kycia, M.W. Meisel, D.R. Talham, Inorg. Chem. 50 (2011) 4295–4300.
[151] N. Dia, L. Lisnard, Y. Prado, A. Gloter, O. Stéphan, F. Brisset, H. Hafez, Z. Saad, C. Mathonière, L. Catala, T. Mallah, Inorg. Chem. 52 (2013) 10264–10274.
[152] M. Presle, I. Maurin, F. Maroun, R. Cortès, L. Lu, R. Sayed Hassan, E. Larquet, J.-M. Guigner, E. Rivière, J.P. Wright, J.-P. Boilot, T. Gacoin, J. Phys. Chem. C 118 (2014) 13186–13195.
[153] O.N. Risset, T.V. Brinzari, M.W. Meisel, D.R. Talham, Chem. Mater. 27 (2015) 6185–6188.
[154] C.R. Gros, M.K. Peprah, A.C. Felts, T.V. Brinzari, O.N. Risset, J.M. Cain, C.F. Ferreira, M.W. Meisel, D.R. Talham, Dalton Trans. 45 (2016) 16624–16634.
[155] O.N. Risset, P.A. Quintero, T.V. Brinzari, M.J. Andrus, M.W. Lufaso, M.W. Meisel, D.R. Talham, J. Am. Chem. Soc. 136 (2014) 15660–15669.
[156] C.R. Gros, M.K. Peprah, B.D. Hosterman, T.V. Brinzari, P.A. Quintero, M. Sendova, M.W. Meisel, D.R. Talham, J. Am. Chem. Soc. 136 (2014) 9846–9849.
[157] Y.X. Wang, D. Qiu, S.F. Xi, Z.D. Ding, Z.J. Li, Y.X. Li, X.H. Ren, Z.G. Gu, Chem. Commun. 52 (2016) 8034–8037.
[158] H.J. Shepherd, C. Quintero, G. Molnar, L. Salmon, A. Bousseksou, Spin-crossover Materials: Properties and Applications, Wiley, 2013.
[159] C. Quintero, G. Molnár, L. Salmon, A. Tokarev, C. Bergaud, A. Bousseksou, Halcrowcholl of chemistry, in: A. Malcolm (Ed.), 16th International Workshop on Thermal Investigations of ICs and Systems (THERMINIC), University of Leeds, UK, 2010, pp. 1–5.
[160] M. Matsuda, H. Isozaki, H. Tajima, Thin Solid Films 517 (2008) 1465–1467.
[161] I. Suleimanov, O. Kraieva, G. Molnár, L. Salmon, A. Bousseksou, Chem. Commun. 51 (2015) 15098–15101.
[162] I. Suleimanov, O. Kraieva, J. Sánchez Costa, I.O. Fritsky, G. Molnár, L. Salmon, A. Bousseksou, J. Mater. Chem. C 3 (2015) 5026–5032.
[163] O. Kraieva, I. Suleimanov, G. Molnár, L. Salmon, A. Bousseksou, Magnetochemistry 2 (2016) 11.
[164] I. Suleimanov, G. Molnar, L. Salmon, A. Bousseksou, Eur. J. Inorg. Chem. (2017) 3446.
[165] G. Félix, K. Abdul-Kader, T. Mahfoud, I.A. Gural'skiy, W. Nicolazzi, L. Salmon, G. Molnár, A. Bousseksou, J. Am. Chem. Soc. 133 (2011) 15342–15345.
[166] C. Bartual-Murgui, A. Cerf, C. Thibault, C. Vieu, L. Salmon, G. Molnár, A. Bousseksou, Microelectron. Eng. 111 (2013) 365–368.
[167] I. Suleimanov, J. Sánchez Costa, G. Molnár, L. Salmon, A. Bousseksou, Chem. Commun. 50 (2014) 13015–13018.
[168] D. Qiu, L. Gu, X.-L. Sun, D.-H. Ren, Z.-G. Gu, Z. Li, RSC Adv. 4 (2014) 61313–61319.
[169] W. Hellel, A. Ould Hamouda, J. Degert, J.F. Létard, E. Freysz, Appl. Phys. Lett. 103 (2013) 143304.
[170] L. Moulet, N. Daro, S. Mornet, N. Vilar-Vidal, G. Chastanet, P. Guionneau, Chem. Commun. 52 (2016) 13213–13216.
[171] Z.-H. Li, Y.-X. Wang, W.-K. Han, W. Zhu, T. Li, Z. Li, X. Ren, Z.-G. Gu, New J. Chem. 41 (2017) 10062–10068.
[172] S. Rat, M. Piedrahita-Bello, L. Salmon, G. Molnár, P. Demont, A. Bousseksou, Adv. Mater. 30 (2018) 1705275.
[173] M.S. Alam, M. Stocker, K. Gieb, P. Müller, M. Haryono, K. Student, A. Grohmann, Angew. Chem. Int. Ed. 49 (2010) 1159–1163.
[174] I. Beljakov, V. Meded, F. Symalla, K. Fink, S. Shallcross, M. Ruben, W. Wenzel, Nano Lett. 14 (2014) 3364–3368.
[175] Y. Murashima, M.R. Karim, N. Saigo, H. Takehira, R. Ohtani, M. Nakamura, M. Koinuma, L.F. Lindoy, K. Kuroiwa, S. Hayami, Inorg. Chem. Front. 2 (2015) 886–892.
[176] M. Bernien, H. Naggert, L.M. Arruda, L. Kipgen, F. Nickel, J. Miguel, C.F. Hermanns, A. Krüger, D. Krüger, E. Schierle, E. Weschke, F. Tuczek, W. Kuch, ACS Nano 9 (2015) 8960–8966.
[177] D. Qiu, D.-H. Ren, L. Gu, X.-L. Sun, T.-T. Qu, Z.-G. Gu, Z. Li, RSC Adv. 4 (2014) 31323–31327.
[178] A. Holovchenko, J. Dugay, M. Giménez-Marqués, R. Torres-Cavanillas, E. Coronado, H.S.J. van der Zant, Adv. Mater. 28 (2016) 7228–7233.
[179] J. Dugay, M. Aarts, M. Giménez-Marqués, T. Kozlova, H.W. Zandbergen, E. Coronado, H.S.J. van der Zant, Nano Lett. 17 (2017) 186–193.
[180] I.A. Gural'skiy, C.M. Quintero, J.S. Costa, P. Demont, G. Molnár, L. Salmon, H.J. Shepherd, A. Bousseksou, J. Mater. Chem. C 2 (2014) 2949–2955.
[181] Y.-C. Chen, Y. Meng, Z.-P. Ni, M.-L. Tong, J. Mater. Chem. C 3 (2015) 945–949.
[182] M.D. Manrique-Juárez, S. Rat, L. Salmon, G. Molnár, C.M. Quintero, L. Nicu, H.J. Shepherd, A. Bousseksou, Coord. Chem. Rev. 308 (2016) 395–408.
[183] M.D. Manrique-Juárez, F. Mathieu, A. Laborde, S. Rat, V. Shalabaeva, P. Demont, O. Thomas, L. Salmon, T. Leichle, L. Nicu, G. Molnár, A. Bousseksou, Adv. Funct. Mater. 28 (2018) 1801970.
[184] V. Nagy, K. Halász, M.-T. Carayon, I.A. Gural'skiy, S. Tricard, G. Molnár, A. Bousseksou, L. Salmon, L. Csóka, Phys. Eng. Asp. 456 (2014) 35–40.
[185] S. Rat, V. Nagy, I. Suleimanov, G. Molnár, L. Salmon, P. Demont, L. Csóka, A. Bousseksou, Chem. Commun. 52 (2016) 11267–11269.